

Advancing microfluidic single-cell analysis technologies, techniques, and applications for the
study of cancers and neuroinflammatory diseases

by

Jay Sibbitts

B.S., Truman State University, 2014

AN ABSTRACT OF A DISSERTATION

submitted in partial fulfillment of the requirements for the degree

DOCTOR OF PHILOSOPHY

Department of Chemistry
College of Arts and Sciences

KANSAS STATE UNIVERSITY
Manhattan, Kansas

2021

Abstract

As the fight against cancers, neuroinflammatory diseases, and other chronic illnesses progresses, bioanalytical technologies and techniques must also advance to provide researchers with a greater depth of information so they may better understand what factors are at play at the cellular level. In recent years, researchers have begun to turn toward the rapidly growing field of microfluidics. Microfluidic technologies have proven to be invaluable in a wide variety of bioanalytical applications in areas such as point-of-care diagnostics, in vitro cellular analysis, and especially single-cell analysis.

The chapters of this dissertation will present and discuss results and progress on 3 microfluidic-based projects. Chapter 2 reports improvements made on the single-cell analysis (SCA) system developed by the Culbertson group that were enabled by low-cost electronics and 3D printing technology. Additionally, results of the measurement of intracellular nitric oxide (NO), an inflammatory biomarker, in single cells using a model cell line (Jurkat, T-lymphocytes) under inflammatory, native, and inhibitory conditions are reported. Chapter 3 incorporates the improvements described in Chapter 2 and demonstrates the capabilities of the SCA system for applications in studying the effects of anti-inflammatory therapeutics for the treatment of neurodegenerative pathologies. An analytical strategy, similar to that developed in Chapter 2, is used to measure intracellular NO levels in the recently discovered immortalized SIM-A9 microglia cell line. Additionally, Chapter 3 presents an interesting in-depth statistical analysis on the distributions of NO levels in microglia under inflammatory, native, and inhibitory conditions, which highlights the potential depth of information made available by performing analyses with single-cell resolution. Finally, Chapter 4 will focus on efforts toward developing a solid-state actuation modality using a dielectric elastomer. The ultimate goal for the dielectric elastomer

actuator technology will be to perform 2 functions in microfluidic systems: the application of precise mechanical stress on cells to study potentially interesting mechanotransduction phenomena and to serve as the basis for a novel non-pneumatic valve.

Advancing microfluidic single-cell analysis technologies, techniques, and applications for the
study of cancers and neuroinflammatory diseases

by

Jay Sibbitts

B.S., Truman State University, 2014

A DISSERTATION

submitted in partial fulfillment of the requirements for the degree

DOCTOR OF PHILOSOPHY

Department of Chemistry
College of Arts and Sciences

KANSAS STATE UNIVERSITY
Manhattan, Kansas

2021

Approved by:

Major Professor
Christopher T. Culbertson

Copyright

© Jay Sibbitts 2021.

Abstract

As the fight against cancers, neuroinflammatory diseases, and other chronic illnesses progresses, bioanalytical technologies and techniques must also advance to provide researchers with a greater depth of information so they may better understand what factors are at play at the cellular level. In recent years, researchers have begun to turn toward the rapidly growing field of microfluidics. Microfluidic technologies have proven to be invaluable in a wide variety of bioanalytical applications in areas such as point-of-care diagnostics, in vitro cellular analysis, and especially single-cell analysis.

The chapters of this dissertation will present and discuss results and progress on 3 microfluidic-based projects. Chapter 2 reports improvements made on the single-cell analysis (SCA) system developed by the Culbertson group that were enabled by low-cost electronics and 3D printing technology. Additionally, results of the measurement of intracellular nitric oxide (NO), an inflammatory biomarker, in single cells using a model cell line (Jurkat, T-lymphocytes) under inflammatory, native, and inhibitory conditions are reported. Chapter 3 incorporates the improvements described in Chapter 2 and demonstrates the capabilities of the SCA system for applications in studying the effects of anti-inflammatory therapeutics for the treatment of neurodegenerative pathologies. An analytical strategy, similar to that developed in Chapter 2, is used to measure intracellular NO levels in the recently discovered immortalized SIM-A9 microglia cell line. Additionally, Chapter 3 presents an interesting in-depth statistical analysis on the distributions of NO levels in microglia under inflammatory, native, and inhibitory conditions, which highlights the potential depth of information made available by performing analyses with single-cell resolution. Finally, Chapter 4 will focus on efforts toward developing a solid-state actuation modality using a dielectric elastomer. The ultimate goal for the dielectric elastomer

actuator technology will be to perform 2 functions in microfluidic systems: the application of precise mechanical stress on cells to study potentially interesting mechanotransduction phenomena and to serve as the basis for a novel non-pneumatic valve.

Table of Contents

List of Figures.....	xi
List of Tables	xv
Acknowledgements	xvi
Dedication.....	xvii
Chapter 1 - Introduction	1
1.1 Analytical separations	1
1.2 Fluid transport in capillaries and microfluidic devices	3
1.2.1 Pressure induced flow	3
1.2.2 Electroosmotic flow	5
1.3 Electrophoretic separations.....	7
1.4 Describing analytical separations.....	10
1.5 Microfluidics.....	19
1.5.1 Microscale fabrication	20
1.5.2 Fluid Manipulation	24
1.5.3 Microfluidics and single-cell analysis	26
1.6 Measuring nitric oxide.....	28
1.7 DIY technologies in the research laboratory	31
1.7.1 3D printing	31
1.7.2 Low-cost open-source electronics	32
1.7 Conclusion.....	34
Chapter 2 - Improvements on fabrication and operation of a single-cell analysis device for the measurement of nitric oxide production in T lymphocytes.....	36

2.1 Introduction.....	36
2.2 Materials and methods.....	38
2.2.1 Reagents and materials.....	38
2.2.2 Tissue culture.....	39
2.2.3 Sample preparation	40
2.2.4 Device design and working principles.....	41
2.2.5 Device fabrication.....	45
2.2.6 Device setup and operation	48
2.2.7 Single-cell analysis experiments	52
2.2.8 Characterization of optical fiber signal improvement	54
2.3 Discussion and results	56
2.3.1 Measurement of changes in NO production.....	56
2.3.2 Optical fiber signal improvement	58
2.4 Concluding remarks	59
Chapter 3 - Single-cell analysis of nitric oxide in SIM-A9 microglial cells.....	61
3.1 Introduction.....	61
3.2 Materials and methods.....	63
3.2.1 Reagents and materials.....	63
3.2.2 Device fabrication and setup	65
3.2.3 Tissue culture.....	65
3.2.4 Sample preparation	65
3.3 Results and discussion	67
3.3.1 Measurement of NO production	67

3.3.2 Single vs bulk cell analysis	75
3.4 Conclusion	76
Chapter 4 - Efforts toward developing applications of integrated dielectric elastomer actuator (IDEA) technology in microfluidics and cellular analysis	78
4.1 Introduction.....	78
4.1.1 Dielectric elastomeric actuators.....	79
4.1.2 DEA applications and potential.....	82
4.2 Materials and methods.....	83
4.2.1 Reagents and materials.....	83
4.2.2 Microchip design and fabrication for valve device	84
4.2.3 Tissue culture.....	86
4.2.4 Testing of valve device	87
4.2.5 Mechanical stretching device fabrication, setup, and testing.....	88
4.3 Results and discussion	91
4.3.1 Video analysis of valve actuation.....	91
4.3.2 Development of mechanical stretching device.....	92
4.4 Concluding remarks	95
Chapter 5 - Future direction.....	97
References	99
Appendix A - Protocols.....	105
Appendix B - Photographs of etched ITO grid electrodes	111
Appendix C - Arduino code for pumping control.....	112

List of Figures

- Figure 1.1 A profile of the velocities generated by pressure induced flow. The size of the red arrows indicates the magnitude of the velocity vector.5
- Figure 1.2 (Top) A diagram showing the planar flow profile generated by electroosmotic flow. (Bottom) A diagram showing the electric double layer, IHP, OHP and the change in electrostatic potential (ψ) as a function of the distance from the capillary wall (r).6
- Figure 1.3 An example electropherogram showing two well resolved components with migration times of t_{m1} and t_{m2} . The graphical method for determining peak width by drawing tangent lines at the interior inflection points of peak 1. Assuming a gaussian peak shape, the width can be expressed as 4σ , where σ is the standard deviation of the peak. 11
- Figure 1.4 A generalized workflow for the process steps of photolithographic micropatterning. 22
- Figure 1.5 A generalized workflow for the process steps for the fabrication of a 1-layer PDMS-based microfluidic device using soft lithography.23
- Figure 1.6 A scheme illustrating the process of multilayer microfluidic device fabrication. The device design shown and the details of each step pertain specifically to the fabrication of the single cell analysis device reported by the Culbertson research group.¹24
- Figure 1.7 (A) A 3D drawing illustrating the actuation of a Quake-style valve both opened (top) and closed (bottom). Green arrows on the closed valve indicate the direction of fluid displacement. (B) Diagrams illustrating single (left) and multiplexed (right) integrated peristaltic pumps. The numbered circles represent the input ports for compressed air. The diagram of the multiplexed peristaltic pumps is based on designs reported by the Culbertson group.^{1, 3-4}26

Figure 1.8 Reaction scheme for the loading of 6-CFDA (top) and DAF-FM DA (bottom) into cells; Both fluorescent probes are modified by intracellular esterases, DAF-FM reacts further with NO to form the strongly fluorescent DAF-FM T derivative.30

Figure 1.9 A photograph of an Arduino UNO R3 microcontroller board.....33

Figure 2.1 Diagram of the single cell μ CE-LIF device; Pneumatic inlets for the peristaltic pumps are numbered 1-4. HV electrodes connected to the positive voltage source and ground are placed into the +V and GND reservoirs, respectively. The Waste, GND, +V, auxiliary buffer (AB) reservoirs are filled with electrophoresis buffer. Cells are loaded into the sample (S) reservoir. Locations for both ends of the optical fiber are shown as the cell detection point (CDP) and the lysate detection point (LDP).42

Figure 2.2 3D render of the SCA device with integrated fiber bridge. (Lower left) A diagram of the cell transport and lysis processes; The red dotted arrows represent the electrophoretic flow and the solid blue arrows represent the hydrodynamic flow direction. (Lower right) A diagram showing the optical path that the excitation (blue) and emission (green) light travels, and the application of the RI gel to the fiber-membrane interface.43

Figure 2.3 A series of single-cell electropherograms. The intact signal and separated lysate contents are labeled for the first cell, and subsequent cells are indicated by the dotted rectangles.44

Figure 2.4 (A) Photograph of the fully assembled microfluidic SCA device with custom 3D printed stage plate and optical fiber manipulators. (B) Photograph showing the fiber-membrane interface with RI gel (20x).....50

Figure 2.5 A diagram of the fluorescence detection optics setup. Excitation light from a solid-state diode laser is directed toward the objective through a fluorescence filter cube with a

dichroic mirror. Fluorescence emission is collected through the objective and is directed toward the photomultiplier tube.	51
Figure 2.6 Representative electropherograms from the native, inhibited and stimulated experiments.	53
Figure 2.7 Fluorescence signal from 10 μm fluorescent polystyrene microspheres with RI gel (blue) and without (green).	55
Figure 3.1 A scheme illustrating the procedure used to prepare cells for NO measurements. Created using Biorender.com.....	66
Figure 3.2 A representative excerpt of fluorescence data for single cell analysis of NO in SIM-A9 microglia. Each cell produced a total of 4 peaks: intact cell, 6-CF, DAF-DHA and DAF-FM T.....	68
Figure 3.3 Histogram plots of the peak area ratios for native (A), stimulated (B), and inhibited (C) conditions. The insets in A-C are histogram plots for the log transformed datasets. The traces are lognormal fits for the main plots and gaussian for the inset plots.	70
Figure 3.4 An overlay of single-cell electropherograms for native, stimulated, and inhibited cells. Fluorescence intensities have been scaled according to the internal standard peak signal. ..	74
Figure 4.1 A diagram illustrating a generic DEA and its actuation. (A) A DE layer is sandwiched between two compliant electrodes with no electric field applied. (B) An electric field is applied causing compression in the z direction (green arrows) and expansion in the xy-plane (red arrows).	79
Figure 4.2 A photograph of dielectric breakdown of a 40 μm PDMS film. As dielectric breakdown occurs, high energy electrons burn a hole through the film and a visible electrical arc can be observed.	81

Figure 4.3 A diagram showing the general layout of the valve layer(light blue) and the fluidic layer (gray) atop the etched ITO electrode. The enlarged region (right) shows is a cartoon representation of the IDEA actuation unit. The red arrows indicate the direction of the compressive force generated upon actuation.87

Figure 4.4 A cartoon of the proposed cell stretching device (left) and working principles of cell stretching (right); The electric field is applied across the PDMS membrane between the electrically conductive growth medium (GND) and the patterned ITO electrode (+V).90

Figure 4.5 IDEA valve actuation data from video frame analysis using ImageJ software; (left) video stills of the off and on states of the IDEA, the yellow lines indicate where intensity data were measured; (right) change in fluorescent intensity between the on and off actuation states.92

Figure 4.6 Contact angle measurements of native (left) and modified (right) PDMS substrates; Native PDMS contact angle was measured at 110°, modified PDMS contact angle was measured at 66.4°.93

Figure 4.7 Photographs taken 24 after cells seeded on native (left) and PDL treated (right) PDMS substrates.....95

List of Tables

Table 2.1 The average ratios (DAF-FM T/6-CF \pm standard deviation) of the peak area and peak height for native, stimulated and inhibited cells.	54
Table 2.2 Average intensity and 95% confidence interval of fluorescence signals from 10 μ m fluorescent microspheres with and without the application of RI gel to the optical fiber faces.	55
Table 2.3 Percent difference and associated p-values for the peak area ratios for each experimental condition.	57
Table 3.1 Skewness and Shapiro-Wilk p-values for untransformed and log transformed datasets for native, stimulated, and inhibited conditions.	70
Table 3.2 Calculated percent differences in the peak area ratios between each experimental condition. The p-values listed correspond to the one-tailed t0test for the comparison of means of independent samples performed on the log transformed datasets.	72
Table 3.3 Arithmetic and geometric summary statistics for native, stimulated, and inhibited datasets; ^a The $\times/$ for geometric statistics is analogous to the \pm for arithmetic statistics. The lower and upper bounds of the 95% confidence interval are: $\bar{x}^* \div s^{*2}$ and $\bar{x}^* \times s^{*2}$. ²	72

Acknowledgements

To Lisa Balbes, you've been there for me since the beginning and I will always be grateful for that.

To my cousin Joe, thank you for giving me the valuable advice of choosing an advisor that I can work with over one whose work I am interested in. I know I made the right choice

To my uncle Joe, thank you for all the stories, laughs, and spiritual guidance.

To Jim Hodgson, thank you for the years of conversations, encouragement and advice. I hope that we remain friends over the years.

To Tobe Eggers, thank you for always answering my questions and helping me troubleshoot problematic computers; It's all good.

To Ron Jackson, thank you for your insight and creativity. You helped me come up with a lot of solutions to some weird problems.

To Chris, thank you for the years of fun and learning. I always felt like I was doing graduate school wrong because people would ask me what it was like and I said it was like a government funded playground. Thank you for continually pushing me to just give it a shot and make it pretty later.

To Anne, thank you for teaching me how to handle cells. I came into graduate school with no biology experience whatsoever and you gave me the tools I needed to become the dedicated "cell person" of our lab.

To Damith, thank you for teaching me the fundamentals I needed to even begin. I really wish we had gotten drinks together more.

To Jalal, thank you for teaching me about optics and always being a bright personality in the lab. I find it strange when months go by and I haven't had to let you into your office because you forgot your keys.

To Kathleen, thank you for helping me learn the value of the adobe creative suite and for tolerating me in my social moods and kept distracting you from your work. It was so cool to watch you take the IEF project from scratch and go as far as you did.

To Michael, thank you for helping me grow as a teacher. Your dedication to your work is something I aspire to have.

To Stefan, working with you has been such a joy. Thank you for always being so kind and encouraging.

To Shu, it has been a wild ride and I know you're not far behind. See you on the other side my friend.

To Abby, I'm so glad you decided to join our crew and I look forward to continuing working with you. Your friendship has helped me so much in the final stretch of my PhD here, thank you.

To Rob, Grace and Jordan, having a supportive set of siblings has made life during my PhD much easier to bear because I know I am never alone. Thank you.

And finally, thank you to my mom and dad. I love you both very much and I cannot thank you enough for providing me the best environment possible to grow into the person that I am today.

Dedication

To my loving parents, Gary and Terry, I couldn't have done this without your endless
love and support, thank you.

Chapter 1 - Introduction

1.1 Analytical separations

Analytical separation techniques are ubiquitous in almost all laboratory settings. The ability to reliably separate, identify and isolate components within a mixture is critical in research labs conducting organic synthesis, proteomic and genomic assays, environmental studies as well as in industrial settings for quality control. In these fields, separations are either used in a preparative manner, as a means of purification for end use (e.g. pharmaceuticals, manufacturing materials, fuels), or in an analytical manner as a tool to determine the composition of a sample mixture. The concepts discussed in this chapter and beyond will focus on the latter. Within analytical separations two prominent categories will be discussed: chromatography which separates species based on distribution equilibria between two phases, and electrophoresis which separates species using an externally applied electrical potential.⁵

Chromatographic techniques come in a variety of formats such as gas chromatography (GC) and high- and ultra- performance liquid chromatography (HPLC and UPLC). In general, chromatographic separations are carried out by first dissolving the sample in the mobile phase (typically a liquid solvent) and then loading the sample at the head of a column that is either coated or packed with a stationary phase. The sample is then pushed through the column, carried via the mobile phase, and components within the mixture are separated based on differences in their distribution equilibria between the stationary and mobile phases. Analytes that interact more strongly with the stationary phase will be retained on the column longer and will, therefore, elute later than analytes with weaker stationary phase interactions. Depending on the nature of the sample and the goal of the separation there are several types of analyte-stationary phase

interactions available including adsorption, absorption, affinity, ion-exchange, immunoaffinity, size exclusion among others. While chromatographic techniques are widely used as an industry standard, there are still several drawbacks to consider. Separations using these methods are costly in terms of both time (tens of minutes per sample) and money due to high consumption rates of expensive, high-purity solvents. Additionally, if a successful separation cannot be achieved by changing the readily adjustable parameters (mobile phase composition, temperature, flow rate) then another column must be purchased which can cost hundreds or even a few thousand dollars.

In contrast, capillary electrophoresis (CE) is a powerful alternative to chromatography as it is generally less expensive and is capable of high-efficiency separations on a faster time scale (on the order of seconds per sample). CE separations begin by loading a small sample plug (0.1-10 nL), dissolved in a buffer solution, that is loaded into a small inner diameter capillary (i.d. ~20-100 μm and 25-50 cm in length) filled with the same buffer solution.⁶ An electric field is then applied across the capillary causing dissolved species to separate based on their mobility within the electric field. CE is well-suited for the separation and quantitation of biomolecules such as proteins, peptides, amino acids and DNA. More recently, electrophoresis has been adopted as the preferred mode of separation used in the field of microfluidics for the separation and analysis of biomolecules.⁷ The term microfluidic device or “lab-on-a-chip” refers to small-scale devices that consist of networks of microscale fluidic channels. While traditional CE can be used to separate nanoliter-scale sample volumes, microchip electrophoresis (μCE) can be used to analyze the contents within a single mammalian cell (picoliter-scale). The following sections will describe the principles of relevant transport phenomena in capillaries and microchannels. Subsequent sections will provide comprehensive background information for electrophoresis,

separation principles, microfluidics, techniques for nitric oxide measurement and finally an overview of emerging technologies that are being used in the microfluidics laboratory.

1.2 Fluid transport in capillaries and microfluidic devices

Fluid flow in capillaries and microchannels is driven in one of two ways, either pressure induced flow or electroosmotic flow. In both cases it is important to consider whether the flow can be described as turbulent or laminar. To quantitatively characterize the flow, a parameter called the Reynolds number (R_e) can be used and is calculated using Equation 1.1:

$$R_e = \frac{\rho u d}{\eta} \quad (1.1)$$

where ρ is the fluid density, u is the linear velocity of the fluid, d is the characteristic dimension of the channel (channel diameter for a circular cross-section), and η is the viscosity of the fluid. The Reynolds number is a dimensionless quantity that gives the ratio of inertial forces to viscous forces. At high Reynolds numbers ($R_e > 2000$) inertial forces dominate and flow is considered turbulent resulting in chaotic flow patterns. In microfluidic channels, R_e typically is $\ll 1$, meaning that viscous forces dominate and flow is considered laminar, resulting in parallel flow patterns with only diffusional lateral mixing. While laminar flow is observed for both pressure induced flow and electroosmotic flow within microchannels, each has a distinct flow profile shape caused by the underlying transport phenomena.

1.2.1 Pressure induced flow

For pressure induced flow to occur within a circular tube or capillary, a pressure differential must be applied across the two ends (Δp). The shape of the flow profile is determined by the magnitudes of the linear velocities (u_r) across the capillary cross section. To determine the

magnitude of u_r , there are two forces acting upon the fluid that must be considered: the force from the applied pressure (F_p) and the frictional drag force at the capillary wall (F_d). Assuming F_p is exerted in the positive direction, the magnitudes of these forces are given by Equations 1.2 and 1.3 respectively:

$$F_p = \Delta p \pi r_0^2 \quad (1.2)$$

$$F_d = -2\pi r_0 L \eta \left(\frac{du_r}{dr} \right)_0 \quad (1.3)$$

where r_0 is the capillary radius, L is the length of the capillary, η is the fluid viscosity, and $\left(\frac{du_r}{dr} \right)_0$ is the shear rate at the capillary wall. When the fluid has reached a constant velocity,

Equations 1.2 and 1.3 are equal and may be combined to solve for shear rate:

$$\left(\frac{du_r}{dr} \right)_0 = -\frac{\Delta p r_0}{2L\eta} \quad (1.4)$$

By treating the fluid layers within the capillary as a series of concentric cylinders with radius r , integrating Equation 1.4 gives the relationship between u_r and distance r from the capillary center:

$$u_r = -\frac{\Delta p r^2}{4L\eta} + \text{const.} \quad (1.5)$$

The constant can be solved for by considering the boundary condition at $r = r_0$, where $u_r=0$:

$$\therefore \text{const.} = \frac{\Delta p r_0^2}{4L\eta} \quad (1.6)$$

Finally, by substituting the solved constant value into Equation 1.5 and simplifying the expression, the linear velocity (u_r) of a fluid travelling through a circular capillary at a distance r from the center, as a result of a constant applied Δp can be described using Equation 1.7:

$$u_r = \frac{\Delta p}{4\eta L} (r_0^2 - r^2) \quad (1.7)$$

This relationship shows that the velocity is dependent upon the distance from the capillary wall with the maximum flow velocity at the center of the capillary ($r = 0$), and the profile of the magnitude of linear velocities is parabolic (**Figure 1.1**).

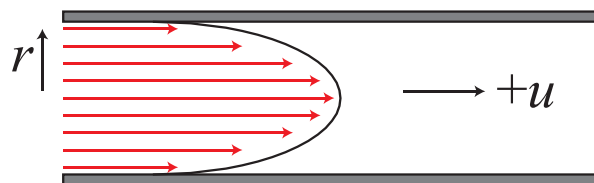


Figure 1.1 A profile of the velocities generated by pressure induced flow. The size of the red arrows indicates the magnitude of the velocity vector.

Parabolic flow is observed in all chromatographic separation methods that use pressure driven fluid handling (e.g. HPLC, UPLC and GC). This type of flow results in decreased separation resolution due to band broadening compared to electrophoretic separations.⁸

1.2.2 Electroosmotic flow

Fluid transport in capillaries and microchannels can also be achieved through a phenomenon called electroosmotic flow (EOF). EOF originates at the surface of a fused silica capillary or a glass microchannel. These surfaces are comprised of ionizable silanol groups (Si-OH) that acquire a net negative charge when in contact with an aqueous solution at $\text{pH} > 4$.⁸

Cations within the aqueous solution are attracted to the negative surface charge and form an electric double layer (EDL). The EDL is comprised of a series of layers parallel to the channel surface shown in **Figure 1.2**. The innermost layer, called the compact layer, is made of immobile cations adsorbed to the surface, i.e. not solvated, and the plane that bisects the center of charge is called the inner Helmholtz plane (IHP).⁵ The next layer out consists of solvated immobile cations, and the plane that cuts through its center of charge is called the outer Helmholtz plane (OHP). Between bulk fluid and the Helmholtz planes is a region of solvated mobile cations, called the diffuse layer, that effectively neutralizes the remaining excess surface charge. The surface charge potential (ψ) as a function of distance (r) from the capillary wall is plotted in the lower portion of **Figure 1.2**. The electrostatic potential across the diffuse layer is referred to as the zeta potential (ζ).

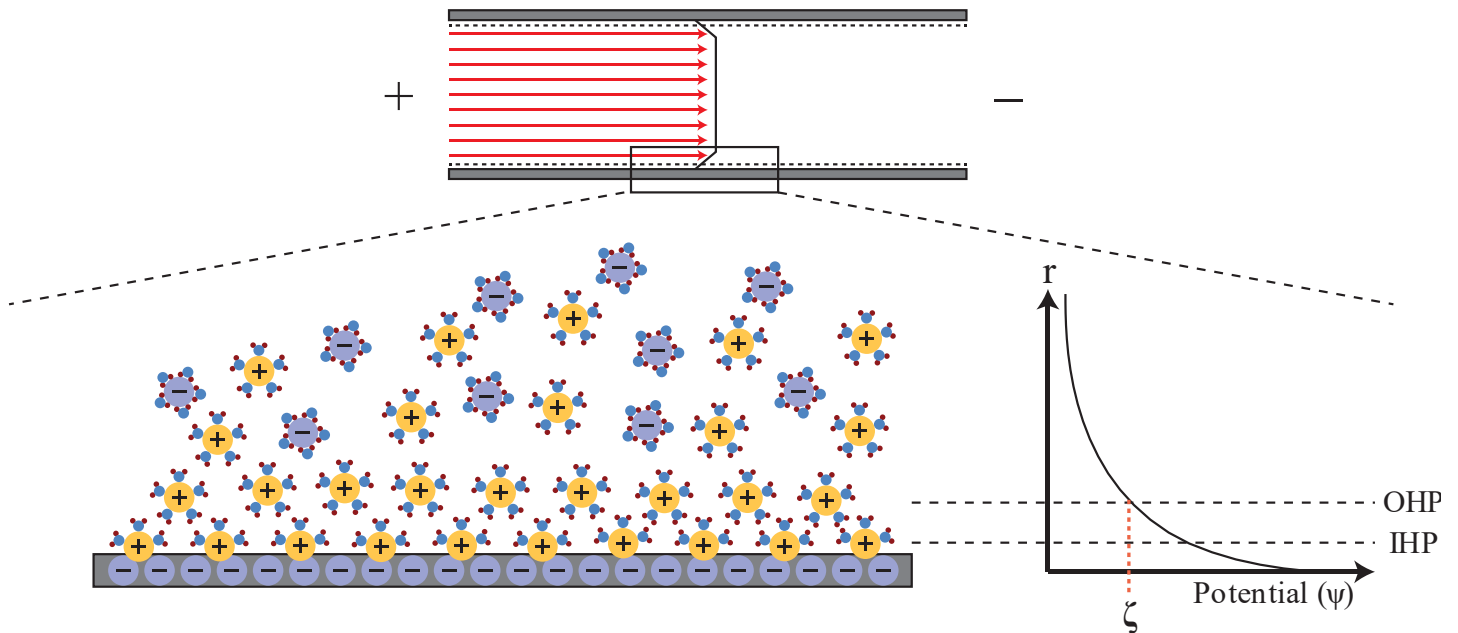


Figure 1.2 (Top) A diagram showing the planar flow profile generated by electroosmotic flow. (Bottom) A diagram showing the electric double layer, IHP, OHP and the change in electrostatic potential (ψ) as a function of the distance from the capillary wall (r).

Upon application of a high electric field across the ends of the capillary, cations in the diffuse layer migrate *en masse* toward the cathode, and viscous forces pull the adjacent bulk fluid along with them. The velocity of the bulk fluid resulting from EOF (u_{eo}) depends on the permittivity of the solution (ϵ), the electrostatic potential across the diffuse layer (ζ) can be calculated using the Smoluchowski equation:

$$u_{eo} = -\frac{\epsilon\zeta}{\eta}E = \mu_{eo}E \quad (1.8)$$

Where ϵ is the permittivity of the solution, ζ is the zeta potential, η is the viscosity of the fluid, E is the applied electric field strength (in V/cm), and μ_{eo} is the electroosmotic mobility. For negatively charged surfaces ζ is negative. However, in electrophoretic separations the positive direction is designated to be toward the negative electrode (cathode), and the negative sign in Equation 1.8 ensures u_{eo} is positive. Much like pressure induced fluid flow, u_{eo} is zero at the channel surface, however, u_{eo} does not depend upon the distance from the capillary wall beyond the OHP and remains constant across the bulk fluid which gives rise to the planar flow profile shown in **Figure 1.2**. As a result, band broadening is significantly reduced in electrophoretic separations as compared to chromatographic separations.

1.3 Electrophoretic separations

Electrophoresis is a method that separates soluble species based on differences in their migration velocities when subjected to a large direct current electric field. The use of electrophoretic separations for biological applications began with its inception in the 1930s by Swedish chemist Arne Tiselius who used it for the separation of serum proteins.⁶ Since then, a method called gel electrophoresis has emerged as the standard method of separation and

quantitation of large biomolecules such as proteins and nucleic acids (DNA and RNA). In gel electrophoresis a porous semisolid gel is immersed in an aqueous separation buffer and the sample is applied to one end of the gel. A dc electric field is then applied across the gel for a defined period of time during which sample components migrate at a speed based on their size and charge. The efficiency of an electrophoretic separation is directly proportional to the magnitude of the applied field strength. However, at high enough field strengths the frictional drag of the ionic species carrying the current begins to generate heat (Joule heating) at a rate that exceeds the system's capacity to dissipate that heat. Joule heating can result in excessive band broadening and in some cases can cause the separation buffer to boil. This limits the applied voltages for gel electrophoresis to approximately 500 V.⁶ In both capillary and microchip electrophoresis (CE and μ CE), however, heat is dissipated much more efficiently due to the increased surface area to volume ratio of capillaries and microchannels. The upper limit on voltage in these systems can be as high as 30,000 V allowing for substantially increased separation efficiencies as well as shorter separation times. The relationship between field strength and separation efficiency as well as the adverse effects of temperature on separations will be discussed in more detail in **Section 1.4**.

The overall velocity of a charged species in an electrophoretic separation (u), assuming the presence of electroosmotic flow, is the sum of the electroosmotic (u_{eo}) and electrophoretic velocities (u_{ep}):

$$u = u_{eo} + u_{ep} \quad (1.9)$$

The magnitude of the electrophoretic velocity of a charged species is governed by the electrical force exerted on the ion (F_e) and the frictional drag force from the separation buffer or medium (F_v):⁵

$$F_e = qE \quad (1.10)$$

$$F_v = -6\pi\eta r u_{ep} \quad (1.11)$$

Where q is the charge of the ion, E is the applied electric field, η is the viscosity of the separation buffer and r is the radius of the ion. Once the ion has reached a steady velocity the magnitudes of the forces are equal giving Equation 1.12, which can be rearranged to solve for u_{ep} giving Equation 1.13.

$$qE = 6\pi\eta r u_{ep} \quad (1.12)$$

$$u_{ep} = \frac{qE}{6\pi\eta r} = \mu_{ep}E \quad (1.13)$$

Where μ_{ep} is the electrophoretic mobility of the ion. By using Equation 1.8 in the previous section and Equation 1.12, Equation 1.9 can be rewritten as:

$$u = \mu_{eo}E + \mu_{ep}E \quad (1.14)$$

Because μ_{eo} , E , and η are the same for all species in a given electrophoretic separation, the differences in velocity that allow for separation are determined by the charge (q) and the effective, or hydrated, ionic radius (r). Furthermore, when electroosmotic flow is present, μ_{eo} is usually greater than μ_{ep} which means both negatively and positively charged ions as well as neutral species (i.e. $\mu_{ep} = 0$) migrate toward the cathode. Given those factors, the order in which separated species would be detected toward the cathode would be highly mobile cations followed by slower cations, then all neutral species, then less mobile anions followed by more highly mobile anions.

1.4 Describing analytical separations

While the principles behind electrophoretic and chromatographic separations are vastly different the metrics used to describe the quality and efficiency of separations are similar. When evaluating the efficiency of a separation it is useful to first consider the ideal chromatographic peak shape. As a species travels through a separation medium a number of sources contribute to the random movement of molecules within a band that results in a Gaussian distribution of concentration.⁶ Terms used to describe a Gaussian distribution, like standard deviation (σ), are also used to characterize separated peaks. For example, the baseline width of a peak is defined as approximately 4σ , as shown in **Figure 1.3**. Integrating over the range of 4σ accounts for 95% of the peak area. When discussing factors that contribute to band broadening, like diffusion, the peak variance (σ^2) is used as the metric for the breadth of a peak. An example is given in the Einstein-Smoluchowski equation that describes the how diffusion increases σ^2 over time.

$$\sigma^2 = 2Dt \quad (1.15)$$

Where D is the diffusion coefficient and t is time.

However, considering diffusion alone does not provide a complete picture of the factors that contribute to band broadening in a separation. The following sections will first define useful terms like plate height and plate number that describe the efficiency of a separation in terms of the sources of band broadening. Then the various physical phenomena that drive band broadening and how they might be mitigated will be discussed. In the final section, the quantity used to define whether or not a separation is successful (resolution) and how it is calculated will be discussed.

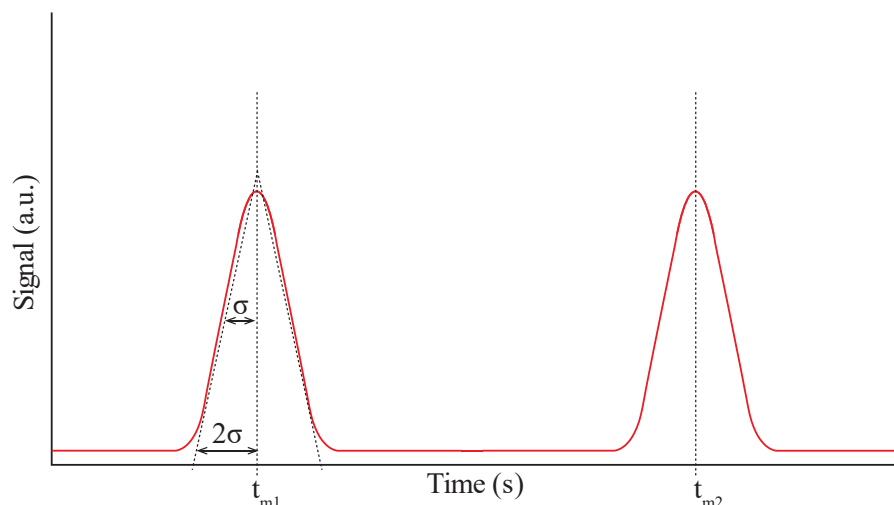


Figure 1.3 An example electropherogram showing two well resolved components with migration times of t_{m1} and t_{m2} . The graphical method for determining peak width by drawing tangent lines at the interior inflection points of peak 1. Assuming a gaussian peak shape, the width can be expressed as 4σ , where σ is the standard deviation of the peak.

1.4.1 Plate height and plate number

The term “plate” came from early separation scientists likening chromatographic columns to distillation columns comprised of a series of narrow plates at which the solute experienced discrete equilibrium events between the mobile and stationary phases.⁶ The height equivalent to a theoretical plate would then be the length of column over which a single discrete equilibrium event occurred. While the theory behind the terminology has since been replaced, the terms plate height (H) and plate number (N) remain in use. For a separation, the efficiency is directly proportional to the number of plates and inversely proportional to the plate height. The relationship between H and N for a given column length (L) by Equation 1.16:

$$H = \frac{L}{N} \quad (1.16)$$

Over the years, separation scientists have attempted to quantify the relationship between band broadening (increased plate height) and the multitude of complex physical phenomena that occur in a separation. While no theoretical equation has been proposed that is capable of accounting for every factor, the van Deemter equation was developed and is widely used as a tool to describe in general how a variety of factors contribute to H:

$$H = A + \frac{B}{u} + Cu \quad (1.17)$$

Where u is the linear velocity of the mobile phase. The van Deemter equation breaks down sources of band broadening into three terms: A is the multipath term and is nominally independent of flow rate, $\frac{B}{u}$ is the longitudinal diffusion term and decreases as flow rate increases, and Cu is the mass transfer term that increases as flow rate increases. Both the A and Cu terms arise from the solid stationary phase in a chromatographic column and therefore do not apply when describing electrophoretic separations. This implies that under ideal conditions H depends solely on diffusion which is given in the Einstein-Smoluchowski equation. The Einstein-Smoluchowski equation can be written in terms of peak velocity (u) and separation length (l_{sep}) by substituting in $t = l_{sep}/u$.

$$\sigma^2 = 2Dt = \frac{2Dl_{sep}}{u} \quad (1.18)$$

Plate height is a measure of variance per unit length and, therefore, may be written in terms of diffusion by dividing Equation 1.18 by l_{sep} :

$$H = \frac{\sigma^2}{l_{sep}} = \frac{2D}{u} \quad (1.19)$$

The expression for N can then be written as:

$$N = \frac{l_{sep}^2}{\sigma^2} = \frac{ul_{sep}}{2D} \quad (1.20)$$

As discussed in Section 1.3, the velocity of a species in an electrophoretic separation is the product of its overall mobility (μ) and the electric field strength(E). Therefore, N can be written in terms of electrophoretic parameters as shown in Equation 1.21:

$$N = \frac{\mu E l_{sep}}{2D} = \frac{\mu V l_{sep}}{2DL} \quad (1.21)$$

Where L is the total length the electric field is applied across (i.e. total capillary length or microchannel length). In capillary or microchip electrophoresis (CE or μ CE) it is common for l_{sep} to be shorter than L because detection can be done at practically any position along the length of the capillary or microchannel. This means that separation efficiency may be increased by detecting further down the length of the capillary or microchannel. Alternatively, separation times may be reduced by detecting closer to the point of sample injection. This offers a clear advantage to CE and μ CE over chromatographic techniques, because the l_{sep} for chromatography can only be altered by changing out the column. Without increasing l_{sep} or altering the separation buffer, the upper limit for separation efficiency in electrophoretic separations is generally dictated by the applied voltage because both μ and D are values intrinsic to the species being separated and the separation buffer used. CE and μ CE separations regularly yield plate counts between 100,000 and 200,000 as compared to those in HPLC which typically range from 5,000 to 20,000.⁶ However, this is not the complete story as CE is not selective but HPLC is. Without

measured values for μ and D , plate number can also be calculated using the migration time (t_m) and the peak width (w) using Equation 1.22:

$$N = 16 \left(\frac{t_m}{w} \right)^2 = 16 \left(\frac{t_m}{4\sigma} \right)^2 \quad (1.22)$$

Where the peak width (w or 4σ) is measured at the baseline graphically by drawing tangent lines at the interior inflection points of the peak, as shown in **Figure 1.3**. The baseline width is the distance between where each tangent line intersects the baseline.

1.4.2 Factors contributing to band broadening

Diffusion limited band broadening discussed in the previous section represents the ideal case for an electrophoretic separation. However, it is not uncommon for a host of other instrumental and physical factors to contribute to band broadening. Assuming each band broadening factor is independent from one another, each contribute to an increase in peak variance additively and are summarized in Equation 1.23.⁵

$$\sigma_{tot}^2 = \sigma_{diff}^2 + \sigma_{inj}^2 + \sigma_{det}^2 + \sigma_{Joule}^2 + \sigma_{geo}^2 + \sigma_{MT}^2 + \sigma_{ads}^2 + \sigma_{edisp}^2 + \sigma_{flow}^2 \quad (1.23)$$

The sources of broadening in Equation 1.23 (listed in order) are diffusion, injection plug length, detection window length, Joule heating, channel geometry, mass transfer, adsorption, electrodispersion, and incidental parabolic flow.

Diffusion is an unavoidable source of band broadening in separations because of the concentration gradient generated upon injection of the sample plug. As described in Equation 1.15, the variance due to diffusion (σ_{diff}^2) is proportional to the diffusion coefficient (D) of the species being separated. The Stokes-Einstein equation defines the diffusion coefficient in terms of the thermal energy and the frictional forces due to the surrounding solution.⁹

$$D = \frac{kT}{6\pi\eta r} \quad (1.24)$$

Where k is the Boltzmann constant, T is the temperature in Kelvin, and the denominator is the friction coefficient where η is the viscosity of the fluid and r is the effective radius of the moving particle.

The contribution of the injection plug length and the detection window length to band broadening are unavoidable but minimal in most cases. Because a sample plug is always going to have a finite starting length (l_{inj}) and, therefore, have a concentration profile. The variance of the injection plug profile is described by Equation 1.25 assuming an impulse (top hat) profile.

$$\sigma_{inj}^2 = \frac{l_{inj}^2}{12} \quad (1.25)$$

This source of band broadening is apparently mostly in rapid separations with short separation distances and can be minimized by ensuring that $l_{inj} < 5\%$ of the distance from injection to detection. For laser induced fluorescence (LIF) detection schemes, the detection window size is either determined by the laser spot size or the size of the detection aperture (pinhole). If the laser spot is smaller than the pinhole, then the gaussian intensity profile of the laser spot determines σ_{det}^2 and is defined by Equation 1.26:

$$\sigma_{det}^2 = \frac{l_{det}^2}{16} \quad (1.26)$$

If, however, the laser spot is larger than the pinhole, then the variance is best described using the top hat profile and can also be calculated using Equation 1.25 substituting in l_{det} . σ_{det}^2 can be considered negligible if the effective aperture is sufficiently small ($< 20 \mu\text{m}$).⁵

As mentioned previously, Joule heating arises due to the frictional drag forces acting on the moving ions that carry the current through the separation medium. The rate at which this phenomenon generates heat (J_Q) is given in Equation 1.27:⁵

$$J_Q = \frac{i^2}{\kappa A^2} \quad (1.27)$$

Where i is the current, κ is the electrical conductivity of the buffer solution ($\Omega^{-1} \cdot \text{cm}^{-1}$), and A is the cross-sectional area of the channel. Joule heating becomes problematic when the heat produced cannot be dissipated at a sufficient rate to prevent the generation of a temperature gradient. The rate of heat dissipation in capillaries and microchannels depends upon factors including the thermal conductivities of the solution, the channel or capillary material and surrounding air as well as the surface areas of the material interfaces. The presence of a temperature gradient leads to a viscosity gradient which can change the flow profile from flat to parabolic because the electroosmotic velocity is dependent upon the solution viscosity. In microchannels, the high specific surface area allows for effective heat dissipation despite the relatively low thermal conductivity of commonly used microchip materials such as poly (dimethyl siloxane) (PDMS) or glass. Excessive Joule heating can also be avoided by using less conductive buffers such as borate.

Channel geometry contributes to band broadening when turns are incorporated into the separation channel. This is usually done to increase the length of a separation without substantially increasing the footprint of a microfluidic device. Because the microfluidic device designs discussed in future chapters do not use turns in the separation channel, this source of band broadening is not relevant. Similarly, the contribution of mass transfer phenomena to band broadening does not apply to the separations that will be discussed because it only pertains to separation techniques that use a stationary phase (e.g. capillary electrochromatography).

Electrostatic interactions between the analytes and the capillary or channel wall are another example of an unavoidable source of band broadening. The high specific surface area of

microchannels is beneficial when it comes to heat dissipation but results in an increased likelihood that adsorption events occur.¹⁰ The degree to which these adsorption phenomena affect the separation efficiency depends on the nature of the species being separated as well as the material of the channel or capillary wall. As mentioned in discussing electroosmosis, the surface of glass capillaries or microchannels consists of silanol groups that can become negatively charged under sufficiently basic conditions. The negative surface charge can cause cationic analytes to adsorb to the surface. Elastomeric materials like PDMS are a commonly used material for microfluidic devices and can potentially adsorb larger biomolecules (e.g. proteins and peptides) via hydrophobic interactions. These adsorption events can be described in a similar manner to stationary phase interactions in chromatography. The contribution of adsorption to band broadening is given in Equation 1.28:¹⁰

$$\sigma_{ads}^2 = \frac{k' u_{eo} l}{(1 + k')^2} \left(\frac{r^2 k'}{4D} + \frac{2}{k_d} \right) \quad (1.28)$$

Where k' is the capacity factor which is defined as: $k' = \frac{t_r - t_0}{t_0}$

t_r is the retention or migration time of the peak, t_0 is the retention time for an unretained molecule, u_{eo} is the electroosmotic velocity, l is the length of the separation channel, r is the radius of the channel, D is the diffusion coefficient of the solute and k_d is the first order desorption rate constant. σ_{ads}^2 can be reduced in glass microchannels by using buffers at an extremely high pH or low pH or with a high ionic strength. These approaches to minimizing σ_{ads}^2 are generally impractical because biomolecules can undergo structural changes at extreme pHs, and Joule heating is more likely to become problematic as buffer conductivity increases. Furthermore, modifying buffer pH and ionic strength does little to improve band broadening in PDMS-based microchannels. Alternatively, channel surfaces can be modified either permanently

through covalent attachment or temporarily through buffer additives such as surfactants or proteins (e.g. bovine serum albumin) that form a dynamic coating.¹¹

Electrodispersion occurs when there is a substantial difference in conductivity between the sample plug and the surrounding separation buffer or when the analyte ion mobility is significantly different to that of the buffer ion. This causes the sample plug to experience a higher or lower local electric field depending on which solution is more conductive or which ion is more mobile. If the sample is less conductive than the buffer, then the local electric field will be higher, causing ions within the sample to migrate more rapidly and concentrate at the front of the sample region. If the sample is more conductive than the buffer, then analyte ions will concentrate toward the rear of the sample plug. Both of these scenarios result in asymmetric peak shapes and can negatively impact the separation efficiency. Electrodispersion can be effectively mitigated by preparing the sample in the separation buffer solution or by matching the conductivity of the buffer to the sample solution. Because electrodispersion causes ions to concentrate at one end of the sample plug, thus counteracting longitudinal diffusion, its contribution to peak variance is not considered to be additive. (Note: The inclusion of σ_{ads}^2 in Equation 1.23 is illustrative and does not reflect its true contribution to total peak variance.)

The final potential contribution to band broadening is the presence of incidental parabolic flow. Parabolic flow can arise from various sources including a viscosity gradient generated because of Joule heating or a difference in reservoir height resulting in a hydrostatic pressure differential. Joule heating can be minimized or prevented as described above. A difference in hydrostatic pressure due to different reservoir heights can be mitigated by maintaining the buffer reservoirs at the same height.

1.4.3 Resolution

Resolution (R_s) is a quantitative metric used to assess whether or not a separation is successful. R_s is a unitless quantity that reflects how well two adjacent peaks have been separated. Using the example electropherogram in **Figure 1.3**, the resolution between components 1 and 2 with migration times t_{m1} and t_{m2} and peak widths of w_1 and w_2 is calculated using Equation 1.29:

$$R_s = \frac{\Delta t_r}{w_{avg}} = \frac{(t_{m2} - t_{m1})}{\frac{w_1 + w_2}{2}} = \frac{2(t_{m2} - t_{m1})}{w_1 + w_2} \quad (1.29)$$

Components are said to be baseline resolved at a resolution of 1.5 or greater, however higher values are desirable when performing quantitative measurements.

1.5 Microfluidics

Microfluidics is a growing field of research in the scientific community that is continually gaining traction. Microfluidics can be defined as the design, fabrication, functionalization, or application of small-scale devices consisting of channels or channel networks with at least one feature dimension being in the microscale (i.e. < 1 mm). Other terms for microfluidic devices include microfluidic chips, lab-on-a-chip (LOC) devices, micro total analysis systems (μ TAS), and other similar terms. Research in the field of microfluidics is highly interdisciplinary and focuses on the prototyping of novel instrumentation for a broad range of applications. The first reported microfluidic device, developed by S.C. Terry et al. in 1979, was a miniaturized gas chromatograph system that was fabricated by etching microchannels into a

silicon wafer.¹² Since then, microfluidic devices have become increasingly sophisticated and have been developed for applications in biological analyses, environmental science, organic chemistry, and others.¹³⁻¹⁴ Key aspects of microfluidic technology that contribute to its growth in popularity include small laboratory footprints, low rates of reagent consumption, rapid analysis times, and lower overall operating and fabrication costs. The purpose of this chapter will be to provide a base understanding of the fabrication, functionality, and application of microfluidic devices. The following sections will first discuss microscale fabrication techniques and technologies, which will lead into commonly used fluid manipulation strategies and will finish with a brief overview of biological applications enabled by microfluidic technology.

1.5.1 Microscale fabrication

Several classes of microscale fabrication techniques have been developed and applied to the field of microfluidics. Early microfluidic devices were fabricated using microscale fabrication technologies developed for early silicon-based sensors and transducers.¹² Methods such as injection molding and hot embossing use temperature and pressure to shape thermoplastics into microfluidic devices.¹⁵ There are also so-called “direct write” methods such as micromilling and 3D printing (specifically fused deposition modeling) that use a computer numerical control (CNC) system to move a tool head to cut away material or hot extruder to deposit layers of plastic in order to form the desired structures.¹⁶⁻¹⁷ While injection molding and hot embossing have the advantages of high-throughput and low-cost production, they have the disadvantages of prohibitively high startup costs, require large machinery, and an incompatibility with rapid prototyping. Conversely, micromilling and 3D printing have relatively low startup costs, smaller footprint, and are well-suited for rapid prototyping, however they are primarily

limited in feature resolution capabilities.¹⁵ (Note: Despite 3D printing's current limitations for microscale fabrication, it still plays a role in the microfluidic research lab and will be discussed in later sections.)

Perhaps the most popular fabrication strategy for microfluidics is polydimethylsiloxane (PDMS) casting.¹⁸ PDMS casting has a relatively low startup cost and is capable of high fidelity feature replication of microstructures down to 1 μm or smaller.^{15, 19} As a material, PDMS also offers advantages, including optical transparency, biocompatibility, tunable elasticity, compatibility with multilayer fabrication, among others. This fabrication method is limited, however, primarily due to difficulties with scaling up production. Despite this issue, a number of commercially available PDMS casted devices have been developed because the advantages of using PDMS as a material outweighed the challenges in production scaling.²⁰

The process of PDMS casting begins with the fabrication of a master mold that contains all the channels and features that will be replicated in the PDMS. The most common method for master mold fabrication is by photolithographic patterning onto silicon wafers. Photolithographic molds are made using either positive- or negative-tone photoresists. A photoresist is a light sensitive polymer that when exposed to UV light, either becomes cross-linked (negative-tone) or breaks down (positive-tone). The design is transferred to the photoresist by exposing it to intense UV light through a photomask that blocks or allows the transmission of the light in the desired pattern. Following exposure, the wafer is placed into a bath of developer (photoresist-specific solvent) that removes any unwanted photoresist, leaving the desired pattern as positive features on the silicon wafer. Once a master mold is made, it can be used repeatedly to make many PDMS devices. The general process is illustrated in **Figure 1.4**.

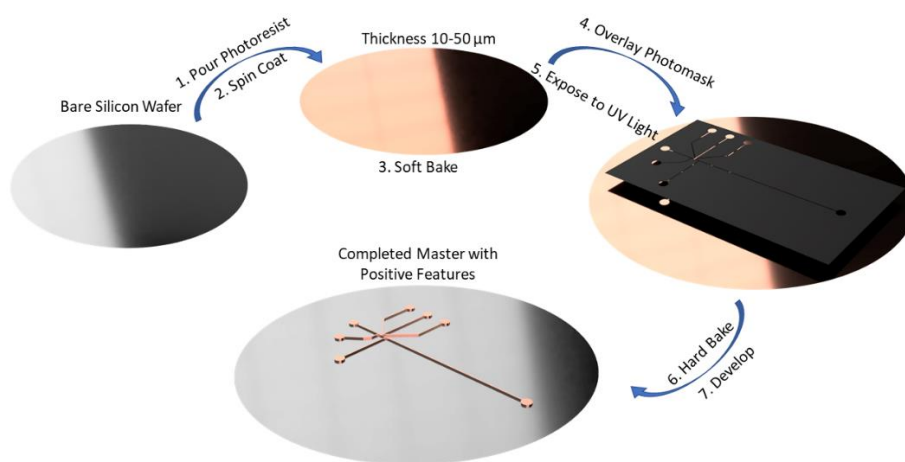


Figure 1.4 A generalized workflow for the process steps of photolithographic micropatterning.

The positive features on the silicon wafer master mold can then be transferred into PDMS using soft lithography. The general process for PDMS-based soft lithography is shown in **Figure 1.5**. PDMS is sold as a 2-part kit consisting of liquid elastomer base and curing agent. The 2 parts are mixed at a 10:1 ratio by weight (elastomer base to curing agent), degassed, and poured over the desired features to be replicated. The cast is then cured after 90 min at 80 °C or 48 hours at room temperature. Once fully cured, the device is carefully peeled, and fluid reservoirs can be punched out using a disposable biopsy punch. The positive features on the master mold are cast as recesses in the PDMS device. Fluidic channels are completed by sealing the device reversibly or irreversibly to a glass slide or other substrate. Reversible sealing of PDMS to substrates, such as glass, is achieved via conformal bonding, and the reversibility of this type of bonding can be attributed to the low surface energy of PDMS.²¹ Permanent bonding of PDMS to substrates requires surface activation via oxygen plasma treatment, however, this type of bonding is only necessary for applications requiring the application of high fluidic pressure.

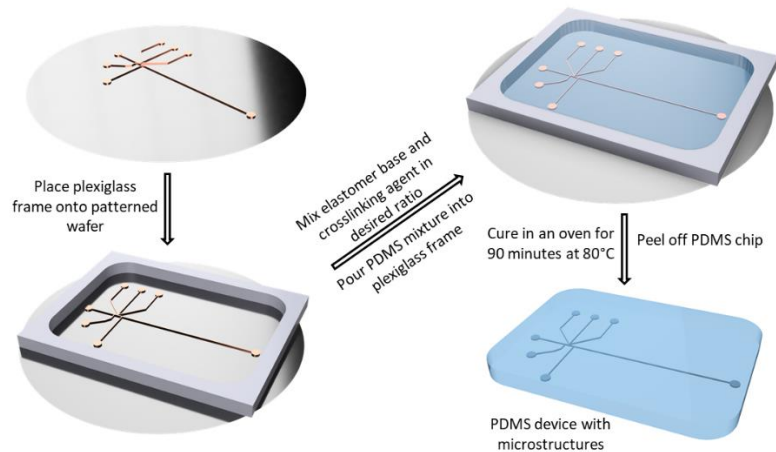


Figure 1.5 A generalized workflow for the process steps for the fabrication of a 1-layer PDMS-based microfluidic device using soft lithography.

Beyond 1-layer microfluidic devices, PDMS casting is uniquely amenable to multilayer device fabrication. The process and potential applications of multilayer soft lithography were detailed in a publication by the Quake group the year 2000.²² Quake et al. demonstrated the capabilities of multilayer soft lithography by fabricating a device with 7 patterned layers. More importantly, they showed how multilayer fabrication enabled them to integrate vital functional components for fluidic systems such as valves and pumps. The bonding between layers within a multilayer device is achieved by mixing the 2 parts at ratios such that the lower layer has an excess of elastomer base and the upper layer has an excess of curing agent. The mixtures are poured over their respective master molds and partially cured separately, then the upper layer can be peeled off and layered on top of the lower layer. Both layers are then placed back into the curing oven where the complementary composition of each layer causes them to bind irreversibly. The process for a 2-layer device is illustrated in **Figure 1.6**.

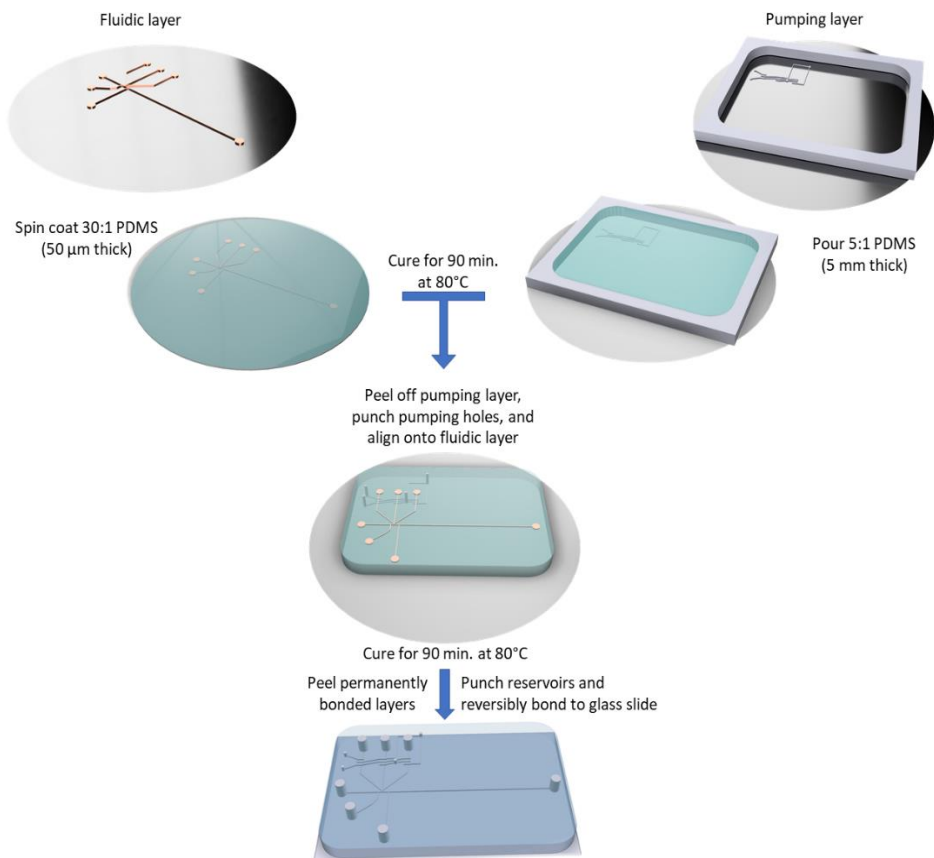


Figure 1.6 A scheme illustrating the process of multilayer microfluidic device fabrication. The device design shown and the details of each step pertain specifically to the fabrication of the single cell analysis device reported by the Culbertson research group.¹

1.5.2 Fluid Manipulation

Fluid manipulation is considered anything that generates or controls fluid flow in a channel or fluidic manifold. Because electroosmotic flow was discussed in previous sections, this section will focus on pressure- or actuation-based fluid manipulation. Approaches to fluid manipulation can be generally classified as either passive or active. One commonly used passive method to generate fluid flow is a hydrostatic pressure differential that is generated when fluid reservoirs are filled to different heights. The difference in fluid height results in a siphon effect. While this method is by far the simplest, the flow generated is relatively slow and difficult to

reproduce. Active fluid manipulation, however, can be achieved either by using a piece of peripheral equipment (e.g. syringe or peristaltic pump), or through on-board components such as integrated valves and pumps. While peripheral equipment is generally simpler to implement, their larger footprint, higher cost, and difficulty with real-time flow adjustments make them less attractive options when compared to integrated fluid control strategies. The most widely used integrated valving technique was first described by the Quake group in 2000.²² The so-called “Quake valve” is a 2-layer design shown in **Figure 1.7A**. The upper layer functions as the control and is connected to an external compressed air source that can be turned on or off using an electronically controlled solenoid valve. The fluidic channels in the lower layer are cast using a photoresist that results in a rounded channel profile. When the valve is actuated, the control layer inflates and presses downward on the fluidic channel, and the rounded channels allow for the valve to close completely. Beyond functioning as a valve, the Quake group demonstrated an integrated peristaltic pump comprised of 3 Quake valves in series. As the valves close, the fluid underneath is displaced laterally along the length of the channel. Unidirectional flow, via peristalsis, can be generated by actuating each of the 3 valves using a series of square waves that are 120° out of phase from one another. A diagram of this type of integrated peristaltic pump is shown in **Figure 1.7B**.

Integrated pumping is a powerful capability that minimizes overall device footprint, cost, and allows for precise flow control. However, flow rates generated by a single pump are limited, and the flow is pulsatile. Higher flow rates and smoother flow can be achieved by connecting multiple sets of pumps in parallel. A layout of this style of manifold is shown in **Figure 1.7B**. The Culbertson group has reported a single-cell analysis device that features a set of these integrated pumps.¹ The pumps provide a means of transporting suspended cells toward an

electrophoretic separation channel. The pumping flow rate of the multiplexed pumps was assessed at varying actuation pressures and frequencies and compared to a single pumping unit. The flow rates generated by the multiplex pumps were 2.2-3x higher than the single pumps. The optimal actuation frequency was found to be around 100 Hz. Higher actuation frequencies resulted in partial valve closure and lower frequencies caused the flow to be more pulsatile. The device design reported serves as the basis for the microfluidic device discussed in later chapters.

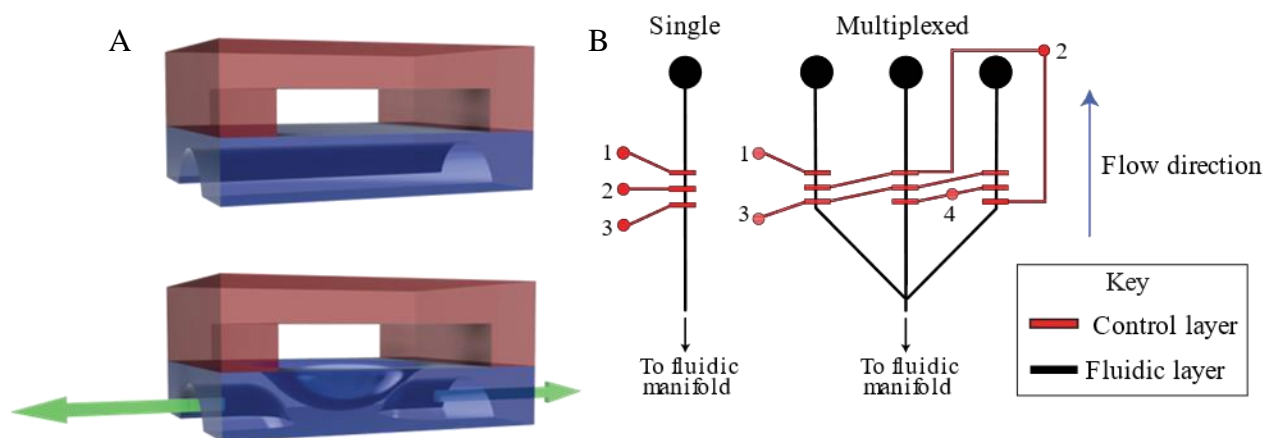


Figure 1.7 (A) A 3D drawing illustrating the actuation of a Quake-style valve both opened (top) and closed (bottom). Green arrows on the closed valve indicate the direction of fluid displacement. (B) Diagrams illustrating single (left) and multiplexed (right) integrated peristaltic pumps. The numbered circles represent the input ports for compressed air. The diagram of the multiplexed peristaltic pumps is based on designs reported by the Culberson group.^{1,3-4}

1.5.3 Microfluidics and single-cell analysis

Traditional cellular analysis has allowed for significant advances in the diagnosis, study, and treatment of chronic illnesses including cancers and neurodegenerative diseases. However,

results yielded from traditional “bulk cell analysis” only give population averaged information and are incapable of providing deeper information about the distribution of the a cell population. There is a high degree of heterogeneity within cellular populations, both healthy and diseased, that is obscured in population averaged data. For example, sub-populations within a tumor can possess genetic differences that impart characteristics such as chemotherapeutic resistance as well as increased invasiveness and are undetectable with bulk cell methods.²³ Similarly, cells can exhibit non-genetic heterogeneity that arises from variations in protein expression levels and can result in vastly different cellular responses to extracellular stimuli within a population.²⁴ In both cases, these variabilities can make chronic illnesses difficult to diagnose, study, and treat effectively.

The field of microfluidics has played a pivotal role in enabling chronic illnesses to be studied at the single-cell level. Several aspects of microfluidic devices make them especially well-suited for single cell analysis applications. Cells and microfluidic channels are similar in scale (microns) which allows for precise and gentle manipulation of cells and minimal dilution of intracellular contents upon lysis. Additionally, microfluidic devices are commonly fabricated using materials that are biocompatible and translucent which enables easy observation of cells under a microscope during analysis. Microfluidic devices are frequently designed to perform multiple functions in a single device. For example, the single cell analysis device reported by the Culbertson group (referenced in section 1.5.3) is capable of transporting and lysing cells as well as separating and quantifying intracellular analytes all in a matter of seconds. In bulk cell analysis several minutes transpire between lysis and quantitation due to centrifugation and sample loading steps. This may result in a less accurate picture due to continuing enzymatic reactions or degradation of analytes with short half-lives. For instance, some enzymatic signaling

reactions occur on time scales that can cause analyte concentrations to change significantly in under 1 second.²⁵

Standard techniques, like flow cytometry, have some commonalities with microfluidic single cell analysis in that they measure at the single-cell level. In flow cytometry, cells are treated with a fluorescent reporter that undergoes some change in fluorescence upon reacting with an enzyme or biomolecule of interest. Cells are then loaded into the flow cytometer where they flow single file through a fluorescence detection system. Flow cytometers are often equipped with multiple excitation sources and emission detectors allowing for multiple fluorescent reporters with different excitation and emission spectra to be quantified simultaneously. However, flow cytometry is limited in terms of the number of analytes that can be quantified simultaneously within a cell. This method is also unable to distinguish between fluorescence caused by the desired reporter-analyte interaction and reporter-interferent interactions. The Culbertson group's microfluidic single cell analysis device has the added advantage of incorporating automated electrokinetic lysis and electrophoretic separation of intracellular contents. By incorporating a mode of separation into the cellular analysis technique, multiple cellular parameters can be measured simultaneously without additional wavelengths of excitation and detection, and interfering species can be identified and accounted for due to their characteristic electrophoretic migration time.

1.6 Measuring nitric oxide

The projects described Chapters 2 and 3 demonstrate the application of microfluidic single-cell analysis for the measurement of an inflammatory biomarker nitric oxide. Nitric oxide (NO) is a fundamental intercellular signaling molecule that is associated with the control and regulation of many major cellular functions including immune response,²⁶ anti-inflammatory

response, and neurotransmission.²⁷ Increased levels of NO can lead to nitrosative stress states in cells that can cause damage to DNA or disrupt certain enzymatic activities.²⁸ The effects of nitrosative stress have been linked to several chronic illnesses including neurodegenerative and cardiovascular diseases as well as a number of different cancers.²⁷ NO exists *in vivo* as a dissolved free radical gas, with an unpaired electron on the nitrogen. It is produced in cells by a family of nitric oxide synthase enzymes (NOS): endothelial nitric oxide synthase (eNOS), neuronal nitric oxide synthase (nNOS), and induced nitric oxide synthase (iNOS). Upon reaction with the superoxide anion (O_2^-), NO forms the highly reactive species peroxynitrite ($ONOO^-$). Peroxynitrite can cause substantial damage to biological systems through nitration, nitrosylation, and the oxidation of proteins, DNA, and lipids. The ability to monitor the production of NO may aid in the understanding of its role in the progression of these diseases. However, NO has a relatively short half-life (3-6 s),²⁷ and therefore analysis must be performed rapidly to obtain accurate measurements. Recently, advances in nanoelectrode techniques for the electrochemical detection of intracellular NO, and other RNOS, have been applied to the measurement of single cells.⁷ However, these techniques are limited in throughput and are most useful in studying individual cells rather than larger cell populations. Rapid and sensitive measurement of intracellular NO may be achieved using DAF-FM DA (4-amino-5-methylamino-2',7'-difluorofluorescein diacetate). DAF-FM DA is a non-fluorescent, membrane permeant molecule that may passively diffuse across cell membranes. Upon entry into the cell, it is deacylated by intracellular esterases, forming a membrane impermeant species, DAF-FM. It then reacts further with NO to form a highly fluorescent benzotriazole derivative reporter (DAF-FM T). To account for differences in loading efficiency, esterase activity, and cell volume an internal standard 6-carboxyfluorescein diacetate (6-CFDA) can be added, as it is structurally similar to DAF-FM DA

and is also deacylated by esterase enzymes to form 6-carboxyfluorescein (6-CF) within the cells.²⁹ The reaction scheme for both DAF-FM DA and 6-CFDA are shown in **Figure 1.8**. DAF-FM T and 6-CF can be quantified in single cells using the microfluidic single-cell analysis device mentioned in the previous section. This analytical strategy is capable of achieving high-throughput single-cell measurements of intracellular NO. Application of this strategy for the analysis of NO levels in T lymphocytes and microglia is demonstrated and discussed in Chapters 2 and 3 respectively.

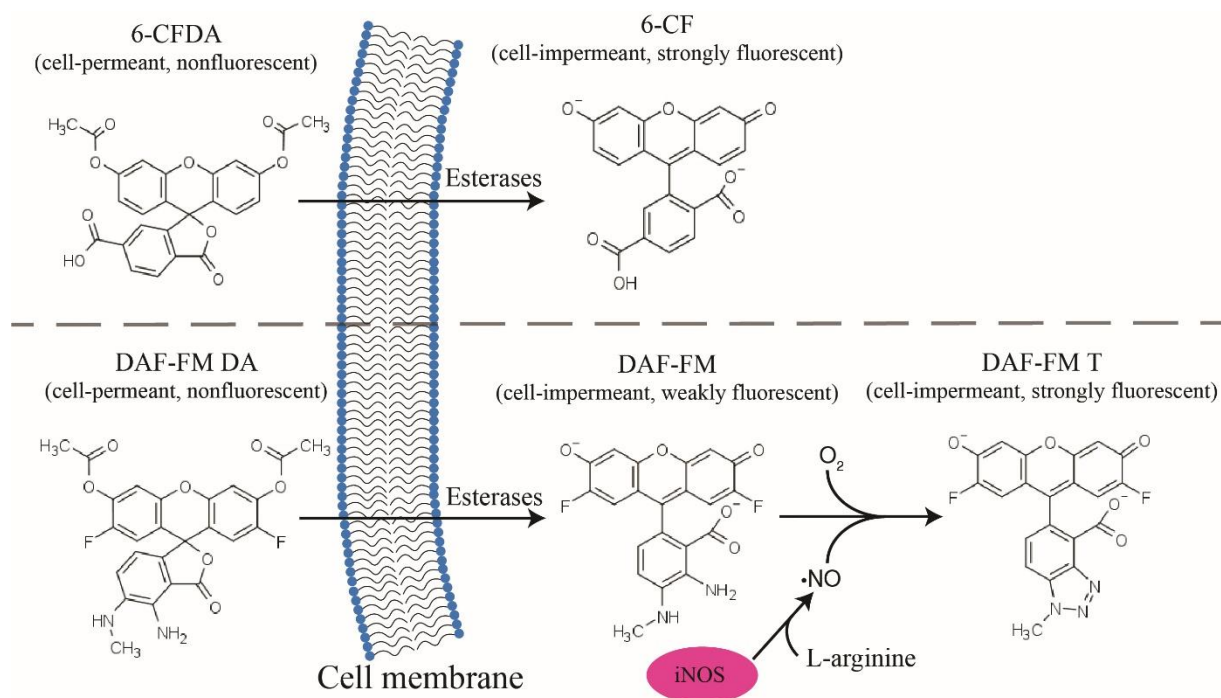


Figure 1.8 Reaction scheme for the loading of 6-CFDA (top) and DAF-FM DA (bottom) into cells; Both fluorescent probes are modified by intracellular esterases, DAF-FM reacts further with NO to form the strongly fluorescent DAF-FM T derivative.

1.7 DIY technologies in the research laboratory

1.7.1 3D printing

The emergence of 3D printing technology has greatly increased the turnover rate and lowered the expense of prototyping compared to traditional machining and fabrication methods, allowing for rapid designing and testing of custom-built parts. 3D printers are used to make objects ranging from simple custom-built housing and fittings³⁰⁻³¹ to parts that require higher precision such as optical components and adapters.³² 3D printing is part of a rapidly growing DIY community that is centered around the culture of sharing ideas and collaborative problem solving. As a result, a number of useful resources are readily available online including extensive tutorial videos for all levels of 3D printing experience and websites, such as Thingiverse.com, where users can share their 3D designs and other members of the community may download them for free. The largest expense in 3D printing is the initial investment in the printer itself. However, a number of “economical” options are available, costing ~\$250 USD for a low-end printer, ~\$500 USD for a mid-range printer, and \$1,000+ USD for higher quality. The versatility and low-cost of this technology make 3D printers a powerful tool in the microfluidics research lab.

3D printing technology comes in a number of varieties, but the 2 most popular formats are fused deposition modeling (FDM) and stereolithographic printing (SLA). Both formats of 3D printing fabricate parts in a layer-by-layer fashion. 3D objects are first designed in a 3D modeling software environment such as AutoCAD or Fusion 360. The 3D object files are then imported into a “slicing” software that converts the 3D object into a machine code that can be understood by the 3D printer. In SLA printers, a printing surface is lowered into a UV curable liquid resin containing vat with a transparent plastic film bottom. A UV light source from

underneath cures the resin in the desired pattern using either a laser guided by 2 mirrors, or an array of UV LED pixels. It is worth noting that in recent years, there have been more user-friendly SLA printers that have come on to the market which will likely result in their increased use in the research lab. While this style of printing is capable of producing high-resolution features (tens of microns), the liquid resins used are toxic and printers are more difficult to maintain compared to their FDM counterparts. FDM printers (alluded to in **Section 1.5.1**) work by using a CNC controlled heated extrusion nozzle to deposit thin lines of thermoplastic onto a heated print surface. The nozzle follows paths computed in the slicing software to construct each layer of the printed object. FDM printers can produce objects with resolutions of ~10+ microns in the XY direction and 100-300 microns in the Z direction. FDM is the most popular format among 3D printing hobbyists because it is more user friendly, lower maintenance, does not use toxic liquid resin, and tends to be less expensive overall. The most commonly used material for FDM 3D printing is polylactic acid (PLA) as it is biodegradable, prints at or below 220°C and does not require a heated print bed. PLA filament can be purchased for \$23/kg and is one of the most inexpensive material choices available, and printed items often cost less than \$1 to print. Other materials for 3D printers are also available when different properties such as increased structural stability or chemical resistance are required.

1.7.2 Low-cost open-source electronics

The development of microfluidic devices often requires a set of specialized electronic components for device control and monitoring functionality as well as a custom graphical user interface (GUI). Companies like National Instruments (NI) have produced tools that meet these requirements such as GUI development software (LabVIEW) and accompanying

microcontrollers (NI-DAQ devices). While these NI products are useful in prototyping, they can be prohibitively expensive and can effectively negate the low-cost aspect of microfluidics. In recent years, open-source microcontroller boards, such as Arduino (**Figure 1.9**), have become powerful, simple, and inexpensive alternative. Open-source microcontrollers are also a part of the DIY community, and as such, benefit from a large online support community that makes it relatively easy for hobbyists and scientists to rapidly program and integrate electronic devices into their setups. There is also a wide selection of auxiliary components, or “breakout boards”, that enable a broader range of functionality for these microcontrollers, including temperature sensing, gas sensing (CO₂, O₂, VOCs), magnetometers, accelerometers, pH probes, among many other analog and digital I/O functionalities. Arduino microcontrollers have begun to find their place in the research lab due to their low-cost and high versatility.³³⁻³⁷



Figure 1.9 A photograph of an Arduino UNO R3 microcontroller board.

Photograph: “Arduino Uno-R3” from SparkFun Electronics [CC BY 2.0
(<https://creativecommons.org/licenses/by/2.0/legalcode>)]

The proliferation of low-cost open-source microcontrollers and accompanying accessories largely began with the Arduino. An Arduino microcontroller is a printed circuit board (PCB) that is centered around a microprocessor chip and comes assembled with all the necessary components (resistors, diodes, voltage regulators, etc.) and is ready to use out of the box. Programmed instructions for the Arduino can be written in the Arduino integrated development environment (IDE) and transferred to the on-board flash memory via a USB cable. Components such as break out boards and other low-power electronics can then be connected to the I/O ports via standard female headers. Because the designs for the original Arduino board are open-source, other companies can manufacture less expensive versions or add their own built in features as desired, making Arduino-style boards costing as little as \$5 USD.

1.7 Conclusion

Thus far, a general overview of the underlying concepts and recent trends for microfluidic biological analysis have been discussed. Microfluidics is a relatively young and rapidly growing area of research that has proven to be incomparable in terms of potential for bioanalytical applications in a variety of settings, such as point-of-care diagnostics, in vitro cellular analysis, and single-cell analysis. The following chapters will present and discuss results and progress on 3 microfluidic-based projects. Chapter 2 reports improvements made on the single-cell analysis (SCA) system developed by the Culbertson group. The improvements made to the SCA system were enabled by low-cost electronics and 3D printing technology. The system is then applied to the analysis of an inflammatory biomarker (nitric oxide, NO) within a model cell line (Jurkat, T-lymphocytes) under inflammatory, native, and inhibitory conditions. Chapter 3 incorporates all improvements reported in Chapter 2 and demonstrates the potential of the SCA

system for applications in studying the effects of anti-inflammatory therapeutics for the treatment of neurodegenerative pathologies, such as Alzheimer's disease, Parkinson's disease, chronic traumatic encephalopathy, among others. An analytical strategy, similar to that developed in Chapter 2, is used to measure NO levels in a recently discovered immortalized cell line (SIM-A9, microglia). Microglia are directly related to the pathologies of interest and studying their behavior in response to pharmacological agents can provide valuable information for the development of more effective therapeutics. Additionally, Chapter 3 presents an interesting in-depth statistical analysis on the distributions of NO levels under inflammatory, native, and inhibitory conditions, which highlights the potential depth of information made available by performing analyses with single-cell resolution. Finally, Chapter 4 focuses on efforts toward replacing bulky pneumatic-based actuation with solid-state actuation using dielectric actuators. The ultimate goals of the project are to use dielectric actuators for 2 functions within microfluidic devices: to apply precise mechanical stress on cells to study mechanotransduction phenomena, and to serve as the basis for a novel non-pneumatic valve.

Chapter 2 - Improvements on fabrication and operation of a single-cell analysis device for the measurement of nitric oxide production in T lymphocytes

2.1 Introduction

Integrated microfluidic devices have become very versatile tools for biological and biomedical investigations.¹³⁻¹⁴ Devices capable of single-cell analysis (SCA), in particular, have proven useful in the study of the etiology of several chronic illnesses including cardiovascular disease³⁸, neurodegenerative diseases,²⁹ and cancers.³⁹ The SCA devices presented in these studies address key challenges in the analysis of diseases, such as heterogeneity within the affected cell populations and the tendency of enzyme activities to change on relatively short time scales.

Microchip electrophoresis coupled with laser induced fluorescence detection (μ CE-LIF) is among the more powerful modes of SCA due to the combination of automated cell handling enabled by microfluidics, the speed of electrophoretic separations, and the sensitivity of LIF detection. There are several current analysis methods that use fluorescent probes to measure the activity of enzymes such as kinases⁴⁰⁻⁴¹ proteases,⁴² nitric oxide synthases, and oxidases.^{28-29, 43-44} Some of these probes directly measure enzyme activity using fluorescently labeled peptide probes while others measure the products of enzyme activity (i.e. nitric oxide and superoxide) using reactive fluorescent moieties. These methodologies are readily adaptable to μ CE-LIF device.

For several years, our research group has been developing an automated high-throughput single cell μ CE-LIF device or single-cell analysis (SCA) device. Previous reports using the SCA

device demonstrated the measurement of NO production in an immortalized T lymphocyte cell line (Jurkat) using a diaminofluorescein based probe (4-amino-5methylamino-2',7'-difluorofluorescein diacetate) or DAF-FM DA.²⁹ Cells were transported from the sample reservoir to the separation channel using a syringe pump in withdrawal mode to pull the fluid. Once the cells entered the separation channel, the high voltage applied for the separation caused the cells to rapidly lyse and the intracellular contents to be injected and separated via electrophoresis. LIF detection was positioned downstream of the lysis intersection where fluorescent analytes in the lysate were detected. Unfortunately, the report did not demonstrate any pharmacological perturbation of the cells to demonstrate the potential of this device for measuring changes in NO production. Since that report, there have been two additional functional components integrated into the SCA device. First, an integrated peristaltic pump was developed to enable on-board fluid control for automatic cell transport from the sample reservoir to the separation channel replacing the external syringe pump.¹ However, the report focused primarily on the functionality of the integrated pumps and did not demonstrate the device's application to a relevant cellular analysis. Additionally, the automatic transport of cells into the lysis intersection is stochastic and uncontrolled, and it is common for two or more cells to enter the lysis intersection in quick succession resulting in electropherogram overlap when multiple analytes are being quantified. The cell density of the sample can be decreased to minimize this possibility; however, this comes at the cost of decreased throughput. While species can, in some cases, be identified with reasonable confidence using their relative migration times, this becomes increasingly difficult as more analytes are added to an analysis. In separations, species can be more confidently identified by their absolute migration times. To that end, the second functionality developed was an integrated optical fiber bridge which enabled fluorescence

detection at two locations simultaneously without additional bulky optics.³ LIF detection spots were placed in the sample channel just before the lysis intersection to detect intact cells and downstream of the lysis intersection to detect separated fluorescent analytes. Detection at these locations allows for the measurement of injection time and separation time which are necessary to calculate or confirm the absolute migration time of separated species. Unlike the report of the integrated pumps, the optical fiber bridge report did demonstrate the application of the device for a relevant cellular analysis, however only preliminary data was reported. The goal of the work presented in this chapter is to combine the added functionalities of the SCA device with a demonstration of its use for a relevant cellular analysis. The SCA device with integrated pumps and optical fiber bridge is used to measure changes in NO production in single Jurkat cells using the DAF-FM fluorescent NO probe and 6-carboxyfluorescein diacetate (6-CFDA) as an internal standard. Additionally, improvements in the optical fiber bridge detection setup are reported.

2.2 Materials and methods

2.2.1 Reagents and materials

T-lymphocyte cells (Jurkat, Clone E6-1, ATCC TIB-152), RPMI-1640 medium (ATCC 30-2001) and Dulbecco's phosphate buffered saline (D-PBS, 1x, ATCC 30-2200) were purchased from American Type Culture Collection (Manassas, VA). Sodium borate, lyophilized bovine serum albumin (BSA), Tween-20, Xylenes (Certified ACS), and acetonitrile (HPLC grade) were all obtained from Fisher Scientific (Pittsburgh, PA). Sodium dodecyl sulfate, anhydrous dimethyl sulfoxide, 99.9% (DMSO), and lipopolysaccharides (LPS) from *Escherichia coli* line 0111:B4 were purchased from SigmaAldrich (St. Louis, MO). 4-Amino-5-methylamino-2',7'-difluorofluorescein diacetate (DAF-FM DA) was purchased from Invitrogen, (Waltham, MA), in 50 µg packs. 6-Carboxyfluorescein diacetate, single isomer (6-CFDA) and

probenecid sodium salt were purchased from Biotium Inc. (Fremont, CA). The iNOS inhibitor, 1400W dihydrochloride, was purchased from Tocris (Minneapolis, MN). Negative tone photoresist SU-8 2010 was purchased from MicroChem Corp. (Newton, MA). The SU-8 developer, 2-(1-methoxy) propyl acetate (99%), was obtained from Acros (Morris Plains, NJ). AZ P4620 positive tone photoresist and AZ 400K developer (1:4) were obtained from AZ Electronic Materials (Branchburg, NJ). Silicon wafers (100 mm diameter, single-side polished, mechanical grade or better) were purchased from Silicon, Inc. (Boise, ID). Chrome coated silicon wafers (100 mm diameter, single-side polished, test grade) were purchased from WRS Materials (San Jose, CA). (1,1,1,3,3,3-Hexamethyldisilazane (98%) (HMDS)) was purchased from Gelest (Morrisville, PA). Sylgard 184 PDMS prepolymer and curing agent were purchased from Dow Corning (Corning Inc., Corning, NY). Ultrapure water was generated from a Barnstead E-pure system (Dubuque, IA). Multimode optical fiber (0.22 NA, core Ø105 µm) and refractive index matching gel (G608N3) was obtained from Thorlabs Inc. (Newton, NJ).

2.2.2 Tissue culture

Cells were cultured in RPMI 1640 medium containing 10% (v/v) fetal bovine serum, L-glutamine (2 mM), penicillin (100 µg/mL), and streptomycin (100 µg/mL). The cells were maintained in a humidified environment at 37 °C and 5% CO₂ and cultured in 25 mL polystyrene culture flasks (Corning Cell Culture Treated, Fisher Scientific). Cells were passaged every 2–3 days. All experiments were scheduled to ensure that the cell density would be approximately 10⁶ cells/mL immediately prior to labeling.

2.2.3 Sample preparation

LPS stimulation and iNOS inhibition

LPS, or lipopolysaccharides, are a class of molecule that are the major constituent of the outer membrane of gram-negative bacteria. LPS is known to stimulate the expression of iNOS via toll-like receptor 4 (TLR4)-mediated signaling and is commonly used for this purpose in studies of the inflammatory response.⁴⁵ In this study, Jurkat cells were stimulated using purified LPS at a rate of 3 μ L of 1 mg/mL LPS per milliliter of cell suspension at a density between 1×10^5 and 1×10^6 cells/mL. Cells were incubated with LPS at 37 °C and 5% CO₂ for 3 hours prior to loading with DAF-FM DA and 6-CFDA.

For iNOS inhibition experiments, 1400W dihydrochloride was used. 1400W dihydrochloride is a potent inhibitor and is selective for iNOS over the other NOS isoforms, namely nNOS and eNOS.⁴⁶⁻⁴⁷ Inhibition occurs through modification of the heme cofactor and destabilization of the iNOS homodimer rendering the iNOS monomers inactive.⁴⁷ In experiments, Jurkat cells were co-treated with 1400W dihydrochloride (100 μ M) and LPS using the same concentration and incubation conditions as the stimulation experiments.

Loading of cells with DAF-FM DA and 6-CFDA

Native, stimulated, and inhibited cells were labeled using the same procedure and similar to that reported previously.²⁹ A stock solution of the fluorogenic NO probe, DAF-FM DA, (approx. 1 mM) was prepared by dissolving the contents of single pack in 100 μ L of DMSO. A separate stock solution of internal standard, 6-CFDA (3.74 mM), was also prepared using DMSO. To prevent the efflux of the anionic dyes probenecid, a commonly used inhibitor of MRP1⁴⁸, was used. Stock solution of probenecid was prepared by dissolving 77 mg in 1 mL of

PBS yielding a final concentration of 250 mM. An amount of 1 mL of cell suspension was aliquoted into a 1.5 mL Eppendorf tube and then centrifuged at 125xg (Marathon 8K, Fisher Scientific, Pittsburgh, PA) for 5 min. The supernatant was removed from the pellet and discarded. Cells were resuspended in a mixture containing 1.1 μ L of 6-CFDA stock solution, 15 μ L of DAF-FM DA stock solution, 1 μ L of probenecid stock solution and 82.9 μ L sterile PBS (100 μ L total) and incubated for 30 min at 37 °C on a heat block. The labeled cells were then diluted to 1 mL with sterile PBS prewarmed to 37 °C and centrifuged at 125xg for 5 min, and the supernatant was then discarded. These rinsing steps were repeated twice more with 1 mL portions of sterile PBS followed by a final resuspension in 1 mL of sterile PBS containing 2 mg/mL BSA and 2.5 mM probenecid.

2.2.4 Device design and working principles

The working principles and operation of the microfluidic device, integrated soft lithographic pumps, and integrated optical fiber detection were described in depth previously.^{1,3} A diagram of the fluidic (black) and pumping (red) manifold for the device is shown in **Figure 2.1**. Labeled cells are loaded into the sample reservoir (labeled S) and drawn to the lysis intersection via hydrodynamic flow generated by the on-board peristaltic pumps (shown in red). A diagram illustrating the processes of cell transport and lysis is shown in **Figure 2.2**. Fluorophores within the intact cells are excited as they pass underneath the cell detection point (labeled CDP). The emission is then transmitted back through the fiber to the photomultiplier

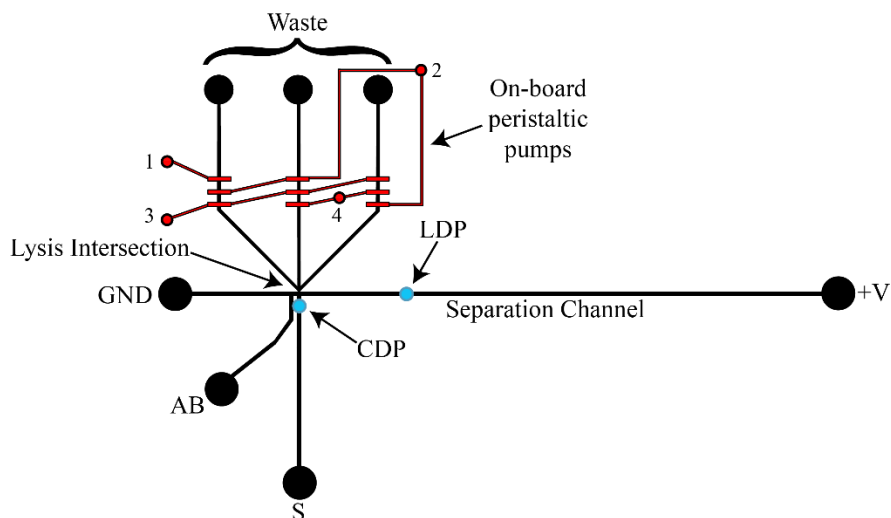


Figure 2.1 Diagram of the single cell μ CE-LIF device; Pneumatic inlets for the peristaltic pumps are numbered 1-4. HV electrodes connected to the positive voltage source and ground are placed into the +V and GND reservoirs, respectively. The Waste, GND, +V, auxillary buffer (AB) reservoirs are filled with electrophoresis buffer. Cells are loaded into the sample (S) reservoir. Locations for both ends of the optical fiber are shown as the cell detection point (CDP) and the lysate detection point (LDP).

tube (PMT) resulting in a sharp emission spike, labeled as intact cell in the electropherogram in **Figure 2.3**. Upon entry into the lysis intersection, the cells experience a high electric field (800-1100 V/cm). This electric field rips the cell membrane away from the charged intracellular contents, lysing the cell. As lysis occurs, the cell membrane and other debris continue with the hydrodynamic flow toward the pumps and waste reservoirs (labeled Waste). Simultaneously, the charged analytes are automatically injected toward the oppositely charged electrode (in the

diagram example it is the anode) and the downstream lysate detection point (labeled LDP) resulting in emission spikes from separated fluorescent analytes (shown in **Figure 2.3**).

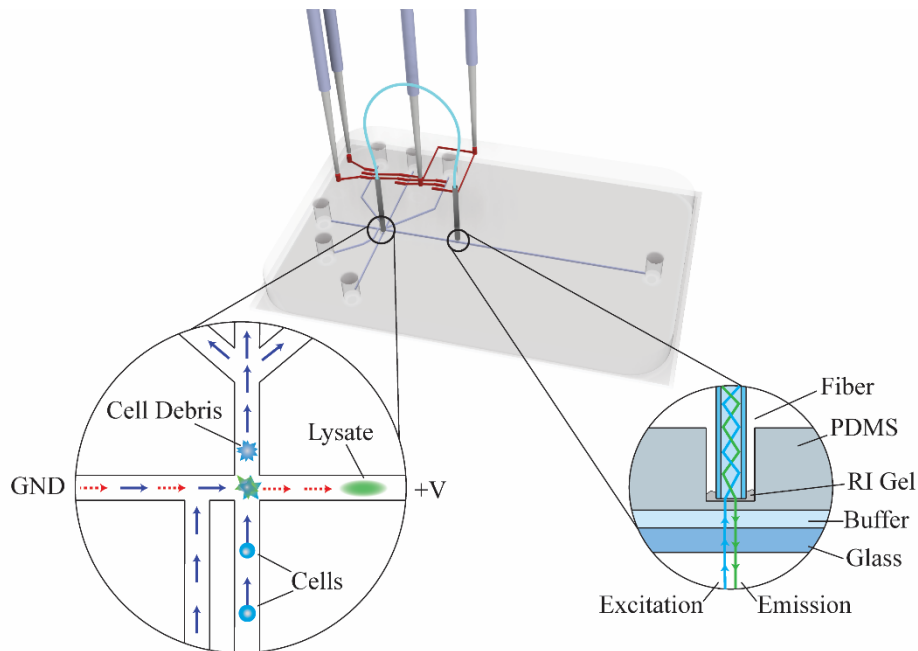


Figure 2.2 3D render of the SCA device with integrated fiber bridge. (Lower left) A diagram of the cell transport and lysis processes; The red dotted arrows represent the electrophoretic flow and the solid blue arrows represent the hydrodynamic flow direction. (Lower right) A diagram showing the optical path that the excitation (blue) and emission (green) light travels, and the application of the RI gel to the fiber-membrane interface.

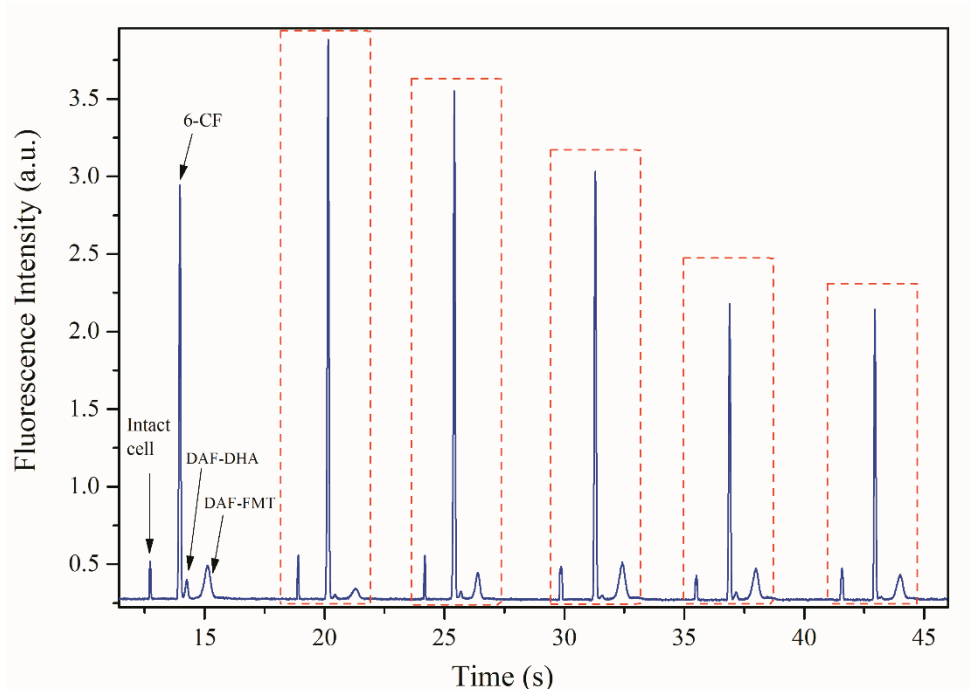


Figure 2.3 A series of single-cell electropherograms. The intact signal and separated lysate contents are labeled for the first cell, and subsequent cells are indicated by the dotted rectangles.

Our device has a few key features that set it apart from other microfluidic SCA systems. The integrated peristaltic pumps allow for simple and precise control of flow rate within our device. Our pumping manifold consists of 3 parallel pumping channels. Each pumping channel is a 3-valve peristaltic pump modeled after designs reported by the Quake group.²² Individual pumping units consist of 3 Quake-style valves in series along a fluidic channel. Flow is generated by actuating each of the valves 120° out of phase with each other generating net fluid movement in one direction. A single-channel pump can generate flow rates up to 3 nL/s, but the flow is pulsatile. By integrating 3 pumping channels actuated 120° out of phase with each other, our device can generate smooth flow at rates up to 9.2 nL/s. The rate at which the cells flow into the injection intersection may be controlled by adjusting the actuation pressure of the valves

using a regulator. Details regarding the assembly and working principles of the on-board peristaltic pumps and the peripheral pneumatics were described in depth previously.¹

Additionally, the integration of the optical fiber enables fluorescence detection at two locations simultaneously without the addition of a second objective, detector, or additional optics. Placing the second detection spot prior to the injection intersection results in a signal just before cell lysis. By measuring the time between the intact cell signal and lysate signal the absolute migration time of separated species may be determined. This capability is important when multiple analyte signals must be identified and quantified.

2.2.5 Device fabrication

The microfluidic SCA device consisted of 2 layers, a fluidic layer and a pumping layer, and was fabricated using standard photolithography to make silicon wafer master molds (SWMs) for subsequent multilayer soft lithography using techniques reported previously and detailed below.¹

Photolithography

The photomasks used to generate the desired channel patterns were first drawn using AutoCAD 2018 (Autodesk, San Rafael, CA). The drawings were then sent to a laser photoplotting company (Fineline Imaging, Colorado Springs, CO) to be printed at a resolution of 40 kdpi. The fluidic layer pattern was printed with dark features and a clear background and the pumping layer pattern was printed clear with a dark background.

The fluidic layer SWM was fabricated by spin coating (Laurell Technologies, North Wales, PA) positive tone photoresist AZ P4620 onto a clean, chrome coated, silicon wafer (1000

rpm for 18 s) yielding a film thickness of 18-20 μm . The coated wafer was then soft baked on a hot plate using a multistep baking process beginning with 65 $^{\circ}\text{C}$ for 2 min, followed by a quick ramp in temperature to 95 $^{\circ}\text{C}$ (approx. 30 $^{\circ}\text{C}/\text{min}$) and held there for 2 min, and then a final quick ramp to 120 $^{\circ}\text{C}$ (approx. 30 $^{\circ}\text{C}/\text{min}$) and held for 4 min. The baked wafer was then removed from the hotplate and placed in a laminar flow hood to cool for 20 min. The photomask with the fluidic layer features was then placed carefully onto the coated wafer and a quartz block (4"x4"x0.5") was placed on top. The assembled wafer, photomask and quartz block were then placed in a UV flood exposure system (ThermoOriel, Stratford, CT) and exposed to UV light for the proper duration that is calculated using the prescribed UV energy dose for 20 μm film thickness (630 mJ/cm^2) and the measured output power of the mercury arc lamp. Following exposure, the quartz block and photomask were removed from the wafer and the wafer sat in the laminar flow hood for 10 min. The wafer was then placed into a crystallization dish filled with the AZ developer (1:4) and developed by gently swirling the developer to remove any uncured AZ. Following development, the wafer was then rinsed carefully with ultrapure water and then carefully dried using a nitrogen blowgun (< 50 kPa pressure). The wafer was then placed back onto a hotplate and baked at 120 $^{\circ}\text{C}$ for 4 min and then removed from the hotplate and allowed to cool for storage until use.

The pumping layer SWM for the upper layer of the device was fabricated using negative tone photoresist, SU-8 2010. The photoresist was spin coated onto a bare silicon wafer (1000 rpm for 20 s) yielding a film thickness of 20 μm . The coated wafer then underwent soft baking on the first hot plate at 65 $^{\circ}\text{C}$ for 2 min and then the second at 95 $^{\circ}\text{C}$ for 4 min. The coated wafer was then removed from the hotplate and allowed to cool for 10 min in a laminar flow hood. The photomask containing the valve manifold pattern for the upper layer was placed on top of the

coated wafer followed by the quartz block and subsequently exposed for a duration calculated using the required dose for the film thickness (145 mJ/cm^2) and the measured output power of the mercury arc lamp. The photomask and quartz were then removed, and the wafer was then immediately hard baked (using same temperatures and times as soft baking step) and allowed to cool. Then the wafer was placed into a crystallization dish containing SU-8 developer (2-(1-methoxy) propyl acetate) and developed by gently swirling the developer to remove any uncured polymer. Complete development was verified by removing the wafer from the developer and carefully squirting a small amount of isopropanol onto the pattern. Development was complete when no white streaks appeared upon contact with isopropanol. The wafer was then carefully dried using the nitrogen blowgun as described before.

Multilayer soft lithography

3 aliquots of PDMS with varying ratios of elastomer base to curing agent (approximately 30:1, 5:1, 10:1) were individually measured out, thoroughly mixed, and degassed in a vacuum desiccator. Both the fluidic and pumping SWMs were pretreated with a releasing agent (1:1 (v/v) HMDS:Xylenes). The fluidic layer was made by spin coating a $50 \mu\text{m}$ thick layer of PDMS onto the fluidic SWM. The pumping layer was made by pouring PDMS into a 5 mm thick plexiglass frame aligned on top of the fluidic SWM. Both layers were placed into an oven at $80 \text{ }^\circ\text{C}$ to cure for 90 min. Once cured, the layers were removed and allowed to cool. The pumping layer was then peeled off the pumping SWM and holes for compressed air inlets and the optical fiber were punched using a custom plexiglass jig as a guide. The pumping layer was placed on top of the fluidic layer by aligning the optical fibre holes with the fluidic channels for the cell detection point (CDP) and the lysate detection point (LDP) as shown in **Figure 2.1**. The assembled layers

were placed back into the 80 °C oven for an additional 90 min. Once fully cured and cooled, the chip was then peeled off the fluidic SWM, and 3 mm diameter reservoir holes were punched out using a disposable biopsy punch.

2.2.6 Device setup and operation

Setup of the microfluidic device

The underside of the microfluidic device (where the fluidic channels are located) was gently but thoroughly rinsed with ultrapure water for 20-30 s. The device was then dried using a nitrogen blowgun ($P < 50$ kPa) and placed channel side up into a laminar flow hood. Any remaining debris was removed by carefully allowing a length of Scotch Magic Tape to adhere to the channel side of the device and then it was carefully peeled away. Both sides of a microscope slide (75x50x1.0 mm) (Fisher Scientific, Pittsburg, PA) were cleaned using glassware soap and thoroughly scrubbed with a cleanroom swab (TX714MD, Texwipe, Kernersville, NC). The slide was then thoroughly rinsed for 20-30 s with ultrapure water and dried using a nitrogen blowgun. In the laminar flow hood, the microfluidic device was assembled by carefully layering the device atop the cleaned glass slide and air bubbles were avoided by slowly laying the device down left to right allowing the device to conform to the glass surface creating a reversible seal. Any dust or debris on the top of the device was then removed using Scotch Magic Tape to ensure minimal light scattering.

The device was then placed into the 3D printed chip holder and secured into the 3D printed microscope stage plate and placed in the xy translation stage of the microscope. The channels were allowed to fill passively by filling the GND reservoir with 30 μ L of prewarmed electrophoresis buffer (37 °C). The composition of the electrophoresis buffer was similar to that

reported previously.¹ The buffer consisted of 0.2% Tween20, 20% (v/v) Acetonitrile, 20 mg/mL BSA, 2 mM SDS and 25 mM sodium borate. Once all fluidic channels were filled with electrophoresis buffer, all reservoirs were filled with 30 μ L of electrophoresis buffer.

Once the device was filled, the high voltage (HV) wires (39x2215,22 AWG, Allied Electronics inc., Fort Worth, TX) with a short length of platinum wire (approx. 2 cm) soldered to one end were press fit into the wire slots on the chip holder with the platinum wire in the GND and +V reservoirs. The HV wire in the GND reservoir was connected to ground and the +V reservoir was connected to the output of the HV power supply (Spellman CZE1000R, Spellman High Voltage Electronics, Hauppauge, NY).

The on-board peristaltic pumps were actuated using 4 mounted solenoid valves (LHDA1221111H, The Lee Company, Westbrook, CT) mounted on a manifold (LFMX0510538BE, The Lee Company, Westbrook, CT) connected to a compressed air regulator (Norgren inc., Littleton, CO) which was connected to the building compressed air (120 psi) and regulated to deliver pressures between 0 and 2 bar. The actuation pattern of the solenoid valves was controlled by a microcontroller (pro trinket 5V, Adafruit, New York City, NY) programmed with in-house written code. The control program may be found in **Appendix C**. The voltage of the digital control signals from the microcontroller (5 V) was stepped up to the actuation voltage of the solenoids (12 V) using the L298N H-bridge (Elegoo inc., Shenzhen, China). The compressed air outlets of the manifold were then connected to the appropriate inlets on the device, labeled 1-4 in **Figure 2.1**.

Setup of the optical fiber and LIF detection

As an improvement on the previously published optical fiber detection system,³ the tapered plastic nozzles for fiber-chip coupling were replaced with straight metal tubes fashioned from the barrels of hypodermic needles. These metal fiber couplers (MFCs) were fabricated by cutting off the bevel and hub of 23-gauge hypodermic needles using a rotary tool equipped with a heavy-duty cut-off wheel (Dremel, Mount Prospect, IL). The MFCs not only have a smaller footprint compared to the plastic nozzles but also firmly hold the optical fiber perpendicular to the microfluidic device and in line with the LIF optics.

The MFCs were prepared by applying a small amount of refractive index matching gel (RI gel) to one end and inserting that end into their respective fiber optic access holes. Both ends of the MMF (105/125 μm core/cladding, Thorlabs FG105UCA, N.A. = 0.22) were then prepared by stripping the coating material near the ends and cleaning the fiber surfaces with an optical wiping tissue wet with isopropanol. The fiber ends were then cleaved using a mechanical fiber cleaver (FC-6S, Sumitomo Electric Lightwave Corp., Raleigh, NC) and inserted into the prepared MFCs. The fiber was bridged between the CDP in the cell handling channel and the

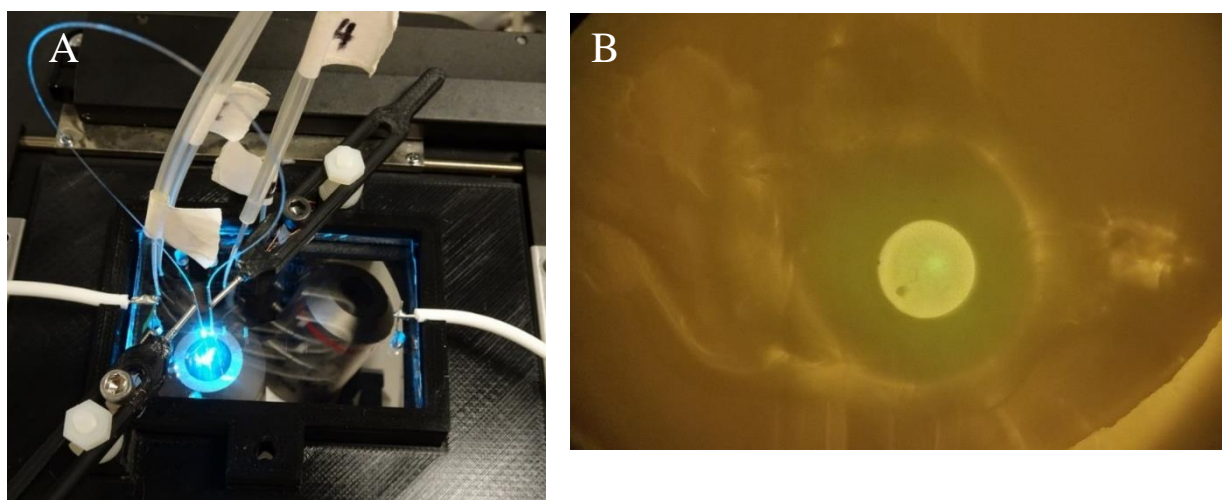


Figure 2.4 (A) Photograph of the fully assembled microfluidic SCA device with custom 3D printed stage plate and optical fiber manipulators. (B) Photograph showing the fiber-membrane interface with RI gel (20x).

LDP in the separation channel. Photographs showing the fully assembled system and the fiber-membrane interface with RI gel is shown in **Figure 2.4**.

The excitation source was a 488 nm laser diode (Oxxius- LBX-488-100-CSB-PP). As illustrated in our previous publication,⁴⁹ several optical elements (i.e. elliptical mirrors and an iris diaphragm) were used to direct the beam into the rear port of a commercial inverted Nikon TS-100-F microscope (Nikon Instruments, Inc., Melville, NY) equipped with a fluorescence filter

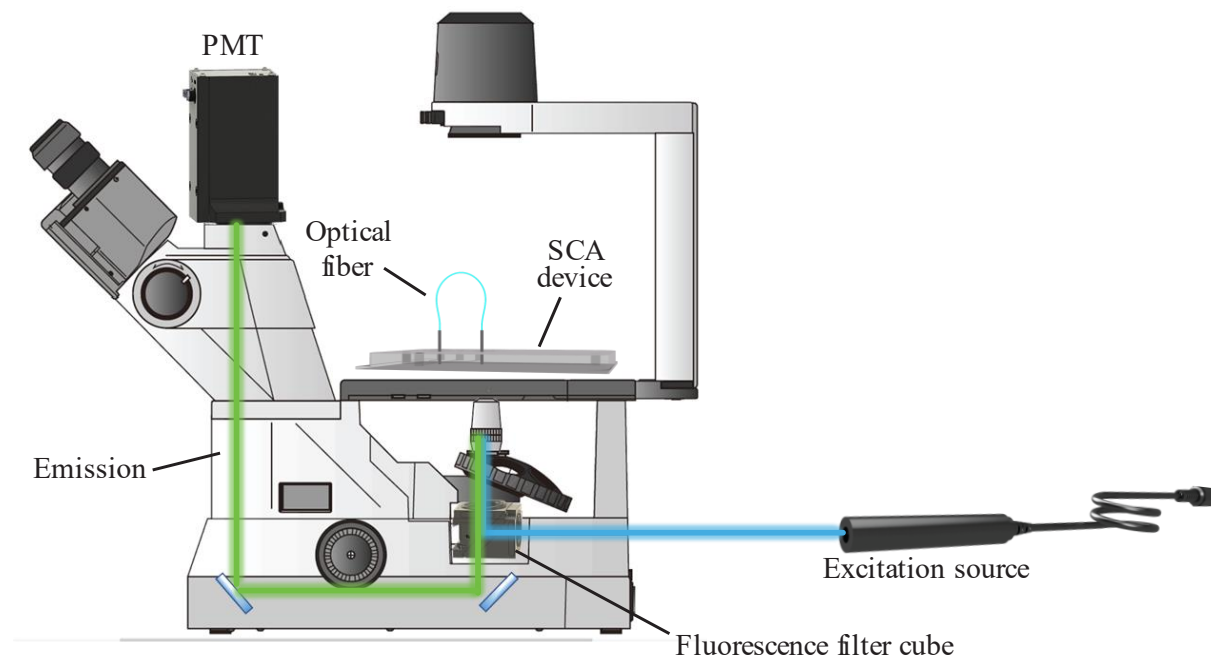


Figure 2.5 A diagram of the fluorescence detection optics setup. Excitation light from a solid-state diode laser is directed toward the objective through a fluorescence filter cube with a dichroic mirror. Fluorescence emission is collected through the objective and is directed toward the photomultiplier tube.

cube (XF115-2 FITC, Omega Optical, Brattleboro, VT). A 20× microscope objective (NA = 0.45) and Z-axis control (i.e. focusing knob) were used to control the spot size of a laser beam. The fluorescence signal was detected by a PMT (R-928, Hamamatsu Instruments, Bridgewater, NJ) with an 800 μm diameter pinhole. A diagram showing the fluorescence detection setup and optics is shown in **Figure 2.5**.

Data collection and analysis

The signal current from the PMT was amplified (1 or 5 $\mu\text{A/V}$) and filtered (30 Hz, low-pass) using a low-noise current preamplifier (Stanford Research Systems, Sunnyvale, CA). Data was collected using a differential analog input of a USB data acquisition device (USB-6002) and a program written in-house using LabVIEW (National Instruments, Austin, TX). Data visualization and analysis was performed using IgorPro (WaveMetrics, Portland, OR).

2.2.7 Single-cell analysis experiments

For experiments, 30 μL of labeled cell suspension was loaded into the sample reservoir, while the remaining cell suspension remained on the heat block (Fisher Scientific, Pittsburg PA) at 37 °C until more cell suspension was needed. Operation of the device began by turning on the on-board peristaltic pumps and setting the actuation pressure to result in a modest flow rate (< 1 bar). Verification of cell movement and sufficient fluorescence labeling was done through visual inspection. The electric field was then applied to the separation channel (850 V/cm). Adjustments to the actuation pressure were made by observing cell lysis at the intersection and determining whether the cells are moving too fast (i.e. a large portion of intracellular fluorescence continues on to the waste channel) or too slow (i.e. the entirety of the cell contents along with the membrane are injected down the separation channel). Typical flow rates for efficient lysis in our system fall in the range of 2-4 nL/s. The optimal electric field magnitude and flow rate must be found experimentally and varies between different cell lines and buffer composition and conductivity. It is crucial that the electric field be of sufficient strength to generate cellular lysis. In general, the lower limit of field strength is determined by the resulting

flow rate of the lowest actuation pressure at which reasonable cellular movement occurs. The upper limit is determined by the device's capability to dissipate power (between 5 and 10 W/m generally).⁵

Once the conditions for lysis were optimized, the objective was then directed toward the downstream end of the optical fiber at the LDP and the optical path was switched from the eyepiece to the PMT. Successful alignment of the fiber and optimal lysis will result in an electropherogram resembling that shown in **Figure 2.3**.

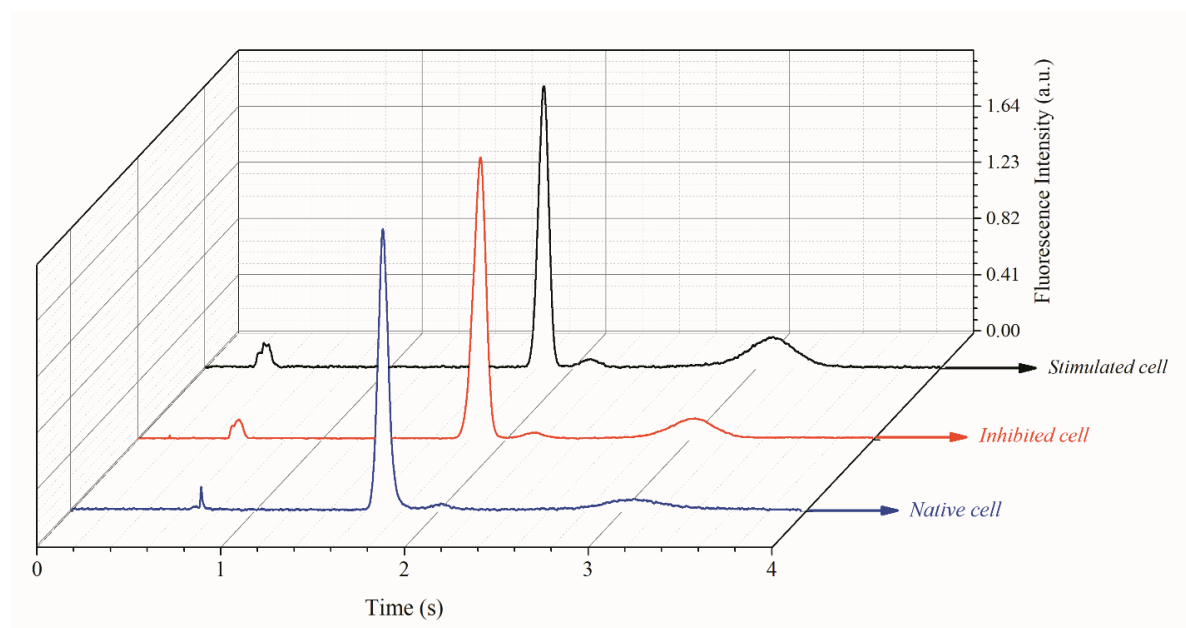


Figure 2.6 Representative electropherograms from the native, inhibited and stimulated experiments.

Changes in intracellular NO levels were quantified for native, stimulated, and inhibited cells. These changes were measured by computing the ratio of the fluorescence peak areas of DAF-FM T to those of 6-CF for each cell. An overlay of representative single-cell electropherograms from each of the 3 runs is shown in **Figure 2.6**. A summary of the results from the experiments is shown in **Table 2.1**.

Table 2.1 The average ratios (DAF-FM T/6-CF \pm standard deviation) of the peak area and peak height for native, stimulated and inhibited cells.

peak area ratio	DAF FM T/6-CF	no. of cells
native cells	0.31 \pm 0.15	53
stimulated cells	0.68 \pm 0.29	44
inhibited	0.37 \pm 0.17	66
peak height ratio	DAF FM T/6-CF	no. of cells
native cells	0.067 \pm 0.031	53
stimulated cells	0.18 \pm 0.08	44
inhibited	0.11 \pm 0.05	66

2.2.8 Characterization of optical fiber signal improvement

For the signal improvement experiments, we applied small amounts of a RI gel to both ends of the optical fibre bridge before inserting them into the microfluidic device. To compare the transmission efficiency of the optical fiber with and without the RI gel, we loaded a sample of fluorescent 10 μ m diameter polystyrene microspheres into the sample reservoir and pulled them past the CDP using the on-board pumps and measured the emission at the LDP. Plots showing a series fluorescence peaks both with and without RI gel is shown in **Figure 2.7**. The average fluorescence signals for both conditions are shown in **Table 2.2**.

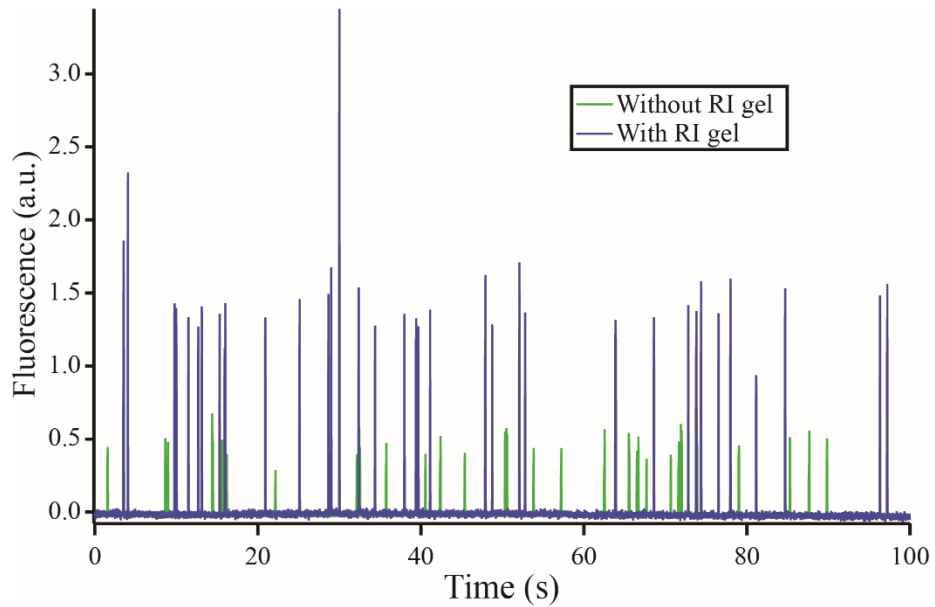


Figure 2.7 Fluorescence signal from 10 μm fluorescent polystyrene microspheres with RI gel (blue) and without (green).

Table 2.2 Average intensity and 95% confidence interval of fluorescence signals from 10 μm fluorescent microspheres with and without the application of RI gel to the optical fiber faces.

	n	Average Intensity (a.u.)
Without gel	80	0.48 ± 0.03
With gel	80	1.43 ± 0.09

2.3 Discussion and results

2.3.1 Measurement of changes in NO production

Difficulties in detecting sufficient intact cell and DAF-FM T arose in early experiments. Each of these issues were caused by two separated and independent phenomena. Issues with detecting the intact cell signal seemed to have been due to issues in the detection optics. One possible explanation is that the face of the optical fiber is further away from the objective than the fluidic channel, and therefore, may be slightly out of focus when the fluidic channel is in focus. Therefore, the position of the objective had to be adjusted until intact cell signal was observed when the optical path was switched from the eyepieces to the PMT. The difficulty in detecting DAF-FM T signal in the cell lysate was not due to issues with the detection optics. During initial experiments, the flow rate was adjusted until cells were observed flowing through the device and appeared to be completely lysed. However, when collecting the electropherograms, only a peak for 6-CF was observed in the lysate for each cell. We determined that this was likely due to hydrodynamic flow pulling the less mobile DAF-FM T toward the pumps while allowing the more highly mobile 6-CF to travel down the separation channel. This was confirmed when the actuation pressure of the pumps was reduced, and the DAF-FM T peak signal began to appear.

Changes in NO production in single Jurkat cells in the presence and absence of LPS stimulation have been reported previously by our group.²⁹ In that study, changes in NO production were measured by calculating changes in the ratio of peak areas and peak heights of DAF-FM T and 6-CF. It was concluded that the change in peak area ratio and peak height ratio indicated a 2-fold increase in NO production in stimulated cells. Both the increase in peak area ratio and peak height ratio were found to be statistically significant. Given that both the peak

area ratio and peak height ratios were in agreement in the previous study, we believe that it is appropriate to consider peak area ratios alone. Peak areas are considered to be more reliable in quantitation because the values do not change significantly if peak shapes are not Gaussian. This will minimize error in quantitation due to potential differences in band broadening between the separated species. **Table 2.3** shows the calculated percent differences between each of the experimental conditions and the statistical significance (p-value) of each difference.

Table 2.3 Percent difference and associated p-values for the peak area ratios for each experimental condition.

	% difference	p-value
Native → Stimulated	+135%	$< 2 \times 10^{-15}$
Stimulated → Inhibited	-49%	$< 2 \times 10^{-12}$
Native → Inhibited	+21%	< 0.04

In the previous study, an increase in peak area ratio of 85% was observed between the native and LPS stimulated conditions. The larger increase in NO production observed in this work can most likely be attributed to the higher concentration of LPS used in stimulation experiments. Unfortunately, the previous study did not verify whether the analysis performed was capable of measuring a decrease in NO production through the addition of a selective iNOS inhibitor. To demonstrate this capability, we chose to treat cells simultaneously with LPS and a known potent and selective inhibitor of iNOS (1400W dihydrochloride). A decrease in NO production of 49% was observed between the stimulated cells and the inhibited cells. This demonstrates the potential for the SCA device to be used in pharmaceutical development applications for testing and characterizing the efficacy of new potential anti-inflammatory therapeutics. NO production in inhibited cells was observed to be slightly higher (+21%) than native cells, however it should

be noted that the statistical significance of this increase is much lower than the other measured differences. It is also important to mention that better quantitation of NO in this study was achieved due to the absence of an extra internal standard peak that was present in our previous publication.²⁹ In the previous report it was suggested that the extra peak observed was due to the presence of partially hydrolyzed 6-CFDA. However, experiments to confirm this were not performed, and therefore, the possibility of contamination cannot be ruled out. While the extra peak did not seem to have significantly influenced quantitation, its absence in these experiments is worth noting. In future studies, we hope to add additional fluorescent probes to measure other inflammatory markers and having an extra contaminant peak could potentially increase the chances of fluorescent peak overlap, and therefore, make quantitation difficult.

2.3.2 Optical fiber signal improvement

One limitation to the optical fiber bridge that was discussed in its initial reporting was the loss of signal due to fiber coupling inefficiency.³ There are several possible causes of light loss in the optical fiber setup, including attenuation loss due to the bending of the fiber, scattering from imperfections in the PDMS membrane, or surface reflection at the fiber-PDMS junctions. Attenuation from fiber bending can be minimized by cutting the MMF longer, thereby maximizing the radius of curvature. Both the scattering at the PDMS membrane and surface reflection at the fiber-PDMS junction can potentially be solved simultaneously. Signal loss from reflection can be attributed to Fresnel reflection at the fiber-membrane interface due to the presence of small air gaps between the optical fiber face and the PDMS membrane. Similarly, surface imperfections in the PDMS membrane can be described as small air gaps in scratches and grooves in the soft PDMS. The scattering and reflection are caused by the step change in

refractive index between the PDMS membrane, air, and the fiber face. In the telecommunications industry a refractive index matching liquid or gel is commonly used for fiber couplings to mitigate similar issues that occur at fiber junctions. With the applied RI gel, we observed a 200% improvement in signal. Previously, to reliably detect the intact cell signal we had to compensate for the limitations in the sensitivity of the optical fiber bridge by increasing the concentration of the internal standard in the loading solutions. For accurate quantitation, the signal intensity of the internal standard peak must fall within the linear range of the current pre-amplifier output. By improving the sensitivity of the optical fiber bridge, we hope to minimize the concentration of internal standard necessary for intact cell signal detection, and therefore, be able to detect lower concentration analytes by increasing the signal amplification setting on the current pre-amplifier.

2.4 Concluding remarks

Herein we have fully described the design, fabrication, and operation of our μ CE-LIF system for the analysis of single cells. As a demonstration of the utility of our system, we applied it to the analysis of intracellular NO in T-lymphocytes under native, LPS stimulated, and inhibited conditions. As expected, we observed a marked increase in NO levels upon stimulation with LPS in comparison with the native cells and a decrease in NO with the addition of the iNOS inhibitor 1400W dihydrochloride. It is important to note that this is the first time we are reporting the use of our device to measure the effects on an inhibitor on the production of intracellular NO. This demonstrates the potential applicability of our system for the study of the effects of novel pharmaceutical agents for the treatment of diseases associated with inflammation, such as Alzheimer's, Parkinson's, cardiovascular disease, and cancers²⁷.

The system presented in this chapter is the result of many years of work done by several researchers. We believe that we have reached the point where our system is robust enough to be used for the analysis of a variety of enzyme activities at the single cell level. It is our hope that the information in this chapter may help other research groups to directly use, or adapt for their purposes, our single-cell analysis device.

Chapter 3 - Single-cell analysis of nitric oxide in SIM-A9 microglial cells

3.1 Introduction

Current treatment strategies are largely ineffective for neurodegenerative diseases like Alzheimer's disease (AD), Parkinson's disease (PD), and chronic traumatic encephalopathy (CTE).⁵⁰⁻⁵² These diseases are characterized by accumulations of misfolded proteins in the brain which trigger a prolonged inflammatory response ultimately leading to neuronal death and a decline in cognitive or motor functions.⁵³ Microglia, being the resident immune cells in the brain, are responsible for the sustained inflammatory environment. Several reviews have cited studies that implicate microglia as playing a central role in the progression of these diseases and other brain pathologies.⁵³⁻⁵⁷

Microglial phenotypes can be described as resting/surveilling (M0), “classically” activated/pro-inflammatory (M1), or “alternatively” activated/anti-inflammatory (M2).⁵⁸ Under normal conditions, the microglial response to neurological insults in the central nervous system consists of a balance between the M1 and M2 phenotypes. A growing body of evidence suggests that microglia in aged brains become “hypersensitive” leading to exaggerated inflammation in response to the protein aggregates present in AD, PD, CTE and other pathologies.⁵⁹ Researchers have found that under these chronic inflammatory conditions, M1 activated microglia become neurotoxic causing accelerated neuronal death.⁶⁰ Upon M1 activation, microglia undergo changes in morphology and motility as they secrete pro-inflammatory cytokines like tumor necrosis factor alpha (TNF- α) and interleukin one beta (IL-1 β), and other signaling molecules.^{56,}

⁶⁰ One class of inflammatory signaling molecules produced by activated microglia are reactive

nitrogen and oxygen species (RNOS). Among the RNOS produced, nitric oxide (NO) has received a lot of attention not only due to its involvement in several physiological processes but also because of its potentially harmful reactivity.⁶¹ NO exists as a dissolved gas *in vivo* produced by a family of enzymes called nitric oxide synthases (NOSs). Inducible NOS (iNOS) is the isoform of NOS that is associated with the inflammatory phenotype of microglia. Excessive levels of NO can lead to nitrosative stress which can result in the induction of neuronal apoptosis thus accelerating the progression of neurodegeneration.⁶² For this reason iNOS has become a potential therapeutic target for the treatment of neurodegenerative diseases.⁶³ Measuring NO production in microglial cells can help in evaluating the efficacy of novel therapies and may also serve as a means of studying the dynamics of microglial inflammation. However, it is difficult to obtain an accurate picture of NO levels in microglial cell populations not only due to its short half-life but also because most methods measure extracellular NO levels and are unable to account for cell-to-cell variations.⁶⁴⁻⁶⁵

As discussed in the previous chapter, we developed a microfluidic single cell analysis (SCA) device and applied it to the measurement of NO production in an immortalized T lymphocyte cell line (Jurkat).^{4, 29} Thus far, the SCA device has only been used for the analysis of Jurkat cells which are cultured in suspension, whereas the majority of vertebrate-derived cells are adherent. Furthermore, Jurkat cells are not an appropriate model cell line for the study of neurodegenerative diseases. Therefore, it was important that we demonstrate the application of this device to the measurement of a pathologically relevant biomolecule within a cell-type derived from the organ of interest. In this chapter, we report the application of our SCA device for the analysis of NO in single microglial cells. As an *in vitro* cell line model, we chose the recently discovered spontaneously immortalized line of mouse microglial cells, SIM-A9.⁶⁶ SIM-

A9 cells are potentially of greater biological relevance as compared to other immortal cell lines available. Cell lines can become immortalized as a result of cancer-related mutations, retroviral genetic modification, or a spontaneous mutation occurring naturally. In the case of SIM-A9 cells, their immortalized characteristics originates from a spontaneous mutation. Therefore, it is reasonable to assume that their behavior more closely resembles their primary counterparts, apart from the mutation that imparted immortalization, compared to cells immortalized by other means. The researchers that discovered this cell line confirmed this by comparing SIM-A9 cells, primary microglia, and another immortal line of microglia (BV-2) in terms of inflammatory response and phagocytic capacity. They concluded that SIM-A9 cells resemble primary microglia as well as, if not better than the BV-2 cells. Additionally, SIM-A9 cells are relatively low-cost and readily available making them an ideal alternative to primary cells for in vitro studies of microglia. In this chapter we report the measurement of intracellular NO in single SIM-A9 microglia under native conditions, and co-stimulation with lipopolysaccharides (LPS) and interferon gamma (IFN- γ) with and without a potent iNOS inhibitor (1400W dihydrochloride). Statistical analysis was performed on the fluorescence data for each cell population to characterize the shape of the population distribution, which highlights the usefulness of acquiring measurements with single-cell resolution.

3.2 Materials and methods

3.2.1 Reagents and materials

SIM-A9 microglial cells (mouse, ATCC CRL-3265) and Dulbecco's phosphate buffered saline (D-PBS, 1x ATCC 30-220) were purchased from American Type Culture Collection (Manassas, VA, USA). Dulbecco's Modified Eagle Medium/Nutrient Mixture F-12 (DMEM:F-

12) was purchased from Thermo Fisher Scientific (Waltham, MA, USA). 4-Amino-5-methylamino-2',7'-difluorofluorescein diacetate (DAF-FM DA) was also purchased from Thermo Fisher Scientific in 50 µg packs. Sodium borate, lyophilized bovine serum albumin (BSA), Tween-20, xylenes (Certified ACS), acetonitrile (HPLC grade), and premium fetal bovine serum (USA origin, heat inactivated) were all obtained from Fisher Scientific (Pittsburgh, PA, USA). Sodium dodecyl sulfate, anhydrous dimethyl sulfoxide, 99.9% (DMSO), horse serum (USA origin, heat inactivated), and lipopolysaccharides (LPS) from *Escherichia coli* line 0111:B4 were purchased from Sigma-Aldrich (St. Louis, MO, USA). Lyophilized interferon gamma (IFN- γ) (Mouse) was purchased from GenScript (Piscataway, NJ, USA). 6-Carboxyfluorescein diacetate, single isomer (6-CFDA) and probenecid sodium salt were purchased from Biotium Inc. (Fremont, CA, USA). The iNOS inhibitor, 1400W dihydrochloride, was purchased from Tocris (Minneapolis, MN, USA). Negative tone photoresist SU-8 2010 was purchased from MicroChem Corp. (Newton, MA, USA). The SU-8 developer, 2-(1-methoxy) propyl acetate (99%), was obtained from Acros (Morris Plains, NJ, USA). AZ P4620 positive tone photoresist and AZ 400K developer (1:4) were obtained from AZ Electronic Materials (Branchburg, NJ, USA). Silicon wafers (100 mm diameter, single-side polished, mechanical grade or better) were purchased from Silicon, Inc. (Boise, ID, USA). Chrome coated (500 Å) silicon wafers (100 mm diameter, single-side polished, test grade) were purchased from WRS Materials (San Jose, CA, USA). (1,1,1,3,3,3-Hexamethyldisilazane (98%) (HMDS) was purchased from Gelest (Morrisville, PA, USA). Sylgard 184 PDMS prepolymer and curing agent were purchased from Dow Corning (Corning, NY, USA). Ultrapure water was generated from a Barnstead E-pure system (Dubuque, IA, USA). Multimode optical fiber (0.22 NA, core Ø105

μm) and refractive index matching gel (G608N3) were obtained from Thorlabs Inc. (Newton, NJ, USA).

3.2.2 Device fabrication and setup

The multi-layer microfluidic device was fabricated using photolithography and multi-layer soft lithography and setup in the same manner as described in Chapters 2 and 3.

3.2.3 Tissue culture

SIM-A9 cells were cultured lying flat in T75 polystyrene flasks (Fisher Scientific, Waltham, MA, USA) in a humidified environment at 37 °C and 5% CO₂ in Dulbecco's Modified Eagle Medium/Nutrient Mixture F-12 (DMEM:F-12) supplemented with heat inactivated fetal bovine serum (10% v/v), heat inactivated horse serum (5% v/v), and streptomycin (100 $\mu\text{g}/\text{mL}$). Once the cells reached 80% confluency, they were passaged. SIM-A9 cultures contain a mixture of adhered and suspended cells. Passaging begins by first scraping the attached cells using an in-house made glass scraper. Scraped cells and suspended cells were then mixed by pipetting and transferred to a 15 mL conical vial and centrifuged at 1000 rpm (or 125 x g) for 5 min. The supernatant was then discarded, and the cell pellet was resuspended in fresh media and split into flasks at a subcultivation ratio between 1:3 and 1:6 with a total culture volume of 15 mL.

3.2.4 Sample preparation

Intracellular NO levels were measured by co-labelling cells with DAF-FM DA and internal standard 6-CFDA following a similar procedure described previously in Chapter 3.⁴ Stock solutions of DAF-FM DA (approx. 1 mM) and 6-CFDA (3.74 mM) were prepared in anhydrous DMSO and were aliquoted and stored frozen at -20 °C until ready for use. Additionally, to minimize dye efflux by MRP1 a 250 mM stock solution of probenecid, an

MRP1 inhibitor,⁴⁸ was prepared in PBS. A labelling solution containing 6-CFDA (40 μ M), DAF-FM DA (150 μ M) and probenecid (2.5 mM) was prepared fresh for each experiment in PBS. The experimental procedure for treatment and preparation of cells is illustrated in **Figure 3.1**. Once the cells were ready for NO measurements, native, stimulated, and inhibited cells were all treated in the following manner. Cells were first scraped and mixed as described above. A sample of the cell suspension (1 mL) was then transferred into a 1.5 mL Eppendorf tube and centrifuged (1000 rpm for 5 min). The supernatant was then removed, and the pellet was resuspended in 100 μ L of the labelling solution and incubated for 30 min at 37 $^{\circ}$ C on a dry bath heating block. Following labelling, the cells were diluted to 1 mL with prewarmed PBS (37 $^{\circ}$ C) and centrifuged (1000 rpm, 5 min). The supernatant was then discarded, and the cells were resuspended again in 1 mL of prewarmed PBS. The cells were spun down and resuspended twice more, but the final resuspension solution was 1 mL of PBS containing 2 mg/mL BSA and 2.5 mM probenecid.

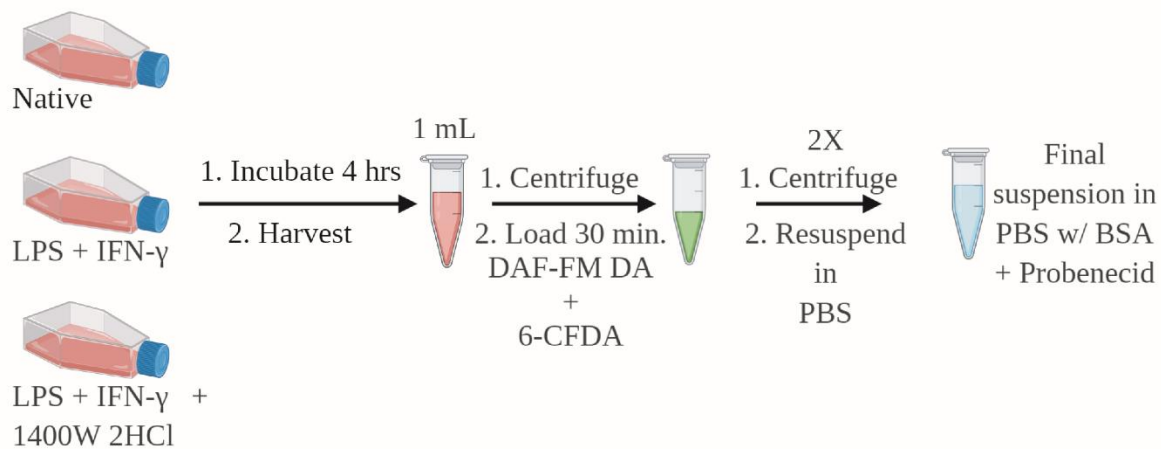


Figure 3.1 A scheme illustrating the procedure used to prepare cells for NO measurements. Created using Biorender.com.

3.3 Results and discussion

Over the years, our research group has published several reports on the continued development of this high-throughput microfluidic single cell analysis technology.^{1, 3-4, 29, 49} However, this is the first demonstration of our system being used for the analysis of an adherent cell type and examining the effects of the addition of stimulators in combination with inhibitors on the etiologically relevant response of cells that originate from the corresponding parenchyma.

3.3.1 Measurement of NO production

SIM-A9 cells are a recently isolated spontaneously immortalized cell line, and as such, there are relatively few studies available for comparing results. However, initial comparisons between SIM-A9 cells and their primary counterparts indicate that they behave similarly in response to inflammatory stimuli.⁶⁶

For stimulation experiments, cells were co-stimulated with LPS and IFN- γ for 4 hr to elicit an inflammatory response which is characterized, in part, by elevated levels of NO production. For inhibition experiments, cells were incubated with the same levels of LPS and IFN- γ for the same period of time but in the presence of the potent and selective iNOS inhibitor 1400W dihydrochloride. Cells for native, stimulated, and inhibited experiments were then all treated in the same manner prior to analysis, shown as a workflow in **Figure 3.1**. Cells were incubated in a loading solution containing the fluorogenic NO probe, DAF-FM DA, and an internal standard, 6-CFDA. 6-CFDA has been used as an internal standard for similar analyses previously.^{29, 67} Once inside the cell, both DAF-FM DA and 6-CFDA are hydrolyzed by non-specific esterases to form DAF-FM and 6-CF, respectively. This allows us to account for cell-to-cell variability in cell volume, esterase activity and viability.

The optical fiber detection was set up such that the CDP was just below the lysis intersection and LDP was 2 mm down the separation channel. The on-board pumps were then turned on to draw the cells to the lysis intersection. An electric field strength of 850 V/cm was applied across the separation channel providing a means of lysis and subsequent electrophoretic separation of the intracellular contents. The flow rate, driven by the pumps, was adjusted at the beginning of each experiment to achieve optimal cell lysis and injection efficiency. The conditions for maximum injection efficiency were determined by visually observing lysis and adjusting the flow rate up or down such that ~100% of the lysate travels down the separation channel and the cell debris travels toward the waste reservoirs.

As cells flow underneath the CDP, a short and narrow peak is observed followed shortly by a set of peaks corresponding to 6-CFDA, DAF-DHA and DAF-FM T as they pass the LDP. A representative excerpt showing a series of single cell electropherograms is shown in **Figure 3.2**.

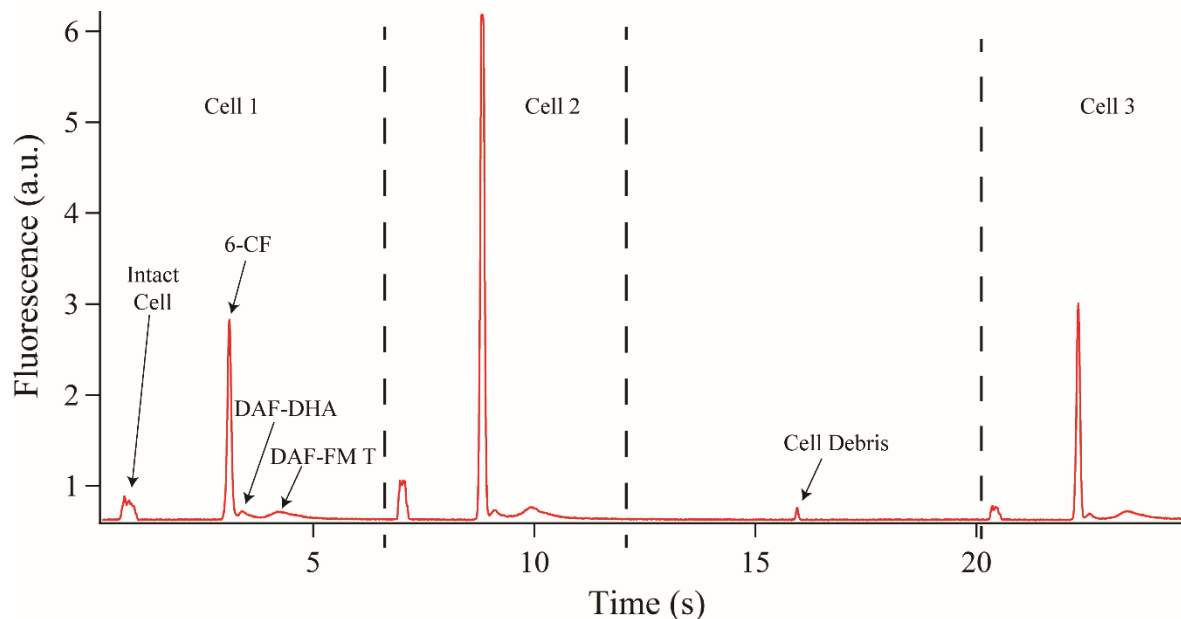


Figure 3.2 A representative excerpt of fluorescence data for single cell analysis of NO in SIM-A9 microglia. Each cell produced a total of 4 peaks: intact cell, 6-CF, DAF-DHA and DAF-FM T.

Intracellular NO production was calculated for each cell using the ratio of the peak area of DAF-FM T (A_{DAF}) to the peak area of the internal standard 6-CF (A_{CF}). The population distributions of NO production for each experiment were visualized using histograms shown in **Figure 3.3**. Upon inspection of the distributions, it was apparent that they did not fit a normal distribution. Non-normal distributions violate the assumptions that must be made when performing statistical tests such as a t-test for the comparison of means. It is possible to perform non-parametric statistical tests on non-normal data, however, statistical power and significance are reduced in this case. In order to perform parametric statistical tests, the distribution shape needs to be characterized. The shape of each distribution was characterized by computing the skewness and subsequently testing for normality using a Shapiro-Wilk test.⁶⁸ The skewness values for all three distributions were significantly positive indicating that the majority of cells fall in the lower end of the distribution with the presence of a tail toward higher values (shown in **Table 3.1**). Skewness is helpful in initial characterization of distribution shapes because it provides a quantitative metric for the degree and direction of the asymmetry in a distribution. By considering the skewness and doing a visual comparison we hypothesized that the distributions fit a log-normal shape. To determine whether the data fit another common distribution shape, a Shapiro-Wilk test was used. The Shapiro-Wilk test was chosen because it is parametric and because of its statistical power when compared to other tests for normality.⁶⁹ The Shapiro-Wilk test p-values confirmed that the distributions could not be described as normal ($\alpha = 0.05$). These results initially precluded the use of a one-tailed t-test for the comparison of means of independent samples because the assumption of normality was not met. However, given the

positive skewness and the absence of negative values, we theorized that the data may fit a lognormal distribution. To test the data for lognormality, a log transformation was performed on each dataset (using the natural logarithm), and the skewness and Shapiro-Wilk test were repeated. The skewness of the log transformed data was significantly reduced, and the Shapiro-

Table 3.1 Skewness and Shapiro-Wilk p-values for untransformed and log transformed datasets for native, stimulated, and inhibited conditions.

Wilk test confirmed that the log transformed data were normally distributed ($\alpha = 0.05$).

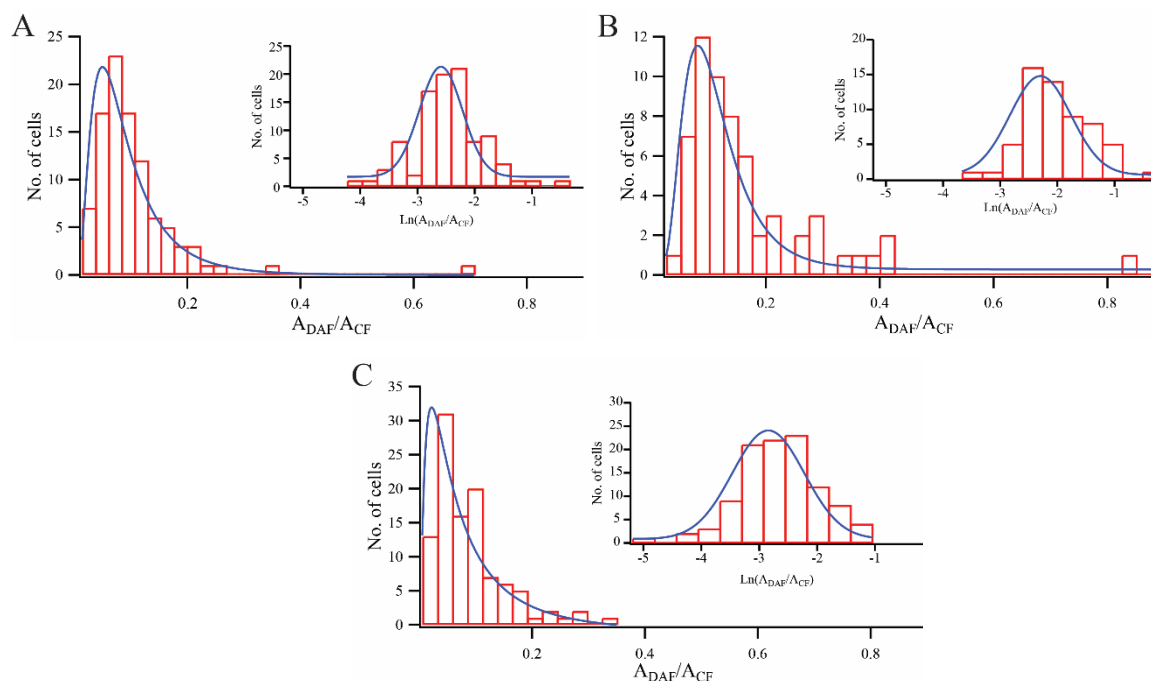


Figure 3.3 Histogram plots of the peak area ratios for native (A), stimulated (B), and inhibited (C) conditions. The insets in A-C are histogram plots for the log transformed datasets. The traces are lognormal fits for the main plots and gaussian for the inset plots.

^a Skewness values are calculated using Equation 3.1. ^b Shapiro-Wilk test statistics p-values are calculated using a plugin for Microsoft Excel.

$$\frac{n}{(n-1)(n-2)} \sum \left(\frac{x_i - \bar{x}}{s} \right)^3 \quad (3.1)$$

The mean values of the log transformed datasets could then be compared using a one-

	Untransformed		Transformed	
	Skewness ^a	Shapiro-Wilk p-value ^b	Skewness ^a	Shapiro-Wilk p-value ^b
Native	4.43	4.5x10 ⁻¹⁴	0.083	0.25
Stimulated	2.99	1.72x10 ⁻⁰⁹	0.41	0.28
Inhibited	1.63	1.12x10 ⁻⁰⁸	-0.31	0.39

tailed t-test for the comparison of means of independent samples. First, the standard deviations for the transformed native, stimulated and inhibited datasets were compared using an F test to determine which form of the t-test was appropriate. The calculated F statistics (F_{calc}) for each comparison concluded that the standard deviations were not significantly different ($\alpha = 0.05$).

The means of the transformed data sets were then compared, and the calculated t values indicated that the differences were statistically significant. The p-values for each comparison are listed in

Table 3.2.

Table 3.2 Calculated percent differences in the peak area ratios between each experimental condition. The p-values listed correspond to the one-tailed t0test for the comparison of means of independent samples performed on the log transformed datasets.

	% difference	p-value
Native → Stimulated	+135%	$< 2 \times 10^{-15}$
Stimulated → Inhibited	-49%	$< 2 \times 10^{-12}$
Native → Inhibited	+21%	< 0.04

While confidence intervals for normal distributions are symmetrical about the arithmetic mean, lognormal distributions are better represented using the geometric mean with an asymmetrical confidence interval based on the multiplicative standard deviation. The geometric mean (\bar{x}^*) and multiplicative standard deviation (s^*) are determined by “back-transforming” the mean (\bar{x}) and standard deviation (s) of the transformed data:²

$$\bar{x}^* := e^{\bar{x}}, s^* := e^s \quad (4.2)$$

Table 3.3 Arithmetic and geometric summary statistics for native, stimulated, and inhibited datasets; ^a The \bar{x}^*/s^a for geometric statistics is analogous to the \pm for arithmetic statistics. The lower and upper bounds of the 95% confidence interval are: $\bar{x}^* \div s^{*2}$ and $\bar{x}^* \times s^{*2}$.²

n	$\bar{x} \pm s$	\bar{x}^* / s^a	~95% C.I. ^a
---	-----------------	-------------------	------------------------

Native	97	0.10±0.08	0.085 ^x /1.83	0.025-0.28
Stimulated	60	0.16±0.13	0.133 ^x /1.86	0.038-0.46
Inhibited	105	0.088±0.063	0.070 ^x /2.02	0.017-0.28

Table 3.3 shows the summary statistics for the native, stimulated and inhibited experiments and includes both the arithmetic mean and standard deviation as well as the geometric mean and multiplicative standard deviation. An overlay of representative single cell electropherograms for the native, stimulated, and inhibited experiments is shown in **Figure 3.4**. The fluorescent peak heights were adjusted according to the internal standard, 6-CF, to allow for a direct comparison of cells. To compare the change in NO production across the cell populations, the percent difference between each experimental condition (shown in **Table 3.2**) was calculated using the geometric mean values (shown in Table 3.3). It is worth noting that despite the fact that the NO levels are not being measured in units of concentration, this method still produces a numerical measure that will enable researchers to quantitatively study the impact of various pharmacological agents on cellular populations.

When comparing the various conditions, we observed a 56% ($p < 0.00001$) increase in NO production between the native and stimulated experiments and a 47% ($p < 2 \times 10^{-8}$) decrease in NO production when cells were simultaneously treated with iNOS agonists (LPS and IFN- γ) and the iNOS inhibitor (1400W dihydrochloride). We also observed a modest decrease in NO production (approx. 18%, $p < 0.02$) in the inhibited cell population as compared to the native cell population. It is likely that during the course of the cell harvesting and loading processes an acute inflammatory response was elicited as a result of incidental cellular stress and damage. In future studies more gentle handling and loading techniques will be investigated to minimize their impact on measurements of inflammatory markers. It is also possible that the iNOS enzyme could produce more NO to compensate for the NO that was consumed by the reaction with DAF-FM. This would result in a gradual increase in DAF-FM T signal over the course of an experiment. Fortunately, we did not observe this phenomenon under any of the experimental conditions.

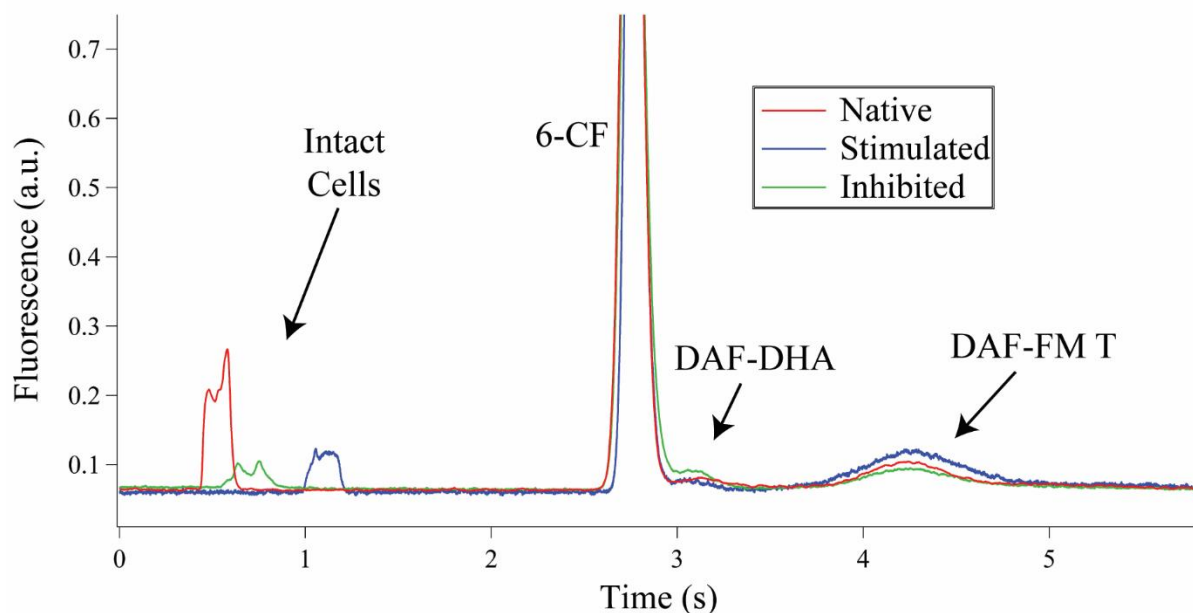


Figure 3.4 An overlay of single-cell electropherograms for native, stimulated, and inhibited cells. Fluorescence intensities have been scaled according to the internal standard peak signal.

One potential downside to measuring NO using diaminofluorescein species, discussed in our previous publication,²⁹ is the formation of fluorescent derivatives when reacted with dehydroascorbate (DHA), the oxidized form of ascorbic acid (AA). AA interference is of particular concern when measuring NO production in microglia because AA concentrations in the brain parenchyma (2-10 mM) are among the highest in the body.⁷⁰ Comparing our electropherograms to those reported previously, we believe that the second peak is a DAF-DHA derivative (**Figure 3.2** and **Figure 3.4**).⁶⁷ Some studies have suggested that AA levels may play a role in chronic neuroinflammation associated with neurodegenerative pathologies.⁷¹⁻⁷² In future experiments, we may exploit the formation of DAF-DHA derivatives as a means to measure intracellular AA levels and its impact on inflammation.

3.3.2 Single vs bulk cell analysis

Without the benefit of a large number of studies, it is difficult to compare our results to any published reports. Additionally, all NO analyses reported for SIM-A9 microglia thus far were bulk cell measurements of extracellular NO levels using the Griess reaction.⁶⁶ Using DAF-FM DA instead of the Griess reaction not only provides greater sensitivity, but allows for the quantitation of intracellular NO production at the single cell level which can yield more detailed information about how a population of cells respond to pro-inflammatory stimuli. In bulk-cell studies, the population average values measured are not capable of determining the shape of the distribution of cellular response. Recent studies show that measuring cellular response at the single-cell level can help to better characterize the regulatory roles that signalling enzymes and molecules play.⁷³⁻⁷⁴ Mapping the different regulatory roles of signalling components in a cascade may help to better understand how normal cellular function is disrupted, especially in neurodegenerative pathologies. With this information, novel treatment strategies may be

developed to combat the disruptions more specifically. Furthermore, the efficacy of the new treatment strategies can be evaluated using the same single-cell analysis technologies used to study the signalling cascades.²⁴

3.4 Conclusion

Measuring intracellular NO in single microglia will enable researchers to study not only the average effect of a potential pharmaceutical on a cell population but increases the depth of information collected. Here we used our microfluidic device to measure changes in NO levels in SIM-A9 microglial cells under native, stimulated, and inhibited conditions using a fluorogenic probe and an internal standard. Following a 4-hr stimulation with LPS and IFN- γ , a 56% increase in NO production was observed as compared to native cells. The effects of a selective iNOS inhibitor, 1400W dihydrochloride, were measured by treating cells with both the inflammatory stimulants and the inhibitor. Not only were NO levels lower than stimulated conditions by approximately 47%, but inhibited cells produced 18% less NO compared to native cells. In addition to quantitation, the electrophoretic separation allowed us to distinguish between fluorescence from DAF-FM T and the interfering DHA derivatives. We also observed that the population distributions for all three experimental conditions exhibited lognormal characteristics. Further characterization of cell-to-cell variability in the expression and production of inflammatory markers may help to better understand the impact aging has on the immune system. It is worth noting that this is the first report of single cell analysis being performed on SIM-A9 microglial cells. This report marks the first instance of our device's application for the analysis of an adherent cell line since the beginning of its development in 2003.⁷⁵ In future studies, we would like to investigate the relationship between distribution shape and enzymatic

regulation or dysregulation. Arginine is the sole substrate for iNOS, therefore, arginase is a direct antagonist for iNOS because it reduces the amount of arginine available for NO production. Studies have shown that exposure of microglia to oligomeric amyloid beta ($A\beta$), a protein that is known to aggregate and form plaques in AD brains, results in an improperly regulated inflammatory response.⁷⁶ One study also observed a decrease in Arg1 (the gene that encodes the protein arginase) expression in primary microglia upon exposure to $A\beta$.⁷⁷ Furthermore, exposed microglia exhibited decreased phagocytic function which is necessary for the clearance of $A\beta$ plaques in AD brains. In future studies, we may investigate whether there is a characteristic shift in population distribution shape by inhibiting or stimulating arginase in the presence of LPS and IFN- γ . Additionally, We hope to further expand the application of our device to the analysis of other cell types relevant to other brain diseases, such as U-87 glioblastoma cells. Future work will be directed toward studying how glioblastoma cells modulate nearby immune cells to promote tumour growth and survival. We will also work toward incorporating additional fluorescent reporters for other reactive oxygen and nitrogen species including peroxynitrite and superoxide to gain a more comprehensive picture of the effects of chronic neuroinflammation.

Chapter 4 - Efforts toward developing applications of integrated dielectric elastomer actuator (IDEA) technology in microfluidics and cellular analysis

4.1 Introduction

One of the more appealing aspects of microfluidic-based analysis is the small laboratory footprint of microfluidic devices. However, it is common for the advantage offered by the small footprint of these devices to be essentially negated by the relatively bulky footprint of the peripheral equipment and accessories necessary for the operation of the device. A great deal of microfluidic research is dedicated to the goal of minimizing the footprint of that peripheral equipment by developing smaller, cheaper, and equally effective alternatives. Many of the operations carried out in microfluidic devices (e.g. fluid control, pumping, mixing, cell handling) are driven by some type of actuation or moving component. Pneumatic actuation is the most common modality for actuation in microfluidics because it is low-cost, robust, and fabrication of integrated pneumatically driven components is relatively facile in PDMS devices. However, pneumatic control systems are relatively bulky because they require a compressed air source, air filters, tubing, external valves, and a pressure regulator. Efforts to incorporate direct, on-board actuation mechanisms have been made including using a tactile braille text display with vertically moving pins to deform elastomeric channels,⁷⁸ or using a piezoelectric transducer operated at high frequencies to induce fluid flow via acoustic waves.⁷⁹ However, on-board actuation mechanisms such as these are either rather bulky, in the case of the braille display, or require expensive piezoelectric substrates and sophisticated equipment for operation.⁸⁰ There is

an ongoing effort in the field of microfluidics to develop a compact, inexpensive, easily-integrated, and highly modular means of actuation.

4.1.1 Dielectric elastomeric actuators

Recently, attention has been directed toward novel applications of a class of materials called “smart materials”. Smart materials are broadly defined as a material that changes a physical property in response to an environmental change. Piezoelectric materials are one such example as they change physical dimension upon application of an electrical potential. While piezoelectric materials are effective at producing mechanical actuation, they are expensive and not as simple to shape or pattern as other smart materials. One class of smart material that is worth exploration are dielectric elastomers (DEs). DEs are a specific type of smart material under the category of electroactive polymers. DEs, specifically, are electrically insulating polymers (dielectric) that are highly compliant polymers (elastomeric). Like piezoelectric transducers, dielectric elastomer actuators (DEAs) are responsive to external electric fields. A generic diagram of a DEA is shown in **Figure 4.1**.

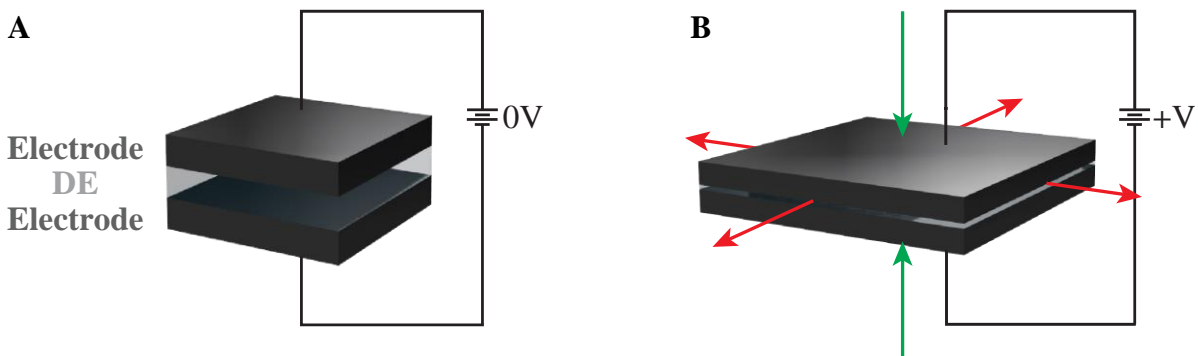


Figure 4.1 A diagram illustrating a generic DEA and its actuation. (A) A DE layer is sandwiched between two compliant electrodes with no electric field applied. (B) An electric field is applied causing compression in the z direction (green arrows) and expansion in the xy-plane (red arrows).

In general, a DEA unit is made by placing a thin (20-200 μm) DE layer between two electrodes. Upon application of an electric field across the dielectric layer, the attractive force between the oppositely charged electrodes induces Maxwell stress and causes the DE layer to compress in the z-direction and simultaneously stretch in the xy-plane due to the incompressibility of the DE layer material and the repulsion between like charges at the compliant electrode surfaces.⁸¹ The compression in the z-direction and the stretching in the xy-plane are mechanically coupled, and therefore, a single effective actuation pressure (p) can be described using Equation 4.1 derived by Pelrine et al.⁸²

$$p = \epsilon_0 \epsilon_r E_{cap}^2 = \epsilon_0 \epsilon_r \left(\frac{V}{z_0} \right)^2 \quad (4.1)$$

Where ϵ_0 is the permittivity of free space, ϵ_r is the relative permittivity of the dielectric (sometimes written as dielectric constant κ), E_{cap} is the applied electric field across thickness z_0 , and V is the applied voltage. It is worth noting that the Maxwell stress in a DEA with compliant electrodes is twice that of a parallel plate capacitor with rigid ones. This is due to the direct mechanical coupling of the z-direction compression and the xy-plane stretching mentioned above. The strain (S) induced in the DE layer in response to the Maxwell stress (p) can be described using Equation 4.2:⁸²

$$S = -sp = -\frac{\epsilon_0 \epsilon_r E_{cap}^2}{Y} \quad (4.2)$$

Where s is the compliance of the dielectric elastomer which is equal to the inverse Young's modulus (Y). The negative sign indicates that the strain is compressive as opposed to tensile (elongation). This relationship between S and p , also called the Hookean Model, holds true for strains of up to 10%, but breaks down above that threshold due to the change in Young's modulus as a function of strain.⁸² The relationship between stress and strain at strains above 10%

is better described by the Neo-Hookean or Mooney-Rivlin models that accounts for this change using additional physical constants specific to each material that must be determined experimentally.⁸³ While inaccurate at higher strains, Equation 4.1 still illustrates that the key properties of the dielectric material in determining actuation performance are the dielectric constant and the elasticity. The upper limits of these parameters are determined by the requirements for actuator performance in the final application. Higher strains may be achieved by increasing the compliance of the polymer; however, this limits the response frequency, which may prove to be an issue in higher frequency applications such as peristaltic pumping (~100 Hz). Similarly, increasing the dielectric constant of the material may improve actuator performance to a degree, but as the dielectric constant is increased the dielectric strength is decreased. Dielectric strength determines the maximum electric field that a material functions as an insulator before undergoing dielectric failure or dielectric breakdown. A photograph of a dielectric film that has undergone dielectric failure is shown in **Figure 4.2**.



Figure 4.2 A photograph of dielectric breakdown of a 40 μm PDMS film. As dielectric breakdown occurs, high energy electrons burn a hole through the film and a visible electrical arc can be observed.

4.1.2 DEA applications and potential

DEAs have recently increased in prevalence and are used in a wide variety of applications including tunable optical components, soft robotics, biomedical applications, energy harvesting, sensing, and microfluidics.⁸⁴

In the field of microfluidics, DEA is an attractive modality for actuation as an alternative to pneumatic actuation for several factors. DEA actuation only requires a voltage source and control electronics, both of which are already required in microfluidic applications that use electrophoresis as a separation method. Furthermore, microfluidic channels are typically filled with a conductive buffer solution and connected to high voltage electrodes, therefore, the microfluidic channels may be used as one of the compliant electrodes in the DEA unit. This style of integrated dielectric elastomeric actuator (IDEA) was demonstrated by the Culbertson group previously and was used to produce unbiased hydrodynamic injections for microfluidic electrophoretic separation, as well as a means of inducing mixing of 2 solutions within a microfluidic channel.⁸⁵⁻⁸⁶ The devices described were fabricated using PDMS which, in addition to being a commonly used material for microfluidic device fabrication, is a dielectric elastomer. PDMS is well-suited for use in DEA applications because it is relatively inexpensive, visibly transparent, biocompatible, has tunable flexibility, and is easily processed as a thin film (tens of microns thick) via spin coating.

This chapter will discuss efforts and progress toward developing two applications of integrated dielectric actuators. The first part will focus on work toward developing a solid-state dielectric actuation-based valve to replace quake valves. Simple model devices were designed and fabricated to evaluate the performance of the dielectric valves. Initial results are reported as images taken from video recordings of valve actuation as well as image analysis to measure

changes in valve deformation. The second part will detail early efforts to utilize the precision of dielectric actuation to control the deformation of a flexible substrate. Ultimately, cells will be seeded onto a flexible PMDS substrate, and upon actuation cells will be mechanically stretched. Future studies will investigate the potential mechanosensitivity of cells derived from glioblastoma multiforme (GBM) by monitoring for signs of anoikis, which is a specialized type of apoptosis that can be triggered by mechanical stimulation. Initial work in this application aims to perform surface modification of PDMS substrates so that they may be a more suitable substrate for anchorage dependent cell culture while minimally impacting cellular characteristics. These substrates will then be integrated into a microscale culture device that incorporates a dielectric actuator. Preliminary results are reported as cell culture images to confirm normal cell growth and attachment, contact angle measurements, and videoframes showing cell potential actuation induced cell movement.

4.2 Materials and methods

4.2.1 Reagents and materials

Negative tone photoresist SU-8 2010 was purchased from MicroChem Corp. (Newton, MA). The SU-8 developer, 2-(1-methoxy) propyl acetate (99%), was obtained from Acros (Morris Plains, NJ). AZ P4620 positive tone photoresist and AZ 400K developer (1:4) were obtained from AZ Electronic Materials (Branchburg, NJ). Silicon wafers (100 mm diameter, single-side polished, mechanical grade or better) were purchased from Silicon, Inc. (Boise, ID). Chrome coated silicon wafers (100 mm diameter, single-side polished, test grade) were purchased from WRS Materials (San Jose, CA). (1,1,1,3,3,3-Hexamethyldisilazane (98% (HMDS)) was purchased from Gelest (Morrisville, PA). Sylgard 184 PDMS prepolymer and

curing agent were purchased from Dow Corning (Corning Inc., Corning, NY). Ultrapure water was generated from a Barnstead E-pure system (Dubuque, IA). SIM-A9 microglial cells (mouse, ATCC CRL-3265) and Dulbecco's phosphate buffered saline (D-PBS, 1x ATCC 30-220) were purchased from American Type Culture Collection (Manassas, VA, USA). Dulbecco's Modified Eagle Medium/Nutrient Mixture F-12 (DMEM:F-12) was purchased from Thermo Fisher Scientific (Waltham, MA, USA). Indium tin oxide (ITO) coated glass slides (50 x 75 mm, 8-12 $\Omega\cdot\text{cm}$) were purchased from SPI supplies (West Chester, PA, USA).

4.2.2 Microchip design and fabrication for valve device

The IDEA device was fabricated using two layers of patterned PDMS, the bottom layer consisting of the fluidic manifold and the top containing a manifold of Quake valves (valve layer). The device is fabricated using standard photolithography to make silicon wafer master molds (SWMs) for subsequent multilayer soft lithography in a manner similar to that described in Chapter 2 and reported previously.¹ The 2-layer device was then placed atop an etched indium tin oxide (ITO) coated slide that has a thin film of PDMS covering the electrode surface. ITO was chosen as the electrode conductor because it is visibly transparent and is easily patterned using photolithography or tape masking, followed by hydrochloric acid etching. Other electrode materials (e.g. gold) tend to be more expensive, less visibly transparent, and require harsher chemicals for patterning.

Photolithography

Device fabrication began with a similar photolithography procedure described previously in Chapter 2 to generate 2 silicon wafer master (SWM). Briefly, the fluidic SWM was fabricated using the positive tone photoresist, AZ P4620, spin-coated onto a chrome coated silicon wafer

(1000 rpm for 18 s), yielding a film thickness of 18-20 μm . The subsequent soft and hard baking steps as well as exposure, development, and other finishing steps were performed exactly as described in Chapter 2.

The valve layer SWM was fabricated using the negative tone photoresist, SU-8 2010, also following a procedure previously described in Chapter 2. The SU-8 was spin-coated onto a bare silicon wafer (10000 rpm for 20 s) yielding a film thickness of 20 μm . Similarly, the baking, exposure, development and other finishing steps were also performed as described in Chapter 2.

Soft lithography

The 3-layer IDEA device for testing valve configurations was fabricated using a multi-layer soft lithography described in Chapter 2 and reported previously.¹ Briefly, 3 aliquots of PDMS with varying ratios of elastomer base to curing agent (approximately 30:1, 5:1, 10:1) were individually measured out, thoroughly mixed, and degassed in a vacuum desiccator. Both the fluidic and valve SWMs were pretreated with a releasing agent (1:1 (v/v) HMDS:Xylenes). The fluidic layer was made by spin coating a 50 μm thick layer of PDMS onto the fluidic SWM. The valve layer was made by pouring PDMS into a 5 mm thick plexiglass frame aligned on top of the valve SWM. Both layers were placed into an oven at 80 $^{\circ}\text{C}$ to cure for 90 min. Once cured, the layers were removed and allowed to cool.

The valve layer was then peeled off of the valve SWM and filling access holes were punched using an 18-gauge needle with the bevel cut off and sharpened. The valve layer was then cleaned and aligned atop the fluidic SWM being careful not to trap air between the layers. Excess 10:1 PDMS was then poured around the edge of the device to aid in device removal in the final step. A thin layer of 10:1 PDMS (40 μm) was fabricated on an ITO coated glass slide(50

x 75 mm) by pouring the remaining 10:1 PDMS onto the slide and spin coating at 2000 rpm for 45s. A piece of tape was placed onto the ITO slide prior to spin-coating for later removal to allow a small area of conductive ITO to be exposed for electrical contact. The assembled layers and PDMS coated slide were then placed into the 80 °C oven for a 90 min. Once fully cured and cooled, the 2-layer chip was then peeled off the fluidic SWM, and 3 mm diameter reservoir holes were punched out using a disposable biopsy punch. The 2-layer chip was then placed on top of the PDMS coated ITO slide to complete the fluidic channel.

4.2.3 Tissue culture

SIM-A9 cells were cultured lying flat in T75 polystyrene flasks (Fisher Scientific, Waltham, MA, USA) in a humidified environment at 37 °C and 5% CO₂ in Dulbecco's Modified Eagle Medium/Nutrient Mixture F-12 (DMEM:F-12) supplemented with heat inactivated fetal bovine serum (10% v/v), heat inactivated horse serum (5% v/v), and streptomycin (100 µg/mL). Once the cells reached 80% confluency, they were passaged. SIM-A9 cultures contain a mixture of adhered and suspended cells. Passaging begins by first scraping the attached cells using an in-house made glass scraper. Scraped cells and suspended cells were then mixed by pipetting and transferred to a 15 mL conical vial and centrifuged at 1000 rpm (or 125 x g) for 5 min. The supernatant was then discarded, and the cell pellet was resuspended in fresh media and split into flasks at a subcultivation ratio between 1:3 and 1:6 with a total culture volume of 15 mL. Detailed protocols for the cryopreservation, resuscitation and culture of SIM-A9 cells may be found in **Appendix A**.

4.2.4 Testing of valve device

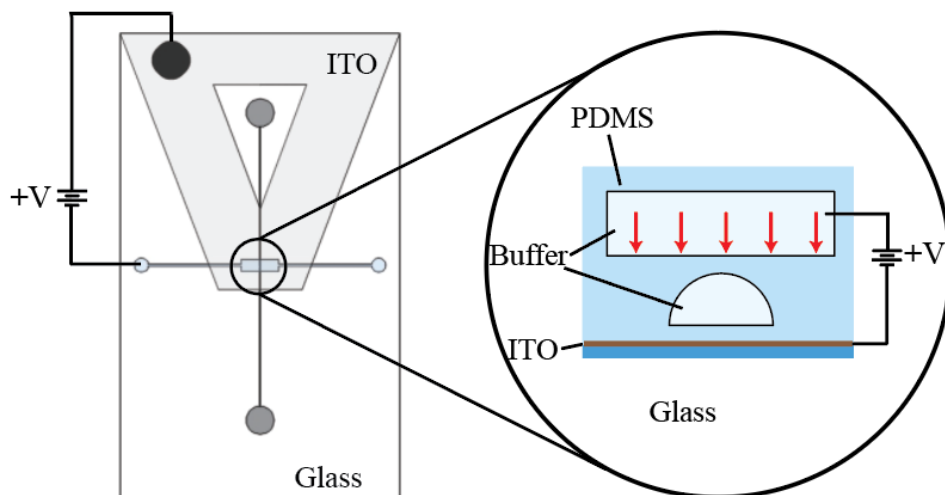


Figure 4.3 A diagram showing the general layout of the valve layer(light blue) and the fluidic layer (gray) atop the etched ITO electrode. The enlarged region (right) shows is a cartoon representation of the IDEA actuation unit. The red arrows indicate the direction of the compressive force generated upon actuation.

Actuation performance of the IDEA valve device (**Figure 4.3**) was performed by filling the fluidic channel with a solution of rhodamine B (50 μM) dissolved in an aqueous buffer solution of sodium borate (25 mM). Sodium borate was chosen to mimic the conditions of implementing IDEA valving in a microchip electrophoresis device, as borate buffers are a commonly used buffer system for electrophoretic separations. The valve layer was filled with borate solution without fluorophore to serve as the compliant electrode.

Actuation of the IDEA valve was driven by a high voltage power supply controlled using an in-house written LabVIEW program and a USB digital-to-analog converter (National Instruments, USB-6002). Electrical contact with the valve layer was made by inserting a platinum electrode wire into one of the two access holes. Contact with the ITO slide was made by adhering high voltage wire to the slide using a silver conductive epoxy. Actuation

performance of the device was monitored using a Nikon Eclipse TE2000-U inverted microscope equipped with a epi-luminescence system consisting of a mercury arc lamp and a G-2A fluorescence filter cube with a 535 nm bandpass filter for the excitation wavelength and a 590 nm long-pass emission filter. Video of IDEA device performance was captured using a Sony CCD color video camera mounted on the side port of the microscope. Video footage was analyzed by taking individual frames and importing them as images into ImageJ software. The software converts the color image to grayscale, so the light intensity of each pixel may be represented as a gray value. The device was actuated by applying voltages from 1.5 kV to 4 kV.

4.2.5 Mechanical stretching device fabrication, setup, and testing

PDMS surface modification testing

Ultimately, the PDMS surface will be modified with a biomolecule that is representative of the in vivo extracellular matrix for the cells. This will be done via covalent attachment of hyaluronic acid to the PDMS surface. To perform covalent attachments to a PDMS surface, the surface must first be activated. This is typically done using oxygen plasma treatment to generate surface silanol (Si-OH) groups. Unfortunately, our lab does not currently have oxygen plasma treatment capabilities. Instead we pursued an all wet chemical surface modification strategy. Not only is this strategy likely to be less expensive, but similar methods have produced surface modifications that last longer than those generated via oxygen plasma.⁸⁷ The process begins with treating PDMS with piranha solution (hydrogen peroxide:sulfuric acid, mixed 2:3) for 15 min follow by a rinse and then treatment with 1 M KOH solution. PDMS test substrates were treated according to the procedure from Maji et al. and contact angle measurements were performed to confirm the Si-OH formation indicated by an increase in hydrophilicity (or decrease in water contact angle). Contact angle photographs were taken using a camera (Sony alpha-6400)

equipped with a macro lens. Contact angle calculations were performed using ImageJ image analysis with a contact angle plugin.

Alongside efforts toward covalent attachment of biomolecules, a faster but less stable surface modification strategy was investigated to optimize culture conditions so that initial testing of the stretching device may proceed as soon as possible. Physisorption of molecules, such as poly-D-lysine, onto PDMS is a common strategy and has been reported previously.²⁰ Surface modification was tested using 24-well plates lined with 10:1 PDMS on the bottom. Surfaces were treated using a 0.2 mg/mL solution of poly-D-lysine (PDL) in PBS. Treatment was carried out by incubating the surfaces in the refrigerator (4 °C) overnight. The surfaces were then rinsed with PBS and cells were seeded at various densities. Proper monolayer growth was monitored by taking pictures using a camera mounted to a microscope.

Cell stretching device fabrication

A cartoon representation of the proposed design and working principles for the cell stretching device are shown in **Figure 4.4**. Fabrication begins with etching of the ITO slide to achieve the desired electrode pattern. The etched pattern on each ITO slide allows for 6 individual cell stretching devices.

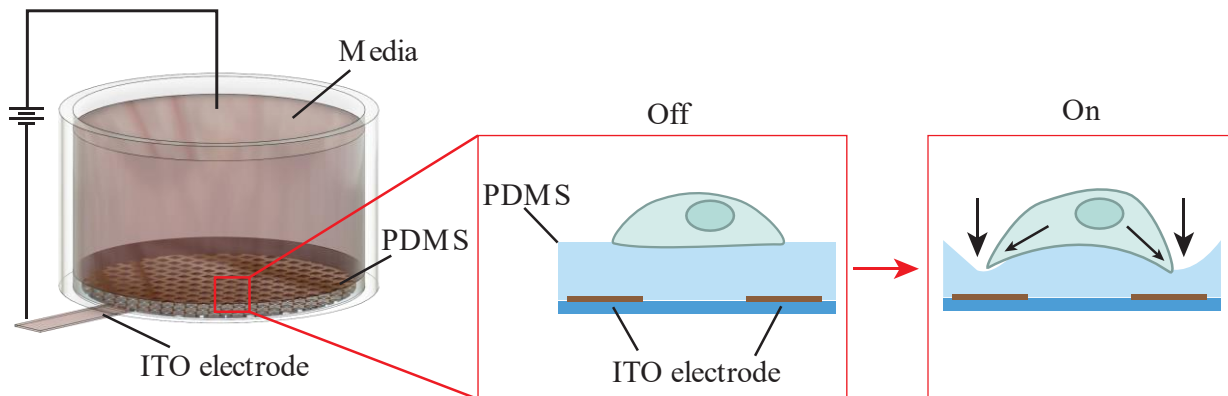


Figure 4.4 A cartoon of the proposed cell stretching device (left) and working principles of cell stretching (right); The electric field is applied across the PDMS membrane between the electrically conductive growth medium (GND) and the patterned ITO electrode (+V).

The ITO slide is prepared for patterning by spin coating a thin layer of positive tone photoresist AZ-P4620 at 2000 rpm for 17 s to achieve a thin layer. The photoresist coated slide is then baked following the same procedure mentioned in **Section 2.2.5**. Once baked, the AZ coated slide is left to cool and rehydrate for an hour. A photomask with the desired features is then placed on top of the AZ coated slide and the slide is then exposed according to the photoresist manufacturers recommended dosage (also mentioned previously in **Section 2.2.5**). The remaining steps of photoresist development and hard baking are the same as above. Once the AZ has been developed and baked, the undesired ITO may then be etched away by immersing the slide in a bath of 1 M hydrochloric acid for 30 min. Once the ITO has been etched, the remaining photoresist may be removed using a series of rinses, first with acetone, followed by isopropanol and finished with DI water.

Once the ITO has been etched in the desired grid pattern, it is then coated with a thin layer of 10:1 PDMS by spin coating at 1000 rpm for 45 s, yielding a membrane thickness of

approx. 40 μm . Scotch tape is placed over regions of the ITO prior to spin coating to allow easy removal of PDMS in the final steps for electrical contacts. The coated slide is then baked for 90 min at 80 °C. Once cured, 6 short lengths (~8 mm) of 5 mm i.d. glass tubing are placed atop the membrane each aligned with a grid patterned electrode to create reservoirs. The reservoirs are sealed in place by pouring 10:1 PDMS coating the remainder of the slide. The coated slide with reservoirs in place is then placed back into the 80 °C oven for a final 90 min curing period. Once cured, the PDMS over the tape covered areas is then cut using a scalpel and the tape is carefully removed to expose ITO to allow for electrical connection.

4.3 Results and discussion

4.3.1 Video analysis of valve actuation

The goal for IDEA actuation tests was to observe an open-to-close action of the valve. A decrease in the fluidic channel height would be indicated by seeing a decrease in fluorescent intensity upon actuation. However, following analysis of still frames taken during video recording of the IDEA actuation, it was observed that the fluorescent intensity increased rather than decreased. Photographs showing the location of the line scan used to measure the fluorescent intensity of the “Off” and “On” states and the accompanying data are shown in **Figure 4.5**. The actuation was characterized by subtracting the “Off” state fluorescent intensity line scan from that of the “On” state. The change in fluorescent intensity was directly proportional to the applied electric field. This is the opposite of the desired outcome.

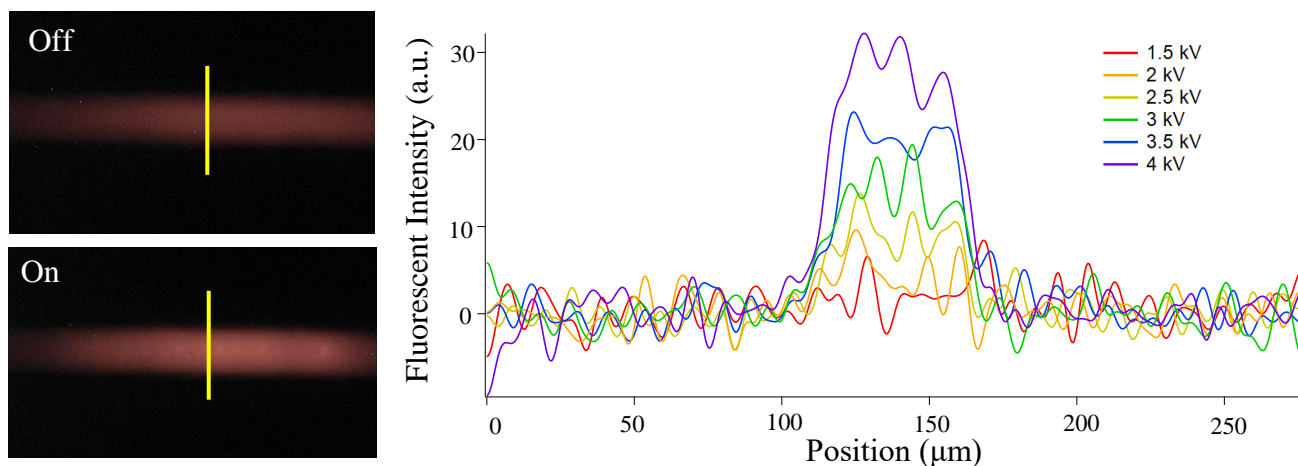


Figure 4.5 IDEA valve actuation data from video frame analysis using ImageJ software; (left) video stills of the off and on states of the IDEA, the yellow lines indicate where intensity data were measured; (right) change in fluorescent intensity between the on and off actuation states.

It is possible that the conductivity of the solution within the fluidic channel is impacting the ability of the IDEA to function as an open-to-close valve. This hypothesis was tested by leaving the fluidic channel empty and applying the same electric fields. This appeared to result in the desired action, however we cannot confirm this using the same method as the fluorescent solution is no longer there to aid in visualization. If the valve is indeed closing with no fluid in the fluidic channel, then the current configuration for the IDEA valve is not suitable for applications in microfluidics.

4.3.2 Development of mechanical stretching device

PDMS surface treatment with piranha and KOH

Ideally the surface of the PDMS should be modified to resemble the extracellular matrix that corresponds to the cells' organ of origin. In the case of glioblastoma multiforme (GBM), hyaluronic acid (HA) is not only present in the brain, but also plays a potential role in the

invasiveness of gliomas.⁸⁸ Additionally, it is important that the surface modification be stable enough to remain relatively unchanged during the course of mechanical stimulation. Initial efforts have been aimed toward optimizing the wet chemical pre-treatment of PDMS substrates using the piranha:KOH solution procedure. Contact angle photographs of the native and modified PDMS substrates are shown in **Figure 4.6**.

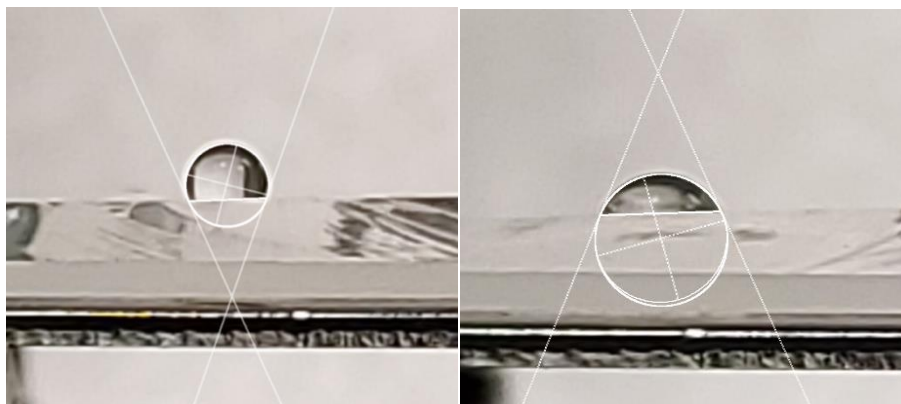


Figure 4.6 Contact angle measurements of native (left) and modified (right) PDMS substrates; Native PDMS contact angle was measured at 110° , modified PDMS contact angle was measured at 66.4° .

Successful improvement of surface wettability was indicated by a substantial decrease in water contact angle from 110° to 66.4° . While this is promising, falls well short of the improvements reported by Maji.⁸⁷ Additionally, the surface modification was tested on thinner PDMS membrane substrates (approx. $40\ \mu\text{m}$) to test its suitability for use in the cell stretching device which requires a thin membrane to achieve actuation. Unfortunately, the membrane was too weak to withstand the harsh chemical treatment. Future efforts will be directed toward reaching the same low contact angle of 27.0° reported by Maji. Once that is optimized, we will confirm the presence of surface Si-OH groups using FTIR or by covalently attaching a

fluorescent reporter enabling visualization of successful surface attachment. We will also optimize the membrane thickness such that it is substantial enough to withstand the harsh treatment but is also able to produce sufficient strains to mechanically stimulate the cells. To continue with the covalent attachment of hyaluronic acid, it is also important to consider the solvent compatibility of PDMS. PDMS will swell when exposed to many common organic solvents, and the PDMS may retain some small amount of organic solvents that could potentially leech out during experiments where cells are seeded on the substrate resulting in inadvertent cell death. Continuing efforts are being made to devise an aqueous covalent attachment strategy.

Treatment of PDMS surfaces for tissue culture suitability

PDL is a common surface modifier for cell attachment and is ideal for cells of glial origin, as they prefer positively charged surfaces.⁸⁹ For surface treatment experiments, SIM-A9 microglia serve as the model cell line. SIM-A9 microglia are a spontaneously immortalized mouse cell line. The line was discovered in 2014 when a sub-population of primary microglia isolated from postnatal murine cerebral cortices was observed to continue to proliferate after 14 days.⁶⁶ This particular line was chosen because it may be cultured in our BSL-1 facilities, and because it is from the same organ of interest as GBM and, therefore, any surface treatments developed will likely produce similar results with GBM cells. Photographs of cells on native PDMS and PDL treated PDMS are shown in **Figure 4.7**. Cells grown on native PDMS tended to grow in clumps instead of a neat monolayer that is observed on the PDL surface. The cell monolayer was stable for at least 48 hours under culture conditions (37 °C, 5% CO₂). This surface treatment appears to be sufficient to support cell attachment for the duration of the mechanical stretching experiments.

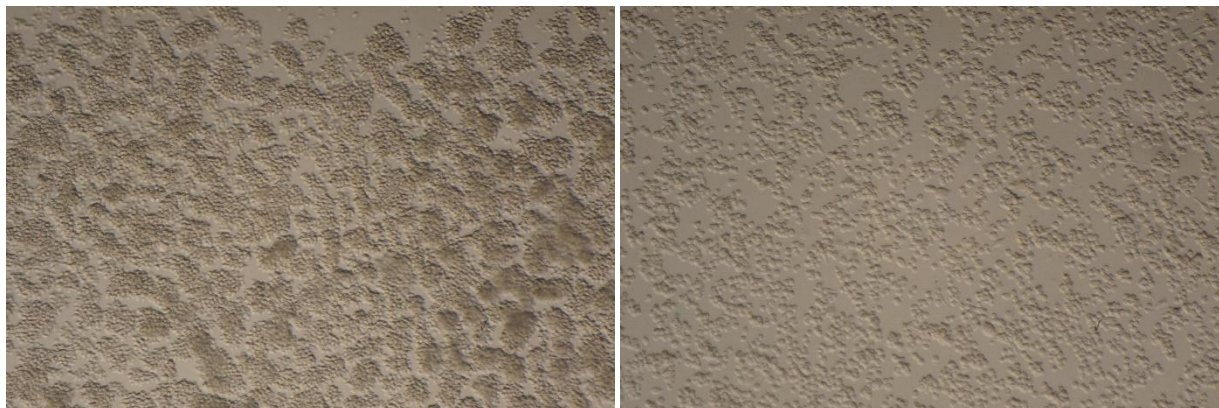


Figure 4.7 Photographs taken 24 after cells seeded on native (left) and PDL treated (right) PDMS substrates.

4.4 Concluding remarks

The development of IDEA technologies for applications in microfluidic in our lab is still in its infancy, however, we believe that these efforts are worthwhile in the pursuit of truly standalone miniaturized lab-on-a-chip technologies. An initial IDEA-based valve configuration was fabricated, and its performance was evaluated by attempting actuation at voltages from 1.5 to 4 kV. If open-to-close actuation was achieved, this would have been indicated by a decrease in fluorescence intensity in the fluidic channel. The degree of the decrease in fluorescence intensity was expected to correlate with the voltage applied. Unfortunately, we observed an increase in fluorescence intensity which suggests that the fluidic channel is expanding or dilating. It appears as though this was caused by the conductivity of the solution within the fluidic channel. Future efforts will be directed toward developing an IDEA-based valve configuration that circumvents this issue.

Early efforts in applying IDEA actuation to the mechanical stimulation of adherent cells are currently underway. Thus far we have seen promising results in developing surface pre-treatment strategies to modify the PDMS surface to be more amenable to normal cell growth. We

will be continuing development of a more robust and stable surface treatment by working toward a wet chemical covalent modification strategy. Preliminary contact angle measurements following the first step of the surface modification are encouraging but will require further optimization. Additionally, we have begun work on fabricating the grid electrode IDEA cell stretching device (pictured in **Figure 4.4**). A series of grid patterned electrodes have been etched into ITO coated glass using photolithographic patterning followed by HCl etching of the electrode. Photographs of the initial electrodes may be found in **Appendix B**. The actuation performance of the grid electrode IDEA cell stretching device will be characterized either by video analysis or possibly by shining a laser onto the surface and seeing if a diffraction pattern is generated due to the change in the surface topology of the PDMS membrane.

Our ultimate goal is to develop a benchtop microfluidic analytical system that only requires a power outlet to function and eliminating the need for bulky external compressed air sources will significantly move our efforts forward.

Chapter 5 - Future direction

The projects described previously can be separated into 2 major project areas: microfluidic single-cell analysis of NO levels and development of applications for IDEA technology for microfluidics and cellular analysis.

Major developments in the single-cell NO measurement project was shown in the progression from Chapter 2 to Chapter 3, however there are still characteristics and capabilities that we plan to explore. The next steps of the project will focus on 2 major aspects of the analysis: 1. Factors that impact the distribution of NO levels in cell populations (e.g. cell-type, organ of origin, method of immortalization, passage number/age, media composition, ascorbic acid levels, inhibition of regulatory mechanisms). 2. The capability of the analysis strategy for screening of potential iNOS inhibitors and characterizing their performance in terms of overall efficacy as well as insight into the mechanism of action by analyzing the population data. By pursuing these 2 branches of the project, we hope to gain a deeper understanding of the important factors that influence our analysis while also demonstrating the powerful potential of this type of measurement strategy for applications in the in vitro stages of pharmaceutical development.

Future efforts on the valve portion of the IDEA project will be aimed at exploring other valve configurations that are compatible with DEA actuation. Potential strategies that will be explored include incorporating flexible electrode materials (ionic liquids, conductive polymers and gels) as well as exploring other dielectric materials (acrylic polymers, modified PDMS, dielectric liquids). As for the mechanical stimulation portion of the IDEA project, future efforts will be directed toward continuing the development of a device capable of mechanically stimulating cells for an extended period of time. While we are working on developing an IDEA-

based device for mechanical stimulation, we will also be exploring the use of ultrasound as a source of mechanical perturbation. The ultimate goal is to develop the device into a form that can be easily coupled to the microfluidic single-cell analysis device. Once coupled, a cell population may then be mechanically stimulated for a prescribed period of time, then the cells can be treated with fluorogenic probes or tagged peptide substrates before being drawn into the SCA device where the cells can be lysed and the contents can be separated and quantified. Once this has been achieved, we will study the mechanosensitivity of cancer cells such as B35 rat neuroblastoma cells or C6 rat glioma cells. We hope to eventually measure a set of biomarkers and enzyme activities associated with mechanically induced apoptosis to better understand this behavior to aid in the development of a cancer treatment strategy that exploits this phenomena.

References

1. Patabadige, D. E.; Mickleburgh, T.; Ferris, L.; Brummer, G.; Culbertson, A. H.; Culbertson, C. T., High-throughput microfluidic device for single cell analysis using multiple integrated soft lithographic pumps. *Electrophoresis* **2016**, *37* (10), 1337-44.
2. Limpert, E.; Stahel, W. A.; Abbt, M., Log-normal Distributions across the Sciences: Keys and Clues. *BioScience* **2001**, *51* (5), 341-352.
3. Patabadige, D. E.; Sadeghi, J.; Kalubowilage, M.; Bossmann, S. H.; Culbertson, A. H.; Latifi, H.; Culbertson, C. T., Integrating Optical Fiber Bridges in Microfluidic Devices to Create Multiple Excitation/Detection Points for Single Cell Analysis. *Anal Chem* **2016**, *88* (20), 9920-9925.
4. Sibbitts, J.; Sadeghi, J.; Culbertson, C. T., Microelectrophoretic single-cell measurements with microfluidic devices. *Methods Enzymol* **2019**, *628*, 223-241.
5. Kutter, J. P.; Fintschenko, Y., *Separation Methods in Microanalytical Systems*. CRC Press LLC: 2006; p 575 pp.
6. Skoog, D. A.; Holler, F. J.; Crouch, S. R., *Principles of instrumental analysis*. Seventh edition. ed.; Cengage Learning: Australia, 2018; p xix, 959 pages.
7. Ou, X.; Chen, P.; Huang, X.; Li, S.; Liu, B. F., Microfluidic chip electrophoresis for biochemical analysis. *J Sep Sci* **2020**, *43* (1), 258-270.
8. Petersen, J. R.; Mohammad, A. A., *Clinical and forensic applications of capillary electrophoresis*. Humana Press: Totowa, N.J., 2001; p x, 453 p.
9. Harris, D. C.; Lucy, C. A., *Quantitative chemical analysis*. Ninth edition. ed.; W.H. Freeman & Company: New York, 2016; p 1 volume (various pagings).
10. Lauer, H. H.; Rozing, G. P., *High Performance Capillary Electrophoresis: A Primer*. 2 ed.; Agilent Technologies: Santa Clara, CA, 2018.
11. Li, X.; Zhou, Y., *Microfluidic devices for biomedical applications*. Woodhead Publishing: Cambridge, UK, 2013; p xxiii, 652 pages.
12. Terry, S. C.; Jerman, J. H.; Angell, J. B., Gas Chromatographic Air Analyzer Fabricated on a Silicon Wafer. *Ieee T Electron Dev* **1979**, *26* (12), 1880-1886.
13. Sibbitts, J.; Sellens, K. A.; Jia, S.; Klasner, S. A.; Culbertson, C. T., Cellular Analysis Using Microfluidics. *Anal Chem* **2018**, *90* (1), 65-85.
14. Patabadige, D. E.; Jia, S.; Sibbitts, J.; Sadeghi, J.; Sellens, K.; Culbertson, C. T., Micro Total Analysis Systems: Fundamental Advances and Applications. *Anal Chem* **2016**, *88* (1), 320-38.
15. Gale, K. B.; Jafek, R. A.; Lambert, J. C.; Goenner, L. B.; Moghimifam, H.; Nze, C. U.; Kamarapu, K. S., A Review of Current Methods in Microfluidic Device Fabrication and Future Commercialization Prospects. *Inventions* **2018**, *3* (3).
16. Guckenberger, D. J.; de Groot, T. E.; Wan, A. M.; Beebe, D. J.; Young, E. W., Micromilling: a method for ultra-rapid prototyping of plastic microfluidic devices. *Lab Chip* **2015**, *15* (11), 2364-78.
17. Bhattacharjee, N.; Urrios, A.; Kang, S.; Folch, A., The upcoming 3D-printing revolution in microfluidics. *Lab Chip* **2016**, *16* (10), 1720-42.
18. Raj, M. K.; Chakraborty, S., PDMS microfluidics: A mini review. *J Appl Polym Sci* **2020**, *137* (27).

19. Nguyen, H. T.; Thach, H.; Roy, E.; Huynh, K.; Perrault, C. M., Low-Cost, Accessible Fabrication Methods for Microfluidics Research in Low-Resource Settings. *Micromachines (Basel)* **2018**, *9* (9).
20. Halldorsson, S.; Lucumi, E.; Gomez-Sjoberg, R.; Fleming, R. M. T., Advantages and challenges of microfluidic cell culture in polydimethylsiloxane devices. *Biosens Bioelectron* **2015**, *63*, 218-231.
21. Agostini, M.; Greco, G.; Cecchini, M., Polydimethylsiloxane (PDMS) irreversible bonding to untreated plastics and metals for microfluidics applications. *APL Materials* **2019**, *7* (8), 081108.
22. Unger, M. A.; Chou, H. P.; Thorsen, T.; Scherer, A.; Quake, S. R., Monolithic microfabricated valves and pumps by multilayer soft lithography. *Science* **2000**, *288* (5463), 113-6.
23. Marusyk, A.; Almendro, V.; Polyak, K., Intra-tumour heterogeneity: a looking glass for cancer? *Nat Rev Cancer* **2012**, *12* (5), 323-34.
24. Niepel, M.; Spencer, S. L.; Sorger, P. K., Non-genetic cell-to-cell variability and the consequences for pharmacology. *Curr Opin Chem Biol* **2009**, *13* (5-6), 556-61.
25. Berridge, M. J., Inositol trisphosphate and calcium signalling. *Nature* **1993**, *361* (6410), 315-25.
26. Bogdan, C., Nitric oxide and the immune response. *Nat Immunol* **2001**, *2* (10), 907-16.
27. Pacher, P.; Beckman, J. S.; Liaudet, L., Nitric oxide and peroxynitrite in health and disease. *Physiol Rev* **2007**, *87* (1), 315-424.
28. Caruso, G.; Fresta, C. G.; Siegel, J. M.; Wijesinghe, M. B.; Lunte, S. M., Microchip electrophoresis with laser-induced fluorescence detection for the determination of the ratio of nitric oxide to superoxide production in macrophages during inflammation. *Anal Bioanal Chem* **2017**, *409* (19), 4529-4538.
29. Metto, E. C.; Evans, K.; Barney, P.; Culbertson, A. H.; Gunasekara, D. B.; Caruso, G.; Hulvey, M. K.; Fracassi da Silva, J. A.; Lunte, S. M.; Culbertson, C. T., An integrated microfluidic device for monitoring changes in nitric oxide production in single T-lymphocyte (Jurkat) cells. *Anal Chem* **2013**, *85* (21), 10188-95.
30. Salentijn, G. I. J.; Oleschuk, R. D.; Verpoorte, E., 3D-Printed Paper Spray Ionization Cartridge with Integrated Desolvation Feature and Ion Optics. *Anal Chem* **2017**, *89* (21), 11419-11426.
31. Salentijn, G. I. J.; Permentier, H. P.; Verpoorte, E., 3D-Printed Paper Spray Ionization Cartridge with Fast Wetting and Continuous Solvent Supply Features. *Anal Chem* **2014**, *86* (23), 11657-11665.
32. Davis, E. J.; Jones, M.; Thiel, D. A.; Pauls, S., Using Open-Source, 3D Printable Optical Hardware To Enhance Student Learning in the Instrumental Analysis Laboratory. *J Chem Educ* **2018**, *95* (4), 672-677.
33. Meloni, G. N., 3D Printed and Microcontrolled: The One Hundred Dollars Scanning Electrochemical Microscope. *Anal Chem* **2017**, *89* (17), 8643-8649.
34. Grinias, J. P.; Whitfield, J. T.; Guetschow, E. D.; Kennedy, R. T., An Inexpensive, Open-Source USB Arduino Data Acquisition Device for Chemical Instrumentation. *J Chem Educ* **2016**, *93* (7), 1316-1319.
35. Delaney, C.; McCluskey, P.; Coleman, S.; Whyte, J.; Kent, N.; Diamond, D., Precision control of flow rate in microfluidic channels using photoresponsive soft polymer actuators. *Lab Chip* **2017**, *17* (11), 2013-2021.

36. Soenksen, L. R.; Kassis, T.; Noh, M.; Griffith, L. G.; Trumper, D. L., Closed-loop feedback control for microfluidic systems through automated capacitive fluid height sensing. *Lab Chip* **2018**, *18* (6), 902-914.
37. Im, S. B.; Uddin, M. J.; Jin, G. J.; Shim, J. S., A disposable on-chip microvalve and pump for programmable microfluidics. *Lab Chip* **2018**.
38. Bektik, E.; Dennis, A.; Prasanna, P.; Madabhushi, A.; Fu, J. D., Single cell qPCR reveals that additional HAND2 and microRNA-1 facilitate the early reprogramming progress of seven-factor-induced human myocytes. *Plos One* **2017**, *12* (8).
39. Turner, A. H.; Lebhar, M. S.; Proctor, A.; Wang, Q.; Lawrence, D. S.; Allbritton, N. L., Rational Design of a Dephosphorylation-Resistant Reporter Enables Single-Cell Measurement of Tyrosine Kinase Activity. *ACS Chem Biol* **2016**, *11* (2), 355-62.
40. Dickinson, A. J.; Meyer, M.; Pawlak, E. A.; Gomez, S.; Jaspers, I.; Allbritton, N. L., Analysis of sphingosine kinase activity in single natural killer cells from peripheral blood. *Integr Biol (Camb)* **2015**, *7* (4), 392-401.
41. Proctor, A.; Herrera-Loeza, S. G.; Wang, Q.; Lawrence, D. S.; Yeh, J. J.; Allbritton, N. L., Measurement of protein kinase B activity in single primary human pancreatic cancer cells. *Anal Chem* **2014**, *86* (9), 4573-80.
42. Wang, Y.; Li, J.; Feng, L.; Yu, J.; Zhang, Y.; Ye, D.; Chen, H. Y., Lysosome-Targeting Fluorogenic Probe for Cathepsin B Imaging in Living Cells. *Anal Chem* **2016**, *88* (24), 12403-12410.
43. Chen, Z.; Li, Q.; Sun, Q.; Chen, H.; Wang, X.; Li, N.; Yin, M.; Xie, Y.; Li, H.; Tang, B., Simultaneous determination of reactive oxygen and nitrogen species in mitochondrial compartments of apoptotic HepG2 cells and PC12 cells based on microchip electrophoresis-laser-induced fluorescence. *Anal Chem* **2012**, *84* (11), 4687-94.
44. Mainz, E. R.; Gunasekara, D. B.; Caruso, G.; Jensen, D. T.; Hulvey, M. K.; da Silva, J. A. F.; Metto, E. C.; Culbertson, A. H.; Culbertson, C. T.; Lunte, S. M., Monitoring intracellular nitric oxide production using microchip electrophoresis and laser-induced fluorescence detection. *Anal Methods-Uk* **2012**, *4* (2), 414-420.
45. Trotta, T.; Porro, C.; Calvello, R.; Panaro, M. A., Biological role of Toll-like receptor-4 in the brain. *J Neuroimmunol* **2014**, *268* (1-2), 1-12.
46. Garvey, E. P.; Oplinger, J. A.; Furfine, E. S.; Kiff, R. J.; Laszlo, F.; Whittle, B. J. R.; Knowles, R. G., 1400W is a slow, tight binding, and highly selective inhibitor of inducible nitric oxide synthase in vitro and in vivo. *J Biol Chem* **1997**, *272* (8), 4959-4963.
47. Zhu, Y.; Nikolic, D.; Van Breemen, R. B.; Silverman, R. B., Mechanism of inactivation of inducible nitric oxide synthase by amidines. Irreversible enzyme inactivation without inactivator modification. *J Am Chem Soc* **2005**, *127* (3), 858-68.
48. Di Virgilio, F.; Steinberg, T. H.; Silverstein, S. C., Inhibition of Fura-2 sequestration and secretion with organic anion transport blockers. *Cell Calcium* **1990**, *11* (2-3), 57-62.
49. Sadeghi, J.; Patabadige, D. E.; Culbertson, A. H.; Latifi, H.; Culbertson, C. T., Out-of-plane integration of a multimode optical fiber for single particle/cell detection at multiple points on a microfluidic device with applications to particle/cell counting, velocimetry, size discrimination and the analysis of single cell lysate injections. *Lab Chip* **2016**, *17* (1), 145-155.
50. Weller, J.; Budson, A., Current understanding of Alzheimer's disease diagnosis and treatment. *F1000Res* **2018**, *7*.
51. Maiti, P.; Manna, J.; Dunbar, G. L., Current understanding of the molecular mechanisms in Parkinson's disease: Targets for potential treatments. *Transl Neurodegener* **2017**, *6*, 28.

52. Makinde, H. M.; Just, T. B.; Cuda, C. M.; Perlman, H.; Schwulst, S. J., The Role of Microglia in the Etiology and Evolution of Chronic Traumatic Encephalopathy. *Shock* **2017**, *48* (3), 276-283.
53. Guillot-Sestier, M. V.; Town, T., Let's make microglia great again in neurodegenerative disorders. *J Neural Transm (Vienna)* **2018**, *125* (5), 751-770.
54. Arcuri, C.; Fioretti, B.; Bianchi, R.; Mecca, C.; Tubaro, C.; Beccari, T.; Franciolini, F.; Giambanco, I.; Donato, R., Microglia-glioma cross-talk: a two way approach to new strategies against glioma. *Front Biosci (Landmark Ed)* **2017**, *22*, 268-309.
55. da Fonseca, A. C.; Amaral, R.; Garcia, C.; Geraldo, L. H.; Matias, D.; Lima, F. R., Microglia in Cancer: For Good or for Bad? *Adv Exp Med Biol* **2016**, *949*, 245-261.
56. McKenzie, J. A.; Spielman, L. J.; Pointer, C. B.; Lowry, J. R.; Bajwa, E.; Lee, C. W.; Klegeris, A., Neuroinflammation as a Common Mechanism Associated with the Modifiable Risk Factors for Alzheimer's and Parkinson's Diseases. *Curr Aging Sci* **2017**, *10* (3), 158-176.
57. Elder, G. A.; Ehrlich, M. E.; Gandy, S., Relationship of traumatic brain injury to chronic mental health problems and dementia in military veterans. *Neurosci Lett* **2019**, *707*, 134294.
58. Sousa, C.; Biber, K.; Michelucci, A., Cellular and Molecular Characterization of Microglia: A Unique Immune Cell Population. *Front Immunol* **2017**, *8*, 198.
59. Biber, K.; Owens, T.; Boddeke, E., What is microglia neurotoxicity (Not)? *Glia* **2014**, *62* (6), 841-854.
60. Heppner, F. L.; Ransohoff, R. M.; Becher, B., Immune attack: the role of inflammation in Alzheimer disease. *Nat Rev Neurosci* **2015**, *16* (6), 358-72.
61. Guix, F. X.; Urbesalgo, I.; Coma, M.; Munoz, F. J., The physiology and pathophysiology of nitric oxide in the brain. *Prog Neurobiol* **2005**, *76* (2), 126-52.
62. Brown, G. C.; Bal-Price, A., Inflammatory neurodegeneration mediated by nitric oxide, glutamate, and mitochondria. *Mol Neurobiol* **2003**, *27* (3), 325-55.
63. Yuste, J. E.; Tarragon, E.; Campuzano, C. M.; Ros-Bernal, F., Implications of glial nitric oxide in neurodegenerative diseases. *Front Cell Neurosci* **2015**, *9*, 322.
64. Siegel, J. M.; Schilly, K. M.; Wijesinghe, M. B.; Caruso, G.; Fresta, C. G.; Lunte, S. M., Optimization of a microchip electrophoresis method with electrochemical detection for the determination of nitrite in macrophage cells as an indicator of nitric oxide production. *Anal Methods* **2019**, *11* (2), 148-156.
65. Kim, W. S.; Ye, X.; Rubakhin, S. S.; Sweedler, J. V., Measuring nitric oxide in single neurons by capillary electrophoresis with laser-induced fluorescence: use of ascorbate oxidase in diaminofluorescein measurements. *Anal Chem* **2006**, *78* (6), 1859-65.
66. Nagamoto-Combs, K.; Kulas, J.; Combs, C. K., A novel cell line from spontaneously immortalized murine microglia. *J Neurosci Methods* **2014**, *233* (1872-678X (Electronic)), 187-98.
67. Mainz, E. R.; Gunasekara, D. B.; Caruso, G.; Jensen, D. T.; Hulvey, M. K.; Fracassi da Silva, J. A.; Metto, E. C.; Culbertson, A. H.; Culbertson, C. T.; Lunte, S. M., Monitoring intracellular nitric oxide production using microchip electrophoresis and laser-induced fluorescence detection. *Anal Methods-Uk* **2012**, *4* (2), 414-420.
68. Shapiro, S. S.; Wilk, M. B., An Analysis of Variance Test for Normality (Complete Samples). *Biometrika* **1965**, *52* (3/4), 591-611.
69. Ghasemi, A.; Zahediasl, S., Normality tests for statistical analysis: a guide for non-statisticians. *Int J Endocrinol Metab* **2012**, *10* (2), 486-9.

70. Harrison, F. E.; May, J. M., Vitamin C function in the brain: vital role of the ascorbate transporter SVCT2. *Free Radic Biol Med* **2009**, *46* (6), 719-30.
71. Zhang, X. Y.; Xu, Z. P.; Wang, W.; Cao, J. B.; Fu, Q.; Zhao, W. X.; Li, Y.; Huo, X. L.; Zhang, L. M.; Li, Y. F.; Mi, W. D., Vitamin C alleviates LPS-induced cognitive impairment in mice by suppressing neuroinflammation and oxidative stress. *Int Immunopharmacol* **2018**, *65*, 438-447.
72. Portugal, C. C.; Socodato, R.; Canedo, T.; Silva, C. M.; Martins, T.; Coreixas, V. S.; Loiola, E. C.; Gess, B.; Rohr, D.; Santiago, A. R.; Young, P.; Minshall, R. D.; Paes-de-Carvalho, R.; Ambrosio, A. F.; Relvas, J. B., Caveolin-1-mediated internalization of the vitamin C transporter SVCT2 in microglia triggers an inflammatory phenotype. *Sci Signal* **2017**, *10* (472).
73. Feinerman, O.; Veiga, J.; Dorfman, J. R.; Germain, R. N.; Altan-Bonnet, G., Variability and robustness in T cell activation from regulated heterogeneity in protein levels. *Science* **2008**, *321* (5892), 1081-4.
74. Lu, Y.; Biancotto, A.; Cheung, F.; Remmers, E.; Shah, N.; McCoy, J. P.; Tsang, J. S., Systematic Analysis of Cell-to-Cell Expression Variation of T Lymphocytes in a Human Cohort Identifies Aging and Genetic Associations. *Immunity* **2016**, *45* (5), 1162-1175.
75. McClain, M. A.; Culbertson, C. T.; Jacobson, S. C.; Allbritton, N. L.; Sims, C. E.; Ramsey, J. M., Microfluidic devices for the high-throughput chemical analysis of cells. *Anal Chem* **2003**, *75* (21), 5646-55.
76. Guillot-Sestier, M. V.; Town, T., Let's make microglia great again in neurodegenerative disorders. *J Neural Transm* **2018**, *125* (5), 751-770.
77. Lv, J.; Wang, W.; Zhu, X.; Xu, X.; Yan, Q.; Lu, J.; Shi, X.; Wang, Z.; Zhou, J.; Huang, X.; Wang, J.; Duan, W.; Shen, X., DW14006 as a direct AMPK α 1 activator improves pathology of AD model mice by regulating microglial phagocytosis and neuroinflammation. *Brain Behav Immun* **2020**.
78. Gu, W.; Zhu, X.; Futai, N.; Cho, B. S.; Takayama, S., Computerized microfluidic cell culture using elastomeric channels and Braille displays. *Proceedings of the National Academy of Sciences of the United States of America* **2004**, *101* (45), 15861.
79. Huang, P. H.; Nama, N.; Mao, Z.; Li, P.; Rufo, J.; Chen, Y.; Xie, Y.; Wei, C. H.; Wang, L.; Huang, T. J., A reliable and programmable acoustofluidic pump powered by oscillating sharp-edge structures. *Lab Chip* **2014**, *14* (22), 4319-23.
80. Murray, C.; McCoul, D.; Sollier, E.; Ruggiero, T.; Niu, X.; Pei, Q.; Carlo, D. D., Electro-adaptive microfluidics for active tuning of channel geometry using polymer actuators. *Microfluidics and Nanofluidics* **2013**, *14* (1-2), 345-358.
81. O'Halloran, A.; O'Malley, F.; McHugh, P., A review on dielectric elastomer actuators, technology, applications, and challenges. *Journal of Applied Physics* **2008**, *104* (7), 071101.
82. Pelrine, R. E.; Kornbluh, R. D.; Joseph, J. P., Electrostriction of polymer dielectrics with compliant electrodes as a means of actuation. *Sensors and Actuators A: Physical* **1998**, *64* (1), 77-85.
83. Macosko, C. W., *Rheology : principles, measurements, and applications*. New York : VCH: New York, 1994.
84. Rosset, S.; Shea, H. R., Small, fast, and tough: Shrinking down integrated elastomer transducers. *Applied Physics Reviews* **2016**, *3* (3), 031105.
85. Price, A. K.; Anderson, K. M.; Culbertson, C. T., Demonstration of an integrated electroactive polymer actuator on a microfluidic electrophoresis device. *Lab Chip* **2009**, *9* (14), 2076-84.

86. Price, A. K.; Culbertson, C. T., Generation of nonbiased hydrodynamic injections on microfluidic devices using integrated dielectric elastomer actuators. *Anal Chem* **2009**, *81* (21), 8942-8.
87. Maji, D.; Lahiri, S. K.; Das, S., Study of hydrophilicity and stability of chemically modified PDMS surface using piranha and KOH solution. *Surface and Interface Analysis* **2012**, *44* (1), 62-69.
88. Park, J. B.; Kwak, H. J.; Lee, S. H., Role of hyaluronan in glioma invasion. *Cell Adh Migr* **2008**, *2* (3), 202-7.
89. Tanyeri, M.; Tay, S., Viable cell culture in PDMS-based microfluidic devices. *Methods Cell Biol* **2018**, *148*, 3-33.

Appendix A - Protocols

SIM-A9 Cryopreservation protocol (adapted by Jay Sibbitts from ATCC.org)

**READ THE ENTIRE PROTOCOL BEFORE BEGINNING. CERTAIN STEPS ARE
TIME SENSITIVE**

Materials and equipment:

- DMEM F-12 with 10% DMSO (b/w 17-25 °C)
- DMEM F-12 for media replenish 24 hours prior
- 1.0 mL Nunc vials
- Mr. Frosty freezing container with enough fresh isopropanol

Preparation procedure (to be done 24 hours prior to cryopreservation):

1. Ensure that you have the following ready:
 - a. Fresh freeze medium (complete DMEM F-12 with 10% DMSO)
 - b. Nalgene freezing container with isopropanol
 - c. Ensure that the liquid nitrogen level in the dewar is at 18 cm (this will allow for 2 vials in each cane to be stored in the vapor phase)
2. Prepare the cells for cryopreservation by first verifying 60-70% confluency and >95% viability using trypan blue and the hemocytometer (Only perform a viability count if uncertain because this requires scraping the adherent cells). Postpone cryopreservation if cells are at 80% confluency and passage them at a ratio of 1/3
3. Replenish the media in the flask by removing the supernatant and suspended cells and transferring them into a 15 mL conical vial and then centrifuge at 1000 rpm for 5 min.
4. While the cells are spinning, add 10 mL of fresh DMEM F-12 to the flask (without DMSO) * (assuming culturing in 75 cm² flask with a total volume of 15 mL) *
5. Once the cells have been spun down, wipe the vial down with 70% ethanol and bring the vial back into the biosafety cabinet.
6. Remove and discard the supernatant and resuspend the pellet with 5 mL of fresh DMEM F-12 (**without DMSO**). Then transfer the cells back into the flask and place the flask back into the incubator.

Cryopreservation procedure:

1. Inspect the flask(s) that are to be used for cryopreservation and verify 80% confluency.
 2. Remove freezing media from the refrigerator and allow it to warm up to at least 17°C
 3. Scrape and remove the cells from the flask following the subculture protocol but remove 15-30µL of cell suspension before spinning the cells down.
 4. While the cells are in the centrifuge, perform a quick density and viability count using the standard hemocytometer protocol. Calculate the total number of cells in the vial.
 5. Resuspend the cells in freezing media to yield a density of approximately 2×10^6 cells/mL using the density determined previously. **Note:** Try to round the resuspension volume to the nearest whole mL volume. (Start a timer as soon as the cells are resuspended in the freezing media. This timer must not exceed 10 minutes before the cells are placed into the -80°C freezer)
 6. Transfer 1.0 mL of the resuspended cells into the Nunc vials, cap and label the vials if not previously labeled and set inside the Nalgene freezing container.
 7. Once the timer started in step 3 has reached at least 5 minutes, place the freezing container with the cells in the -80 °C freezer and allow them to cool for > 4 hours
- Then immediately transfer them to the cryo canes and place them in the LN dewar for storage in

LN vapor.

Protocol for Resuscitation of Frozen Cell Line
(adapted by Jay Sibbitts from information from ATCC.org)

Materials and equipment:

- Long forceps
- Face shield and cryo-gloves
- Complete media for cells used (enough to resuspend cells to the desired density + 9 mL for removal of cryoprotectant)

Note: all media used must be preconditioned in the incubator for at least 15 minutes to avoid excessive alkalinity.

- 2x15 mL conical vial
- Water bath (preheated to 37 °C)
- Timer

Procedure:

*indicates steps that require the use of the following additional safety equipment: Face shield and cryo gloves

1. Place a flask containing the media to be used in the incubator at 5% CO₂ and 37 °C for at least 15 minutes to avoid excess alkalinity of the medium during this procedure.
2. Ensure that the water bath has been turned on and has reached 37 °C
3. Follow the standard setup protocol for tissue culture
4. Wipe a 15 mL conical vial with 70% ethanol and bring it into the hood and label it as “wash”
5. Take the preconditioned media from the incubator and bring it into the hood. Transfer 9 mL of media into the “wash” vial
6. *Wearing the proper safety equipment, open the biocane dewar and retrieve the cane with the desired vial of cells and remove the vial while wearing the cryo-glove. Replace the cane in the dewar and be sure to replace the Styrofoam isolation plug before closing the lid of the dewar.

7. *Using the forceps (you may take off the cryo-gloves once you have secured the vial in the forceps), lower the vial into the preheated water bath and start the timer. The time should not exceed 2.5 min. **Note:** Hold the vial such that the cap remains above the liquid level to minimize chances of contamination.
8. As soon as the vial has thawed, wipe the vial with 70% ethanol and bring it into the hood.
9. Using a Kimwipe soaked with 70% ethanol, loosen the cap of the vial to release any pressure.
10. Carefully transfer the 1 mL from the vial dropwise into the “wash” media.
11. Centrifuge the vial at **800 rpm** for 5 minutes. While the cells are centrifuging, prepare the flask(s) into which you will be transferring the cells. (follow instructions specific to each cell line)
12. After centrifugation, wipe the vial with 70% ethanol and bring it into the hood.
13. Remove the supernatant being careful not to disturb the pellet and dispose of the “wash” media into an empty 15 mL conical vial.
14. Resuspend the cells in the volume of preconditioned media specified by the specific instructions for the cell line.

SIM-A9 Culture protocol
(adapted by Jay Sibbitts from subculture method on ATCC.org)

Materials and equipment:

-DMEM F-12 supplemented with 10% heat inactivated FBS and 5% heat inactivated horse serum, and 1x pen strep.

Note: A normal feed and a backup (i.e. 1/3 and 1/5 will require 32 mL of complete media)

-15 mL conical vial

-Glass cell scraper

-Squirt bottle with 70% ethanol

-2x T-75 culture flasks

CULTURE LAYING FLAT!

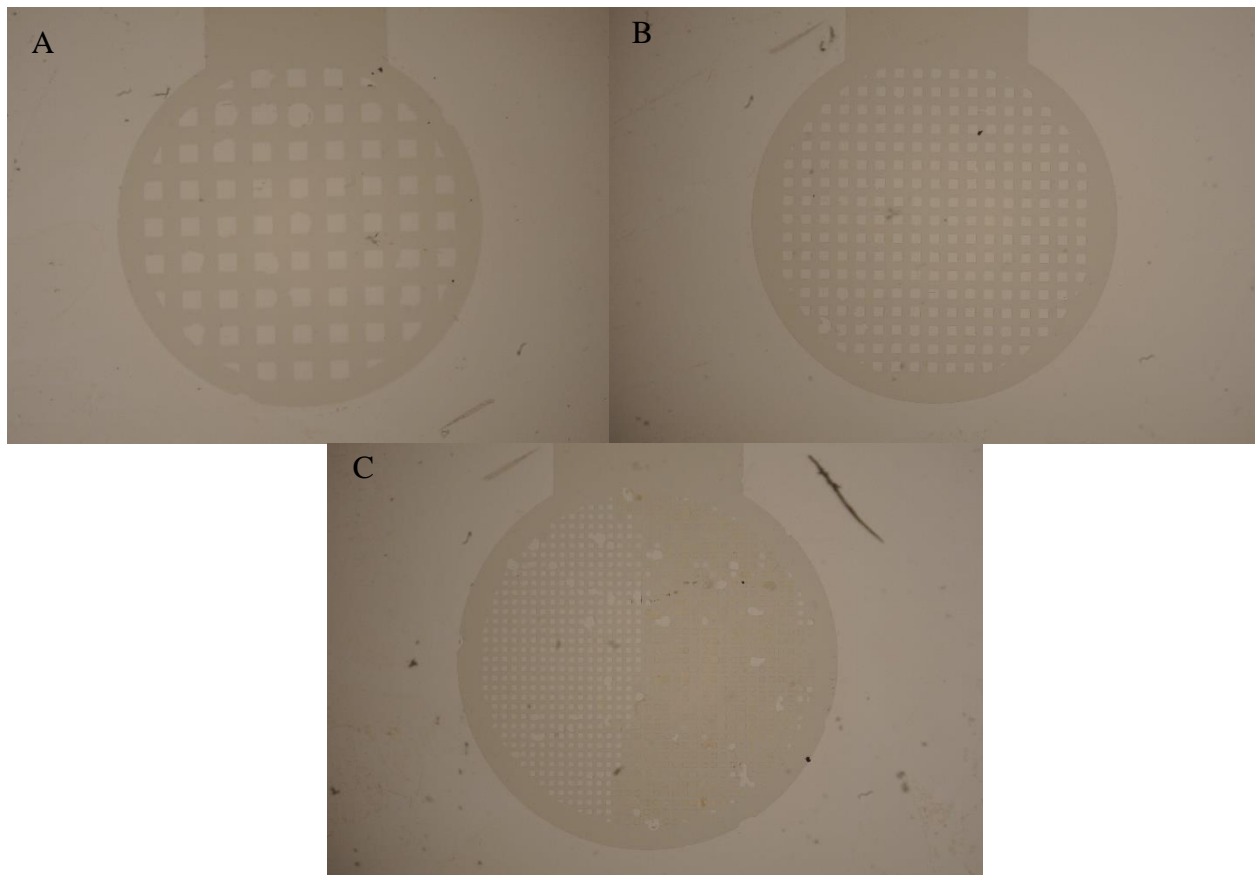
For one 75 cm² and one backup 75 cm² flask:

1. Follow standard setup protocol for tissue culture. Be sure to clean the glass scraper with 70% ethanol and carefully dry using a kimwipe.
2. Refer to the table below for the volume of media required for the desired split ratios in both the main split and the backup flask and label the empty flasks accordingly
3. Remove the previous feed from the incubator and visually inspect the cell layer to confirm approx. 80% confluency. (You may need to use the microscope. Be sure to wipe down the stage with 70% ethanol before)
4. If the cells are up to confluency, carefully scrape the cell layer, re-cap the flask and carefully slide the flask back and forth such that the scraped area is rinsed.
5. Transfer the entire volume of the flask into a sterile 15 mL conical vial, be sure to **note the total volume**, then centrifuge at 1000 rpm for 5 minutes. (1000 rpm results in 125xg using the Marathon 8k centrifuge, recalculate if you are using a different centrifuge, found in operating manual). While the cells are spinning down, dispense the previously determined volumes of fresh media into the new flasks.
6. Once the centrifuge has stopped, remove the conical vial, wipe with 70% ethanol and bring it back into the biosafety cabinet. Remove the supernatant and discard into the original flask.
7. Resuspend the pellet in fresh medium using 1/3 of the volume noted in step 4. This will make a **3x cell suspension** solution (e.g. if the original vol. was 12 mL then resuspend in 4 mL of fresh media)

8. Refer again to the table below and find the volume of 3x cell suspension required for the desired split ratio and deliver the appropriate volumes of 3x cell suspension into their respective flasks and place the new splits back into the incubator **LAYING FLAT**.
9. Follow standard cleanup and log sheet procedures to finish.

REMEMBER: Cell suspension is 3x concentrated				
Split Ratio	75 cm ² Flask V _{tot} = 15 mL		25 cm ² Flask V _{tot} = 5 mL	
(1/x)	Cell susp. (mL)	Media (mL)	Cell susp. (mL)	Media (mL)
1/3	1.7	13.3	0.56	4.44
1/4	1.25	13.75	0.42	4.58
1/5	1.00	14.00	0.33	4.67
1/6	0.8	14.2	0.28	4.72
1/7	0.7	14.3	0.24	4.76

Appendix B - Photographs of etched ITO grid electrodes



Photographs of initial attempts at etching of ITO grid electrodes. Line-widths and characteristic dimension of the squares for A, B, and C are 200 μm , 100 μm , and 50 μm , respectively.

Note: the defects in the 50 μm grid electrode pattern are likely caused by complications relating to expiring photoresist.

Appendix C - Arduino code for pumping control

```
int valvePins[] = {2,3,4,5};

// The first element of an array is index 0.
// We've put the value "2" in index 0, "3" in index 1, etc.
// The final index in the above array is 7, which contains
// the value "9".

// We're using the values in this array to specify the pin numbers
// that the 4 H-bridge inputs are connected to. H-bridge input 0 is connected
// to
// pin 2, H-bridge input 1 is connected to pin 3, etc.

void setup()
{
  int index;

  for(index = 0; index < 4; index++)
  {
    pinMode(valvePins[index],OUTPUT);
    // valvePins[index] is replaced by the value in the array.
    // For example, valvePins[0] is 2
  }
}

void loop() {
  oneAfterAnotherNoLoop();
} // put your main code here, to run repeatedly:
void oneAfterAnotherNoLoop()
{
  int delayTime = 10; // time (milliseconds) to pause between LEDs
                      // make this smaller for faster switching

  // turn all the LEDs on:

  digitalWrite(valvePins[0], HIGH); //Turns on valve #0 (pin 2)
  digitalWrite(valvePins[1], LOW);  //Turns on valve #1 (pin 3)
  digitalWrite(valvePins[2], HIGH); //Turns on valve #2 (pin 4)
  digitalWrite(valvePins[3], HIGH);
  delay(delayTime); //wait delayTime milliseconds

  digitalWrite(valvePins[0], HIGH); //Turns on valve #0 (pin 2)
  digitalWrite(valvePins[1], LOW);  //Turns on valve #1 (pin 3)
  digitalWrite(valvePins[2], LOW);   //Turns on valve #2 (pin 4)
  digitalWrite(valvePins[3], HIGH); //Turns on valve #3 (pin 5)
  //wait delayTime milliseconds
  delay(delayTime);
  digitalWrite(valvePins[0], HIGH); //Turns on valve #0 (pin 2)
  digitalWrite(valvePins[1], HIGH); //Turns on valve #1 (pin 3)
  digitalWrite(valvePins[2], LOW);  //Turns on valve #2 (pin 4)
```

```

    digitalWrite(valvePins[3], HIGH); //Turns on valve #3 (pin 5)
    delay(delayTime); //wait delayTime milliseconds

    digitalWrite(valvePins[0], LOW); //Turns on valve #0 (pin 2)
    digitalWrite(valvePins[1], HIGH); //Turns on valve #1 (pin 3)
    digitalWrite(valvePins[2], LOW); //Turns on valve #2 (pin 4)
    digitalWrite(valvePins[3], LOW); //Turns on valve #3 (pin 5)
    //wait delayTime milliseconds
    delay(delayTime);
    digitalWrite(valvePins[0], LOW); //Turns on valve #0 (pin 2)
    digitalWrite(valvePins[1], HIGH); //Turns on valve #1 (pin 3)
    digitalWrite(valvePins[2], HIGH); //Turns on valve #2 (pin 4)
    digitalWrite(valvePins[3], LOW); //Turns on valve #3 (pin 5)
    //wait delayTime milliseconds
    delay(delayTime);
    digitalWrite(valvePins[0], LOW); //Turns on valve #0 (pin 2)
    digitalWrite(valvePins[1], LOW); //Turns on valve #1 (pin 3)
    digitalWrite(valvePins[2], HIGH); //Turns on valve #2 (pin 4)
    digitalWrite(valvePins[3], LOW); //Turns on valve #3 (pin 5)
    //wait delayTime milliseconds
    delay(delayTime);
}

```